Faculty of Aeronautics and Astronautics, Department of Aerospace Engineering

AEE-412 Aerospace Design II

Cruise Missile Design

Instructor:
Prof.Dr.Ahmet Salih YİĞİT

Team - 1 & 2:

Control & Structure	**CFD & Propulsion**
Batuhan Şahin	Oğuzhan Çamlıca
Yasin Bera Şen	Muhammet Berati Kılıç
Mehmet Yusuf Demirbaş	Muhammed Emre Çetin
Süleyman Sert	Arzu İsmi
İsmail Bayraktar	Burak Akbulut
Merve Sümer	Fatma Zehra Pekince
Ceren Meral	Elif Hazan Efe

Academic Year 2024/2025

Contents

Nomenclature

Symbol / Term	Definition	Unit
α , AoA	Angle of Attack	deg (°)
β	Sideslip angle	deg (°)
C_L	Lift coefficient	–
C_f	Friction coefficient	–
FF	Form Factor	–
C_D	Drag coefficient	–
C_M	Pitching moment coefficient	–
C_A	Axial force coefficient	–
C_N	Normal force coefficient	–
C_Y	Side force coefficient	–
C_p	Pressure Coefficient	–
e	Oswald Efficiency Factor	–
C_l	Rolling moment coefficient	–
C_n	Yawing moment coefficient	–
CP	Center of Pressure	–
CG	Center of Gravity	–
S_{ref}	Reference area	m^2
S_{inlet}	Engine Air Intake Inlet Area	m^2
L_{ref}	Reference length	m
Lat_{ref}	Lateral reference length	m
X_{CG}	Center of gravity location	m
M	Mach number	–
Re	Reynolds number	–
u, v, w	Velocity components in body axes	m/s
p, q, r	Angular velocity components	rad/s
P, Q, R	Angular velocity components (Euler transformed)	rad/s
ϕ, θ, ψ	Roll, pitch, yaw angles	rad or deg
I_x, I_y, I_z	Moments of inertia about body axes	$\text{kg}\cdot\text{m}^2$
F_A, F_G, F_T	Aerodynamic, gravitational, thrust forces	N
L, M, N	Rolling, pitching, yawing moments	N·m
μ	Dynamic viscosity	Pa·s
ν	Kinematic viscosity	m^2/s
ρ	Air density	kg/m^3
q	Dynamic Pressure	N/m^3 or Pa
y^+	Dimensionless wall distance	–
SST	Shear Stress Transport	–

CFD	Computational Fluid Dynamics	–
Missile DATCOM	Coefficient Estimation Program	–
CDR	Critical Design Review	–
PDR	Preliminary Design Review	–
RANS	Reynolds averaged Navier–Stokes	–
DoF	Degree of Freedom	–
NACA	Neighborhood Assistance Corporation of America	–
SFC	Thrust Specific Fuel Conception	g/(kN·s)
YS	Yield Strength	MPa
UTS	Ultimate Tensile Strength	Mpa

1 Executive Summary

1.1 Brief Overview of the Project

This report covers the detailed design process of a cruise missile capable of being launched from a fighter aircraft and neutralize sea and land targets with high precision. The primary objective of the design is to develop an effective, low cost missile that can be integrated into existing systems and reach a range of 100 kilometers.

The project builds upon the Preliminary Design Review (PDR) phase. During that phase, mission requirements were defined, various flight profiles were evaluated, and the "climb and dive" profile was selected. Initial sizing was carried out, and preliminary thrust and fuel estimations were made. These fundamental studies formed the basis for the inclusive engineering analyses presented in this report.

1.2 Purpose and Scope of the Critical Design Review (CDR)

The purpose of this CDR report is to assess the technical readiness of the developed cruise missile by verifying the engineering analyses of all subsystems following the conceptual design phase. At this stage, it is determined whether the design has improved enough to meet the mission requirements.

The main systems and analysis scopes presented in the report are as follows:

- **Aerodynamic System:** The missile's aerodynamic behavior and shock effects were evaluated using Computational Fluid Dynamics (CFD) analyses. Design revisions were proposed, and Lift and drag coefficients were calculated .
- **Propulsion System:** The JetCat P550 Pro turbojet engine was selected. Its integration, fuel consumption, and thrust requirements were validated through detailed calculations.
- **Structure and Materials:** Structural elements were analyzed under various load conditions. Optimal materials were selected as aluminum alloys based on performance.
- **GNC (Guidance, Navigation, and Control):** A 6-Degree of Freedom (DoF) mathematical model was developed. The basis of control algorithms was established.
- **Payload:** The XF-10 thermobaric and fragmentation warhead with high explosive power was selected for its effectiveness against sea targets.
- **System Integration:** The compatibility among subsystems, weight distribution, and center of gravity positioning were analyzed.

- **Reliability and Safety:** FMEA analyses were conducted to identify potential failure modes, and risk mitigation strategies were developed.

In this context, CDR serves as an intermediate technical verification stage before transferring the missile system to prototyping, production and testing processes.

1.3 Key Findings and Recommendations

Key Findings:

- CFD simulations at Mach 0.7 revealed shockwave formation over the wing, increasing drag. A more compact wing is under consideration to improve aerodynamic and structural performance.
- The Shear Stress Transport (SST) k-ω turbulence model provided accurate Wall bounded results, but due to high computational cost, the k-ε model was preferred for control oriented analyses.
- Folding wing regions showed drag penalties caused by abrupt transitions. Smoother geometries are recommended.
- The JetCat P550 Pro engine was selected after thrust requirements were calculated. GasTurb simulations confirmed its performance under varying conditions.
- Structural analysis using CFD derived loads showed stresses (max $\sim$1.4 MPa) well below the material's yield strength. Modal analysis of the fuselage revealed no resonance risks.
- A 6 DoF missile model was developed and trimmed in cruise using aerodynamic and propulsion lookup tables. This model supports the ongoing control system design.

Recommendations:

- Finalize Center of Gravity (c.g) and CP locations to assess static stability.
- Integrate the air intake and nozzle exhaust into the full CFD model to assess pressure and drag impact.
- Extend system linearization for control design beyond cruise conditions.
- Perform modal analysis on wing components to identify potential aeroelastic risks.
- Re-evaluate fuel and propulsion performance under worst case thermal and maneuvering loads.

2 Introduction

This project focuses on the conceptual and detailed design of a cruise missile capable of performing precision air to surface strikes. The main objective is to develop a compact, efficient, and mission ready missile that can be launched from a fighter aircraft, follow a sea skimming or climb and dive flight path, and successfully reach and destroy surface or naval targets. Key design goals include high accuracy, long range, survivability against modern defense systems, and integration of subsystems such as propulsion, aerodynamics, guidance, control, and payload.

During the previous semester, our team completed the Preliminary Design Review (PDR) phase. In this phase, we identified the mission requirements, explored different flight profiles, and selected the "climb and dive" profile as the most effective for our target type. We also performed initial sizing of the missile, selected an airfoil, made first estimations for engine thrust and fuel needs, and proposed a general configuration. Each subsystem team presented early design ideas and feasibility analyses, which formed the foundation of our current work.

Now, in the Critical Design Review (CDR) phase, the aim is to finalize the design with more detailed calculations, simulations, and validation steps. CDR is a very important milestone in the aerospace design process because it shows whether the system is ready to move forward towards manufacturing and testing. At this stage, the interactions between subsystems are carefully examined, and performance predictions are improved using more advanced tools. A successful CDR means that the design is mature, realistic, and complete enough to proceed to the next phases of development.

This report explains the work completed during the CDR phase, including detailed analysis of aerodynamics, propulsion, structures, payload, guidance and control, as well as safety and reliability studies

3 System Design Overview

3.1 Mission Requirements

3.1.1 Target Performance Criteria

The cruise missile is designed for air to surface strike missions against naval targets. It is intended to be launched from a fighter aircraft. The primary performance criteria are as follows:

- **Range:** The missile must achieve a minimum range of 100 km, enabling standoff capability for enhanced platform survivability.
- **Accuracy:** High terminal accuracy is required to ensure a direct hit on stationary naval targets. A Circular Error Probable (CEP) of less than 10 meters is targeted.
- **Payload Capacity:** The missile shall carry a high explosive warhead designed to effectively neutralize medium sized naval vessels.
- **Flight Profile:** The missile should cruise at 10,000 ft.

3.1.2 Operational Constraints and Environmental Considerations

- **Launch Platform:** The missile is to be deployed from combat aircraft, necessitating compatibility with aircraft hardpoints and onboard systems.
- **Sea Skimming Capability:** The missile must maintain a low altitude trajecto over the sea using an altimeter and terrain following navigation, minimizing its radar cross section and exposure time.
- **Navigation System:** A robust, hybrid navigation system integrating GPS and Inertial Navigation Systems (INS) is required. Additionally, terminal seeker guidance (e.g., active radar or imaging infrared) may be employed to enhance precision in the final approach.
- **Environmental Conditions:** The missile must remain operational across a wide range of maritime environments, including windy conditions, sea spray, and low visibility.
- **Survivability:** The missile design should incorporate ow radar cross section (RCS) materials and geometry, and include terminal phase evasive maneuvering capabilities to bypass modern naval defense systems.

3.1.3 Mission Profile Options

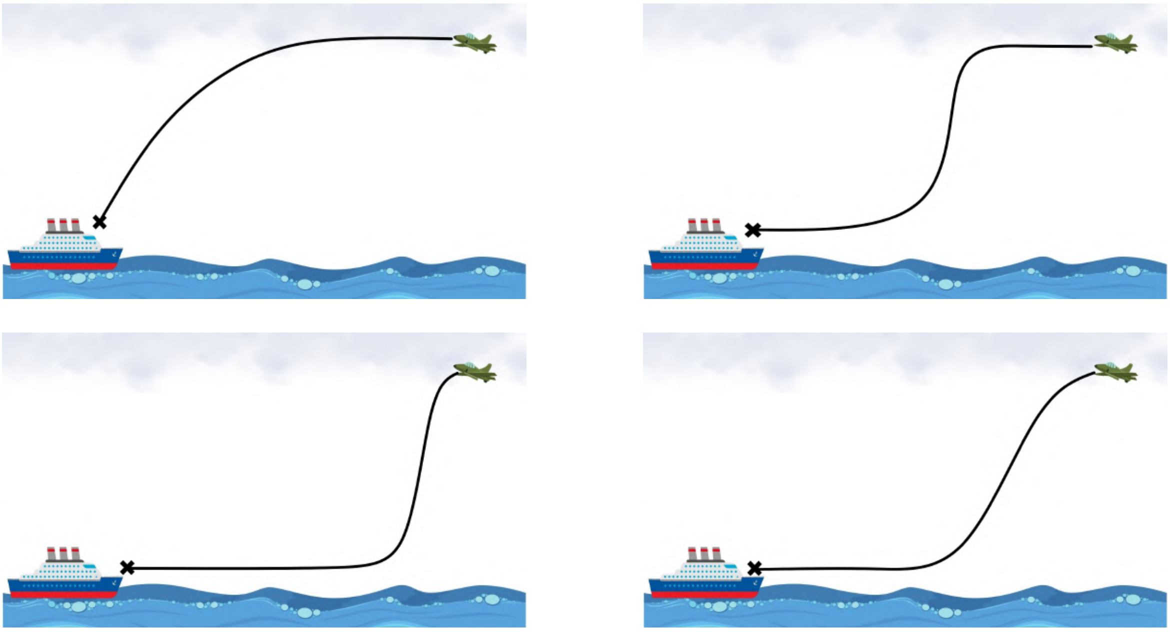

Figure 1: Mission Profiles

Table 2: Missile Mission Profiles

Profile	Characteristics, Advantages	Applications
Parabolic (Ballistic High Altitude)	- High altitude parabolic trajectory. - Maximizes range, bypasses radar. - Harder to intercept.	- Long range land or sea targets.
Low Altitude Cruise	- Sea skimming flight path. - Minimizes radar visibility. - Avoids terrain and waves.	- Anti ship missions. - Coastal or low altitude land targets.
Climb and Dive	- Sharp dive after ascent. - Penetrates armor and defense. - Gains speed at terminal phase.	- Armored ships. - Fortified land bunkers.
Mixed Maneuvering	- Low altitude cruise + evasive maneuvers. - Confuses defense systems. - High agility and stealth.	- Aircraft carriers. - Protected facilities.

3.1.4 Chosen Mission Profile: Climb and Dive

The Climb and Dive profile was selected for our cruise missile operations due to its advantages in overcoming defensive systems. This profile allows the missile to:

Ascend initially to avoid low level defenses.

Dive steeply towards the target, increasing speed and reducing interception time.

Bypass armor and defense systems, ideal for heavily armored ships or fortified bunkers.

The Climb and Dive profile is highly effective for penetrating well protected targets, making it the best choice for our mission.

3.2 Concept of Operations (CONOPS)

3.2.1 Purpose of Operation

The purpose of this project is to design a cruise missile capable of engaging naval and ground targets, such as ships and tanks. The missile will be launched from an aerial platform (UAV or aircraft) at an altitude of 20,000 ft and will travel over a distance of 100 km or more to destroy the designated target. The missile is expected to reach a cruise speed of Mach 0.7 and maintain stable flight performance against possible disturbances during the mission.

3.2.2 Operational Environment

For naval targets, the missile will operate over sea environments. Therefore, the missile design will ensure resistance against humidity and other challenging conditions over the sea surface. For ground targets, the missile must have sufficient maneuverability and robustness to operate effectively in various terrain conditions.

3.2.3 Mission Phases

The flight profile of the cruise missile is designed to fulfill the mission requirements and ensure successful target engagement. The trajectory consists of five main phases:

- **Launch Phase:** The missile will be released from an aerial platform at an altitude of 6,000 m (20,000 ft). After the release, the missile will perform a turning maneuver and descend to an altitude of 3,000 m (10,000 ft).

- **Cruising Phase:** Upon reaching 3,000 m (10,000 ft), the missile will maintain a steady cruise speed between Mach 0.6 and Mach 0.7. During this phase, GPS and INS systems will be used to ensure accurate navigation.

- **Descent Phase:** The missile will descend to an altitude of 100 m to save fuel and avoid detection from high altitude radar systems.

- **Low Altitude Cruise Phase:** After stabilizing at 100 m altitude, the missile will continue to approach the target at approximately Mach 0.7, utilizing GPS and INS navigation data.
- **Terminal Phase:** In the final phase, the IIR (Imaging Infrared) seeker will be activated, allowing the missile to precisely track and engage the target.

3.2.4 Mission Success Criteria

The mission will be considered successful if the missile can hit the target within a 10 meter radius and follow the desired trajectory without deviation.

3.2.5 Operational Constraints

- Operational Range: $\geq$ 100 km
- Accuracy (CEP): $\leq$ 10 m
- Flight Altitude: Minimum 100 m, Maximum 6,000 m
- Cruise Speed: Mach 0.7
- Missile Launch Weight: $<$ 100 kg
- Missile Total Cost: $<$ 100,000 USD
- Missile Total Length: $<$ 2 m
- Missile Body Diameter: $<$ 0.2 m

3.3 System Architecture

The overall system architecture of the designed cruise missile consists of several integrated subsystems working in coordination to ensure mission success. Each subsystem has a specific role and function in the operation of the missile from launch to target engagement. The main subsystems are as follows:

- **Airframe and Structure:** Provides the aerodynamic shape and structural integrity of the missile. Designed to withstand aerodynamic loads, environmental conditions, and dynamic effects throughout the flight.
- **Aerodynamic System:** Optimized for low altitude cruise and high maneuverability. The design includes wings and control surfaces that generate lift and provide stability and control.
- **Propulsion System:** The propulsion system consists of a turbojet engine (JetCat P550 Pro), providing the required thrust to maintain a cruise speed of Mach 0.7. Fuel tanks and the air intake system are integrated within the missile body.
- **Guidance, Navigation, and Control (GNC) System:** Ensures accurate trajectory tracking and stability during the flight. Combines GPS and INS systems for mid course navigation, with an IIR seeker activated in the terminal phase for precise target engagement.
- **Payload System:** The missile is equipped with a high explosive warhead designed for effective damage against both naval and ground targets.
- **Power and Electronics System:** Provides electrical power to all onboard systems, including sensors, actuators, control units, and communication devices.
- **Communication System:** Ensures necessary data transfer and communication between subsystems, and optionally provides uplink or telemetry data for mission monitoring.

4 Detailed Design Analysis

4.1 Aerodynamics

4.1.1 Objective of the Aerodynamics Team

The main objective of the Aerodynamics Team is to evaluate the missile geometry from an aerodynamic perspective in order to accurately predict aerodynamic forces and moments under real mission conditions. The generated aerodynamic data is then shared with other teams to support structural analysis, control system design, and propulsion system design.

4.1.2 Scope of the Aerodynamics Team

The tasks covered within the scope of the project are:

1. **Geometry Assessment:** Analyzing the external geometry of the missile to inspect its aerodynamic efficiency under the mission profile.
2. **Aerodynamic Modeling:** Predicting aerodynamic forces and moments over a range of flight conditions using CFD simulations, and semi empirical models (turbulence models).
3. **Stability and Control Derivatives:** Calculating static and dynamic stability derivatives to support control system design.
4. **CFD Validation:** Conducting Computational Fluid Dynamics (CFD) studies and validating the results using experimental data obtained from studied cases.
5. **Drag Reduction:** Applying aerodynamic modifications to minimize drag.
6. **Trajectory Based Analysis:** Providing aerodynamic data along the missile trajectory to be used in simulations with flight mechanics models.
7. **Interdisciplinary Coordination:** Collaborating with other teams to ensure that aerodynamic characteristics are consistent with structural, and propulsion constraints.

4.1.3 Aerodynamic Evaluation of Conceptual Design

The conceptual wing design was replaced with a more compact configuration due to its incompatibility with the geometric requirements of the foldable mechanism and its excessive length. As a result of the dimensional modifications, shortening the wing length facilitated system integration and made the folding mechanism geometrically feasible. However, the reduction in wing span limits lift at high altitudes due to the decreased lifting surface area, thereby restricting the operational flight ceiling to a certain level. Additionally, the NASA SC(2)-0010 airfoil was selected for the new configuration. This airfoil generates a near-sonic steady pressure distribution over the upper surface, which causes the shock wave to form further aft and with reduced intensity; thus, it provides low drag and high aerodynamic efficiency even at transonic speeds [1].

4.1.4 Altitude Strategy and Flight Profile

Before proceeding to 3D analysis as the Aerodynamics Team, the majority of our analyses up to this point have been conducted at an altitude of 10,000 ft. Although the general launch altitude is set as 20,000 ft, a gliding phase from 20,000 ft down to 10,000 ft is planned to gain energy both for propulsion efficiency and lift generation. After reaching 10,000 ft, the cruise phase is intended to begin, and the aerodynamic design has been developed accordingly.

4.1.5 Turbulence Model Selection

For the 3D missile analysis, the SST k-omega turbulence model was used for initial analysis. To briefly explain this model, it provides more accurate results compared to other RANS models [2,3] when modeling both low and high Reynolds number regions. In other words, it offers better modeling performance near the wall and in regions farther away from the wall. This helps us better identify and address the design flaws of the missile. However, compared to other RANS models, it requires higher computational cost due to its requirement for finer mesh near walls to achieve higher accuracy, the stiff nature of its equations, and its sensitivity to boundary conditions. These factors increase the numerical solution time and resource consumption [4]. Therefore, analyses for control derivatives where force and moment coefficients will be required,realizable the k-epsilon model will be used due to its lower computational cost [4].

4.1.6 CFD Analysis of Missile

In this study, steady state computational fluid dynamics (CFD) analyses were conducted using ANSYS Fluent 2020 R2 [5] in order to determine the aerodynamic characteristics of a cruise missile. The simulations were performed using the density-based solver to model compressible flow conditions, and the realizable k–ε with scalable wall function turbulence model was employed. The three dimensional geometry of the missile and CFD domain used in the analysis is provided in the Appendix as technical drawings 72. An unstructured mesh consisting of approximately 2.3 million cells was generated. The near-wall mesh resolution was adjusted to achieve a wall distance parameter of $y^+ \approx 100$. The computational domain was extended to approximately 30 times the missile body length, and pressure far-field boundary conditions were applied. Freestream conditions were defined based on an altitude of 10,000ft and a flight Mach number of 0.7. Since mass flow inlet and outlet boundary conditions cannot be defined for Missile DATCOM [6], some differences occur in the Missile DATCOM validation—such as neglecting inlet geometry and defining exhaust as a no slip wall. Accordingly, the boundary conditions for both Missile DATCOM and the main simulations are given in Table 3. During the solution process, the discretization scheme was initially set to first-order to enhance numerical stability in the early iterations. Once a stable residual trend was observed, the scheme was transitioned to a 50 % blended discretization to gradually introduce second-order accuracy while reducing numerical oscillations [7]. Finally, a full second-order scheme was adopted to maximize the accuracy of the flow predictions. This staged approach balances solution stability and accuracy throughout the simulation [7]. The stabilization of the lift coefficient (C_L) was used as the primary convergence criterion.

Table 3: Boundary Conditions for Cases

Case\Zone	**Body and Wings**	**Air Intake**	**Exhaust**	**Far Field**
Main Case	No-slip wall	Massflow inlet	Massflow outlet	Pressure Far Field
Missile DATCOM	No-slip wall	—	No-slip wall	Pressure Far Field

4.1.7 Turbulance Model Validation

To validate the selected turbulence model,Realizable $k - \epsilon$, numerical simulations were performed on the Onera M6 [8] wing and AGARD Model B [9], a benchmark cases in external wing and missile aerodynamics.

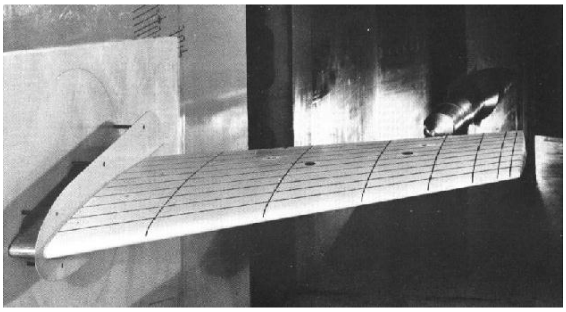

Figure 2: Onera M6 Wing [8]

Figure 3: Agard Model B [9]

ONERA M6

The test conditions were based on Test 2308 from Schmitt and Charpindey. [8] An overview of the applied flow conditions can be found in Table 4.

Table 4: Flow conditions for Test 2308

Mach	Reynolds Number	Angle of Attack (deg)	Angle of Sideslip (deg)
0.8395	11.72×10^6	3.06	0.0

The Cp distribution of Onera M6 wing shows good agreement with the experimental data, as seen in the Figure 4.

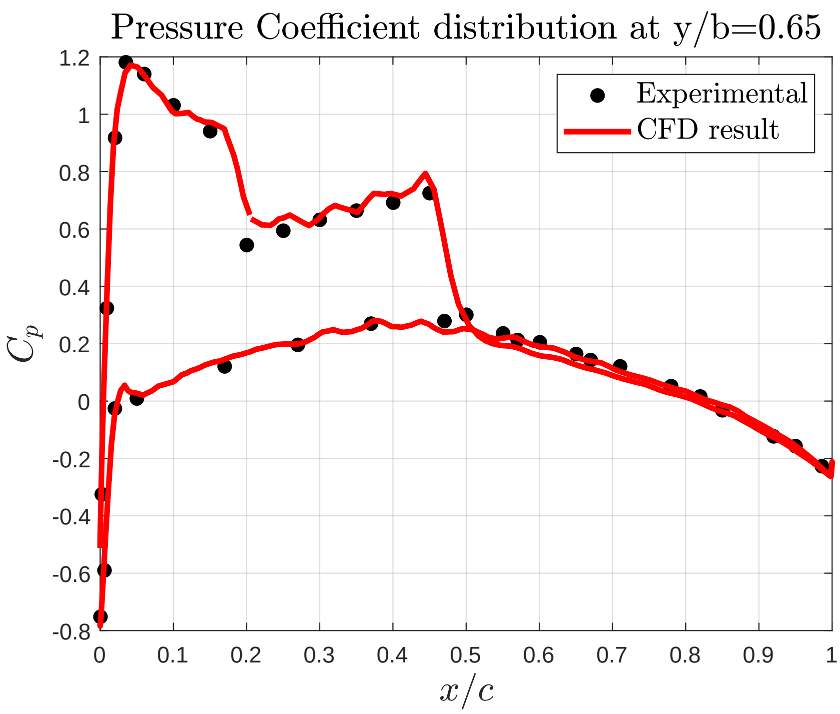

Figure 4: Comparison of experimental $-C_p$ profiles at y/b=0.65 [8].

This validation result indicate that the selected turbulence model yields reliable predictions for wing geometries under flow conditions similar in this study.

AGARD-B Model

The test conditions were based on experimental data presented by Tuling et al [9]. An overview of the applied flow conditions can be found in Table 5.

Table 5: Flow Conditions for AGARD-B Model

Mach	Reynolds Number	Angle of Attack (°)
0.8	1.125×10^6	$0 - 6$

The lift coefficient C_L values obtained from our CFD simulations show good agreement with the reference data for the AGARD-B model as seen in Figure 5.

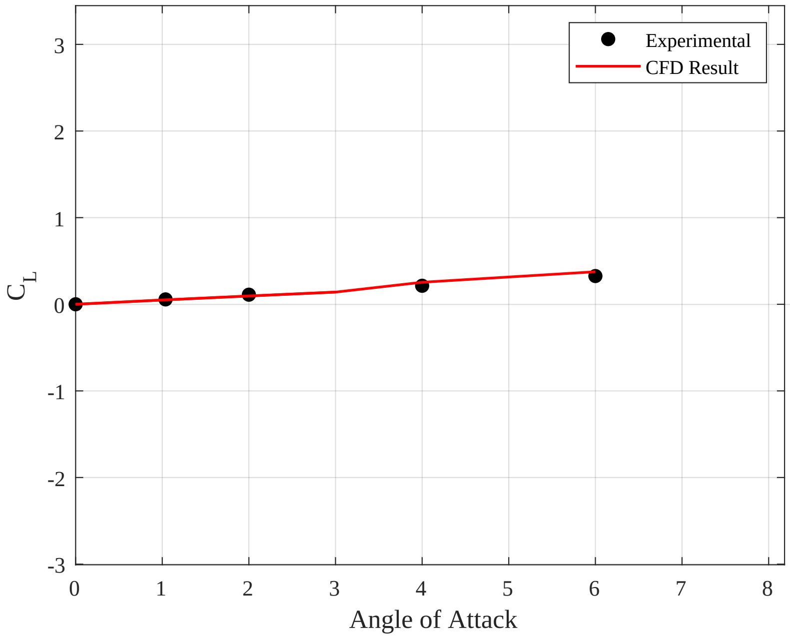

Figure 5: AGARD-B Model C_L Comparison

This validation result indicate that the selected turbulence model yields reliable predictions for missile geometries under flow conditions similar in this study.

4.1.8 Mesh Independence Study

To ensure mesh independence, a cross-sectional slice at y=0.3 m was taken, and the number of elements was compared for three different mesh densities: Coarse, Medium, and Fine. The number of elements for meshes with different densities is provided in Table 6.

Table 6: Number of elements for different mesh densities.

Mesh Type	Number of Elements
Coarse	1.66 M
Medium	2.28 M
Fine	3.26 M

The C_p distributions along the cross-section at y=3 are shown in Figure 6.

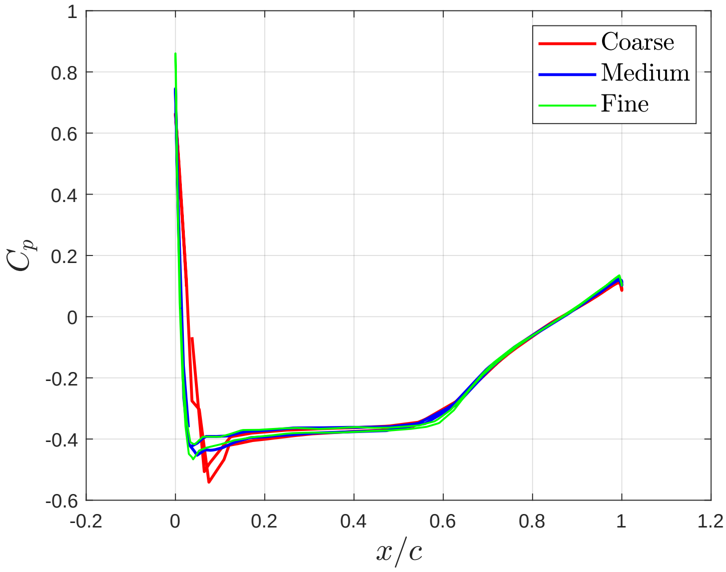

Figure 6: Pressure Coefficient Distribution for Different Mesh Densities

The good agreement between curves shows that further mesh refinement has little impact, confirming mesh independence. Therefore, the medium mesh was selected for subsequent analyses.

4.1.9 CFD Results

CFD analyses were conducted on the main missile geometry at various angles of attack as well as on the geometry designated for Missile DATCOM validation. In these simulations, the convergence behaviors of C_L and C_D at 0° angle of attack, as presented in the figures, exhibited similar trends. Figure 7a presents the lift coefficient convergence plot, demonstrating compliance with the $\Delta C_L < 5 \times 10^{-3}$ tolerance, while Figure 7b shows the drag coefficient convergence plot, indicating satisfaction of the $\Delta C_D < 1 \times 10^{-4}$ criterion.

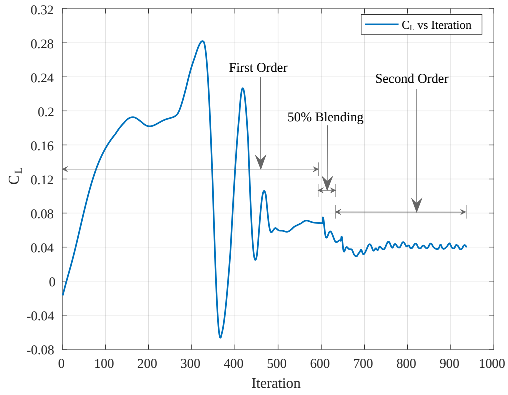

(a) C_L Convergence

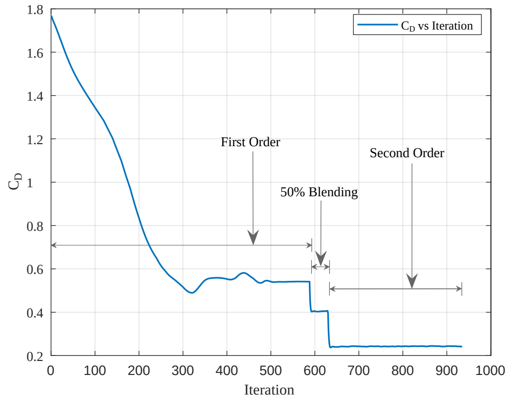

(b) C_D Convergence

Figure 7: C_L and C_D convergence graphs

The y^+ distributions on the wing surface as shown in Figure 8a and the fin surface as shown in Figure 8b confirm that y^+ values remain within the range of 30–130 on both surfaces, thereby fully meeting the near-wall requirements of the realizable $k\text{–}\varepsilon$ turbulence model. Moreover, simulations performed for Missile DATCOM validation exhibited similar convergence behavior, underscoring that the CFD methodology employing the selected turbulence model and solver configurations delivers sufficiently stable and accurate results. The simulation outputs were provided to other units.

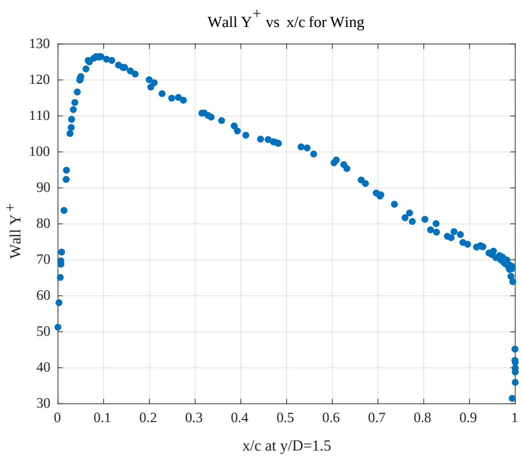

(a) Wing y^+ distribution

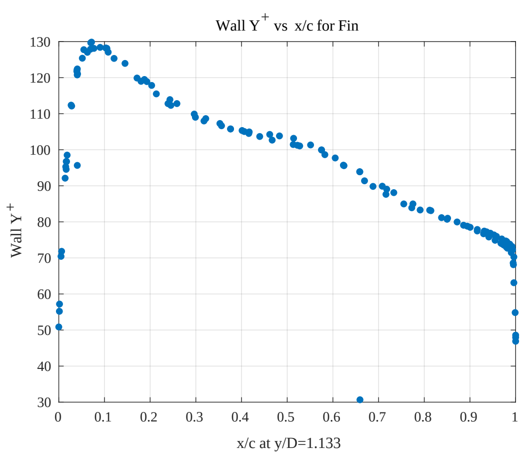

(b) Fin y^+ distribution

Figure 8: Wing and Fin y^+ distributions

4.1.10 Aerodynamical Design Observations and Improvements

Sharp Transitions

From the velocity contours of initial design as shown in Figure 9, we observed that the rear part of the wing folding mechanism caused a significant drop in velocity, leading to a substantial increase in drag force. As a result of this observation, it was concluded that the transition at the rear part of the folding mechanism should be made smoother. The revised transition could be seen in Appendix via technical drawing 71.

Figure 9: Velocity Contour of Missile at 0° Angle of Attack Before Revision at y/D=0

Air Intake and Exhaust Boundary Conditions

To improve the accuracy of total drag prediction, mass flow rates were defined at both the air intake and exhaust in the aerodynamic simulations. This approach ensures a more realistic representation of the propulsion effect on the flow field.

Nose Shape

No modification will be made to the nose design due to the dimensional constraints forced by the seeker component planned to be placed there.

Change of Backward of Air Intake

In the baseline design, the rear section of the air intake was mounted directly to the cruise missile body. At this point, a geometrically sharp and sudden transition occurs, resulting in an increase in aerodynamic drag. To overcome this problem, the rear section of the air intake has been redesigned to provide a smoother and more continuous transition, can be seen from Figure 10. As a result of this design change, a 12.9 % reduction in drag force was achieved, as can be seen in Table 7. This improvement shows that the design change was effective. The analysis are conducted at 0 ° angle of attack.

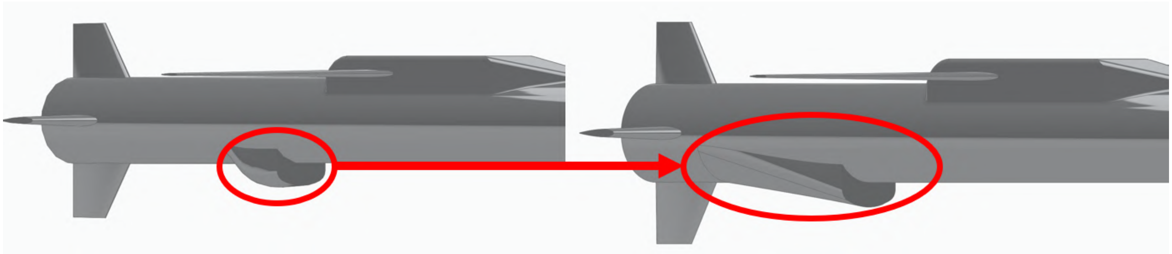

Figure 10: Aerodynamic Design Revision of Backside of Air Intake

Parameter	Baseline Design	Revised Design	Reduction (%)	AoA (°)
Drag Coefficient (C_D)	0.277	0.242	-12.9%	0 °

Table 7: Comparison of Drag Coefficient

Revision of Angle of Incidence

In this project, the Angle of Incidence value was reduced from its previous value of 3.4 degrees to 0 degrees. The reason for this change was the feedback from the control team that this angle of incidence would create instability in the control of the aircraft. The aerodynamic data at cruise speed and altitude after the application are as can bee seen at Table 8:

Parameter	Value
Cruise Angle of Attack (α_{cruise})	1.82°
Cruise Lift Coefficient (C_L)	1.15
Cruise Drag Coefficient (C_D)	0.38
Cruise Lift-to-Drag Ratio (C_L/C_D)	3.013

Table 8: Aerodynamic Data at Cruise Mach Number and Altitude

Aerodynamic Evaluation of Missile Fins

CFD simulations were done to check if the elevator missile fins which is given a 5° deflection could generate the aerodynamic forces necessary for the desired maneuverability. Raising the angle of attack from 0° to 7° led to a rise in the load factor as can be seen from Table 9, achieving 2.51G at 7°, surpassing the 2G limit before 10°, a level enough for maneuverability.

Angle of Attack (°)	Load Factor (G)
0	-0.85
5	1.91
7	2.51

Table 9: Angle of Attack vs Load Factor

4.1.11 Missile DATCOM Validation

To provide the control team with the necessary aerodynamic derivatives and coefficients, Missile DATCOM [6] was utilized due to its computational efficiency and the extensive time requirements of high-fidelity CFD solutions

The corresponding input and output files are included in Appendix 1 for reference.

Although Missile DATCOM [6] offers rapid estimations, its accuracy can be limited, especially for complex geometries or flow conditions. Therefore, to validate the reliability of the Missile DATCOM [6] results, selected outputs were compared against available CFD solutions.

As shown in Figure 11, and Table 10 the agreement between Missile DATCOM and CFD in terms of C_N, C_M, and C_A was found to be satisfactory for the intended design phase.

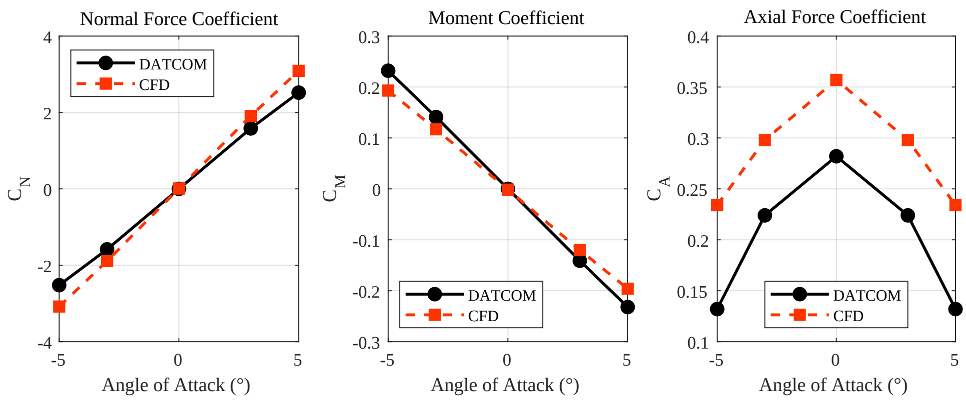

Figure 11: Comparison of Missile DATCOM and CFD Results for C_N,C_M,and C_A

Angle of Attack (°)	C_N		C_M		C_A	
	Missile Datcom	CFD	Missile Datcom	CFD	Missile Datcom	CFD
-5	-2.520	-3.080	0.232	0.193	0.132	0.234
-3	-1.583	-1.890	0.141	0.117	0.224	0.298
0	0.000	0.009	0.000	-0.002	0.282	0.357
3	1.583	1.910	-0.141	-0.120	0.224	0.298
5	2.520	3.090	-0.232	-0.196	0.132	0.234

Table 10: Comparison of Missile DATCOM and CFD Results for C_N, C_M, and C_A

4.2 Propulsion System

4.2.1 Thrust Requirement Analysis and Calculation

In this section, the required thrust was estimated based on the total drag of the aircraft. The total drag coefficient was calculated as the sum of the parasite drag and the induced drag:

$$C_D = C_{D_0} + KC_L^2$$

Here, C_{D_0} represents the parasite drag coefficient, and KC_L^2 represents the induced drag coefficient.

The parasite drag coefficient C_{D_0} was determined using the component build-up method, as described in Raymer's textbook [10]. This method estimates the subsonic parasite drag of each aircraft component using a flat-plate skin-friction drag coefficient C_f, a form factor FF that accounts for pressure drag due to viscous separation, and an interference factor Q to account for the mutual aerodynamic effects between components [10]. Assuming steady, level flight, it was considered that lift equals weight. Additionally, a simplified case was adopted where the weight was not directly included in the thrust calculation but was assumed to be balanced by lift. Subsonic parasite drag buildup is represented as:

$$(C_{D_0})_{\text{subsonic}} = \frac{\sum(C_f \cdot FF \cdot Q \cdot S_{\text{wet}})}{S_{\text{ref}}} + C_{D_{\text{misc}}} + C_{D_{\text{L\&P}}}$$

where $C_{D_{\text{misc}}}$ includes drag from base area, while $C_{D_{\text{L\&P}}}$ accounts for leakages and protuberances. The parasite drag is calculated separately for each component, such as the fuselage, wing, and tail.

- Reference wing area: $S_{\text{ref}} = 0.0314\,\text{m}^2$
- Flight velocity: $V = 781\,\text{ft/s} \approx 238.1\,\text{m/s}$
- Air density at sea level: $\rho = 0.0765\,\text{slug/ft}^3 \approx 1.226\,\text{kg/m}^3$
- Dynamic pressure: $q = 726\,\text{psf} \approx 34.76\,\text{kPa}$

Parasite Drag

The Reynolds number is computed using the equation:

$$Re = \frac{\rho \cdot V \cdot L}{\mu} \tag{1}$$

For turbulent boundary layers on flat plates, the empirical skin friction coefficient is given by:

$$C_f = \frac{0.455}{((\log_{10} Re)^{2.58}) \cdot (1 + 0.144 \cdot M^2)^{0.65}} \tag{2}$$

This is valid for fully turbulent flow over smooth surfaces.

The form factor accounts for additional drag due to the shape and flow separation effects. For a body of revolution (e.g., fuselage), it is approximated as:

$$FF = \left(1 + \frac{60}{(l/d)^3} + 0.0025\, l/d\right) \tag{3}$$

where l/d is the length-to-diameter ratio.

For wing and tail surfaces, a simplified estimation is:

$$FF = [1 + \frac{0.6}{0.3}\frac{t}{c} + 100\left(\frac{t}{c}\right)^4] \cdot [1.34 \cdot M^{0.18} \cdot cos(\Lambda_m)^{0.28}] \tag{4}$$

where t/c is the thickness-to-chord ratio.

Each component's parasitic drag is calculated as:

$$C_D = C_f \cdot FF \cdot \frac{S_{\text{wet}}}{S_{\text{ref}}} \tag{5}$$

Interference Drag Estimation

In the preliminary drag estimation, the parasite drag contributions from the wing and tail were multiplied by an interference factor of 1.25. This factor accounts for interference drag, which arises when two aircraft components are in proximity—such as the wing-fuselage or tail-fuselage junctions. These junctions cause boundary layer thickening, increased pressure drag, and flow separation effects that would not occur if the components were isolated. According to standard empirical guidelines, such as those in Chapter 12 of Raymer (2018), a Q factor of 1.25 is appropriate for components like wings or tails that are immersed in accelerated flow near the fuselage or each other. This adjustment ensures a more realistic estimate of the parasitic drag in multi-body configurations. [10]

- **Fuselage:**

$$\begin{aligned} \text{Re}_{\text{fuselage}} &= 1.175 \times 10^9 \\ C_{f,\text{fuselage}} &= 0.0015 \\ \text{Form Factor (FF)} &= 1.085 \\ C_{D,\text{fuselage}} &= 0.0698 \end{aligned}$$

- **Wing:**

$$\begin{aligned}
\text{Re}_{\text{wing}} &= 7.837 \times 10^7 \\
C_{f,\text{wing}} &= 0.0021 \\
\text{Form Factor (FF)} &= 0.872 \\
C_{D,\text{wing}} &= 0.0165
\end{aligned}$$

- **Tail (Fin):**

$$\begin{aligned}
\text{Re}_{\text{tail}} &= 8.277 \times 10^7 \\
C_{f,\text{tail}} &= 0.0021 \\
\text{Form Factor (FF)} &= 1.697 \\
C_{D,\text{tail}} &= 0.0224
\end{aligned}$$

Total Drag and Lift Coefficient

The zero-lift drag coefficient is computed as the sum of the individual components:

$$C_{D_0} = C_{D,\text{fuselage}} + C_{D,\text{wing}} + C_{D,\text{tail}} = 0.109$$

The lift coefficient is obtained from the required lift:

$$C_L = \frac{L}{q \cdot S_{\text{ref}}} = \frac{1032}{34761.2 \times 0.0314} = 0.945$$

Oswald Efficiency Factor (e) and Induced Drag Factor (K)

To account for the extra drag due to the nonelliptical lift distribution and flow separation, the Oswald efficiency factor **e** is used [10]. It effectively reduces the aspect ratio in the induced drag factor **K**, which is calculated by:

$$K = \frac{1}{\pi \cdot A \cdot e}$$

$$e = 1.78(1 - 0.045 \cdot A^{0.68}) - 0.64$$

$$e = 0.066$$

$$K = 0.106$$

$$C_D = C_{D_0} + KC_L^2 = 0.108670 + 0.105662 \cdot (0.945)^2 = 0.102$$

Thrust Requirement

The required thrust is calculated from the drag force:

$$D = C_D \cdot q \cdot S_{\text{ref}} = 0.102 \cdot 34761.2 \cdot 0.031 = 221.7\,\text{N}$$

Thus, the engine must provide a minimum of 221.7 N of thrust to maintain steady-level flight at Mach 0.7 at sea level.

There is a MATLAB [11] code in the Appendix 10 where drag is calculated.

4.2.2 Engine Selection

This section outlines the engineering process and technical evaluations conducted to determine the appropriate turbojet engine for the cruise missile. The selection was based on aerodynamic requirements, dimensional constraints, system integration considerations, and data availability. The turbojet engine is selected based on these criteria:

- **Thrust Requirement:** Based on the component drag analysis from Raymer's *Aircraft Design* [10], the body, wings, and fins were evaluated separately. To maintain the cruise flight at Mach 0.7 and at sea level, the required continuous thrust was calculated as 221 N.

- **Diameter and Length Constraint:** The missile design imposes a maximum fuselage outer radius of 200 mm. Therefore, the engine diameter must remain within this limit. This limit also includes structural supports, mounting hardware, and possible thermal protection. Selecting an engine that fits within these tight dimensional constraints is critical for ensuring successful integration.

- **Performance and Documentation:** Engines offering a balance of high and efficient performance were prioritized. In addition, the availability of technical data and performance parameters through open-access sources was considered essential to support analysis and system integration.

4.2.3 Turbojet Engine Selection Process

As a result of the research, three different turbojet engines from different manufacturers were considered. The relevant engines are listed in Table 11. The German-made JetCat P550 PRO [12] turbojet engine was selected due to its ability to easily provide the required thrust, its compliance with the diameter constraint without the need for modifications, the availability of key performance parameters such as mass flow and pressure ratio, and the presence of an open-access user manual.

Engine Model	**Thrust (N)**	**Length (mm)**	**Diameter (mm)**	**Remarks**
JetCat P550 PRO [12]	550	427	175	Detailed specs available, selected
Swiwin SW600 PRO [13]	600	372	177	Insufficient system-level data, not selected
AMT Nike [14]	784	396	178	Exceeds diameter constraint, not preferred

Table 11: Turbojet Engine Options

4.2.4 Selected Engine: JetCat P550 Pro

The technical documentation of the JetCat P550 PRO [12] turbojet engine is represented in Table 12. The technical drawing of the JetCat P550 PRO turbojet engine is shown in Figure 12.

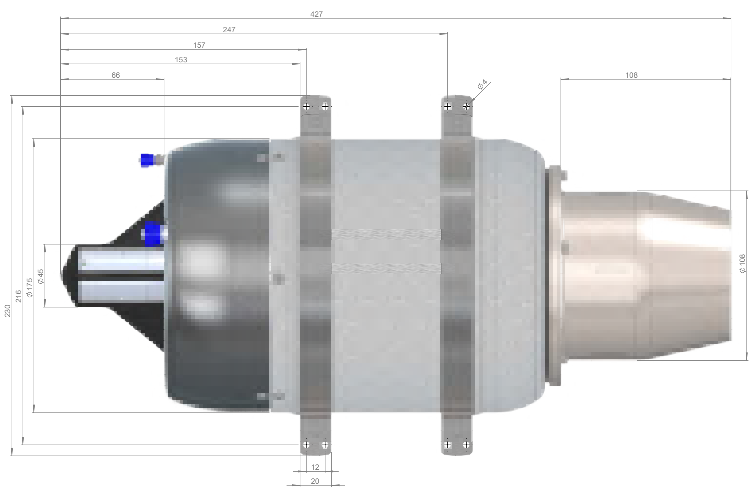

Figure 12: Technical Drawing of JetCat P550 PRO Turbojet Engine

Table 12: JetCat P550 PRO Technical Specifications

Specification	**Value**
Thrust Range	28–550 N
Specific Fuel Consumption (SFC)	0.144 kg/Nh
Fuel Flow Rate	300–1650 mL/min
Fuel Type	Jet-A1/Diesel + 3–5% JetCat oil
Weight	5400 g
Diameter	175 mm
Length	427 mm
RPM Range	26,000–83,000 rpm
Exhaust Gas Temperature	480–750 °C
Air Mass Flow	0.93 kg/s
Exhaust Gas Velocity	2129 km/h
Exhaust Gas Power Output (Max)	163 kW
Ignition System	Direct kerosene start
Integrated Components	ECU, fuel pump, solenoids, post-filter, ignition, EGT probe
Power Input	10–35 VDC
Connectors	1x data, 1x power

4.2.5 Engine System Integration

The JetCat P550 engine requires supporting components including a fuel tank, feeder/hoppertank, Pro-Interface (ECU), and other accessories. These components will be positioned and integrated in coordination with the structural team, considering factors such as center of gravity, wiring routes, and service accessibility.

Figure 13 shows a conceptual block diagram of the engine system integration.

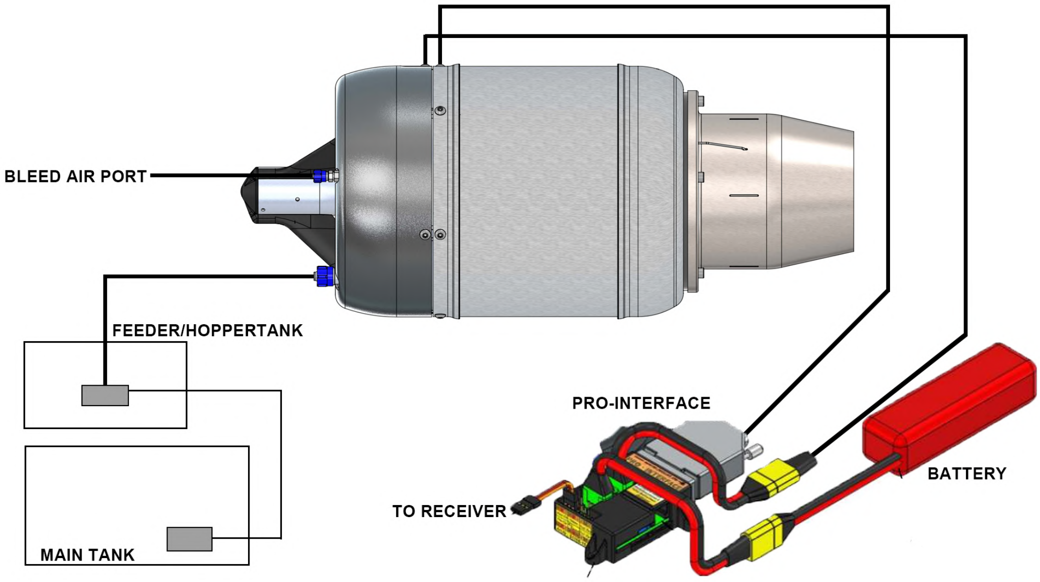

Figure 13: JetCat P550 system integration schematic

4.2.6 Engine Performance Analysis Using GasTurb

In this section, propulsion analysis is conducted using the GasTurb 11 [15] software. The selected engine was modeled within the application, and various performance analyses were carried out using relevant input parameters.

Due to the limited availability of manufacturer data, several critical parameters were obtained from the experimental study titled "Thermodynamic Analysis and Performance Evaluation of Microjet Engines in Gas Turbine Education" [16], in which the selected engine is also included.

The data extracted from the study are as follows:

- Burner Exit Temperature = 1214.6 K
- Compressor Exit Temperature = 453.6 K
- Compressor Efficiency = 0.80
- Turbine Efficiency = 0.83

With these parameters, an on-design single-cycle analysis was carried out at sea level and Mach = 0 using GasTurb [15], in order to validate the engine's rated thrust against the manufacturer's performance specifications under standard atmospheric conditions. Results are shown in Table 13.

Table 13: GasTurb On-Design Results at Sea Level, Mach = 0

Station	**W (kg/s)**	**T (K)**	**P (kPa)**
Station 1	0.919	288.15	101.325
Station 2	0.919	288.15	100.312
Station 3	0.919	462.25	381.185
Station 4	0.834	1214.60	369.749
Station 5	0.926	999.56	183.069
Station 6	0.926	999.56	179.407
Station 8	0.926	999.56	179.407
Performance Parameters			
Thrust (FN)	0.51 kN		
TSFC	32.6164 g/(kN·s)		
Specific Thrust (FN/W2)	558.86 m/s		
Nozzle Exit Area (A8)	0.0042 m^2		
Fuel Flow (WF)	0.01674 kg/s		
Fuel-Air Ratio (far7)	0.01855		
Compressor Efficiency	0.7606		
Turbine Efficiency	0.8417		
Burner Efficiency	0.9999		

These results demonstrate that Gasturb [15] analysis is closer to the manufacturer specification. Then, parametric analysis was performed at 10k feet and Mach equal to 0.7, which is cruise properties. In Figure 14, the relationship of the compressor pressure ratio and specific thrust is shown.

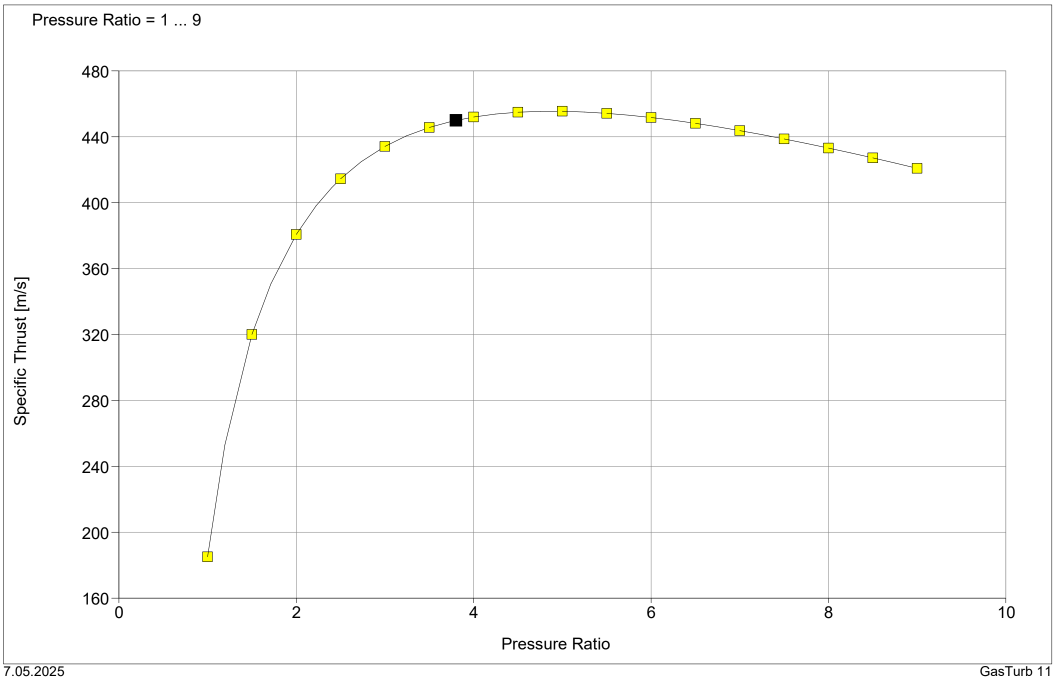

Figure 14: Compressor Pressure Ratio vs Specific Thrust

The black point symbolizes the design point, which is the pressure ratio equal 3.8 in this graph. As the compressor pressure ratio increases, the airflow entering the combustion chamber becomes more compressed. This condition enables more energy to be released from the same amount of fuel, resulting in higher exhaust velocity and increased specific thrust. However, beyond a certain pressure ratio, the burner exit (turbine inlet) temperature reaches its maximum allowable limit, which restricts further fuel addition. In addition, the compressor demands more power, requiring the turbine to extract more energy, leaving less energy for the exhaust jet. As a result, specific thrust starts to decrease slightly.

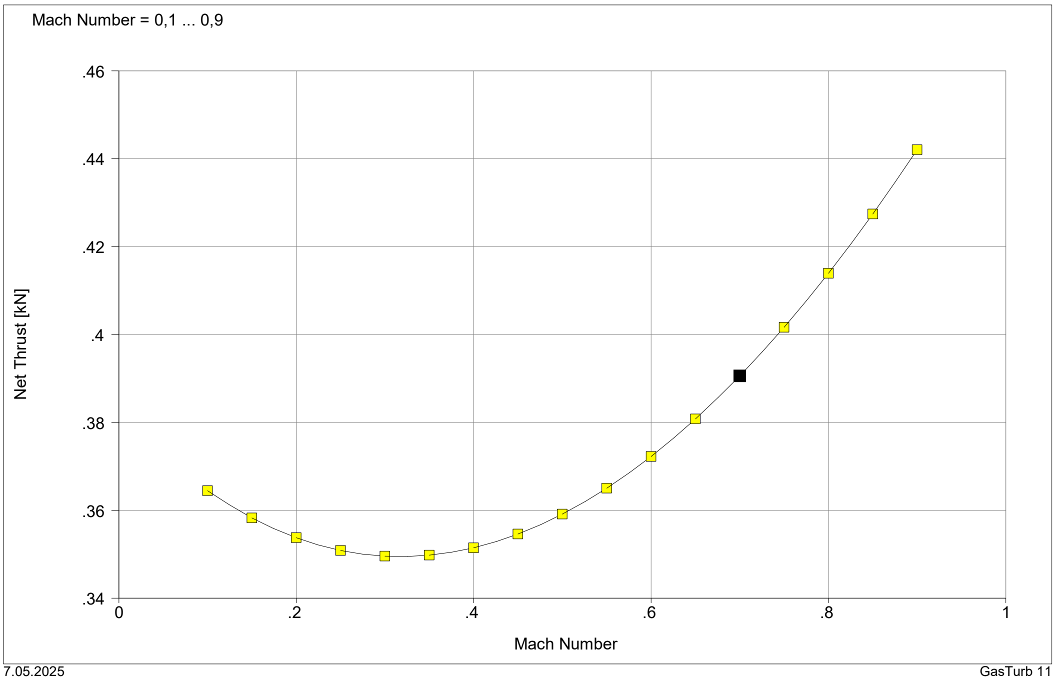

Figure 15: Mach vs Net Thrust

The Figure 15 illustrates the variation of net thrust with respect to Mach number. As seen in the graph, the net thrust decreases at low Mach numbers and then increases significantly beyond approximately 0.35 Mach. At the selected cruise speed of Mach 0.7, the engine is capable of generating sufficient thrust, indicating that the propulsion system can comfortably meet the thrust requirement during cruise.

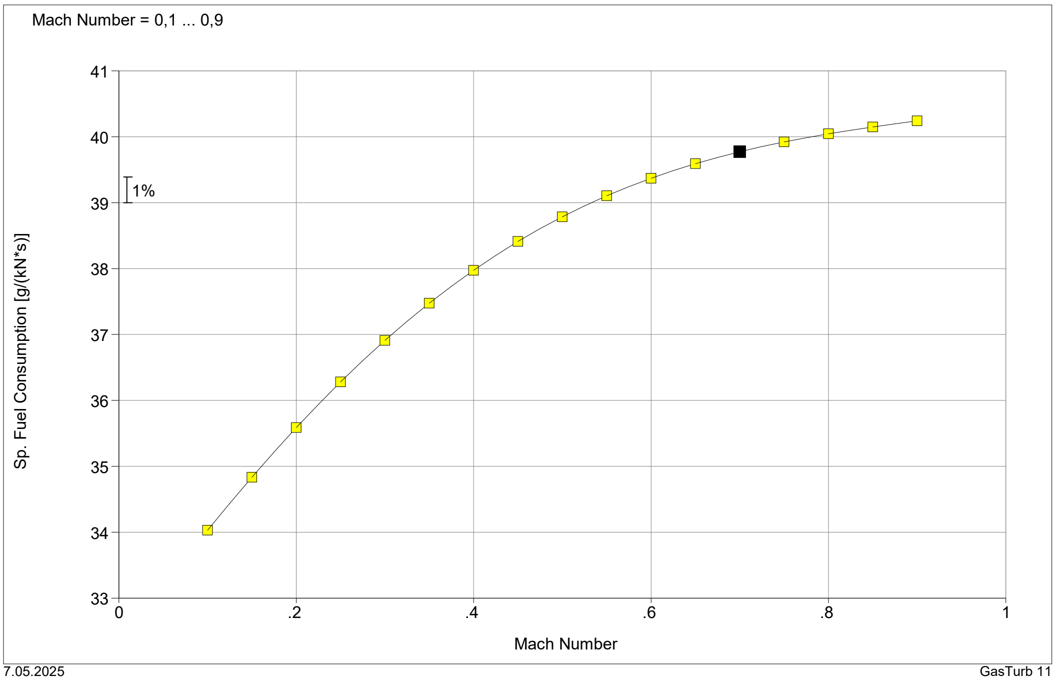

Figure 16: Mach vs Specific Fuel Consumption

Figure 16 shows the variation of specific fuel consumption with Mach number. As the Mach number increases, SFC also increases. Because at higher speeds, the amount of air entering the engine per unit time increases, and it leads to more compression in the compressor. As a result, more air enters the combustion chamber, which requires more fuel to efficient combustion.

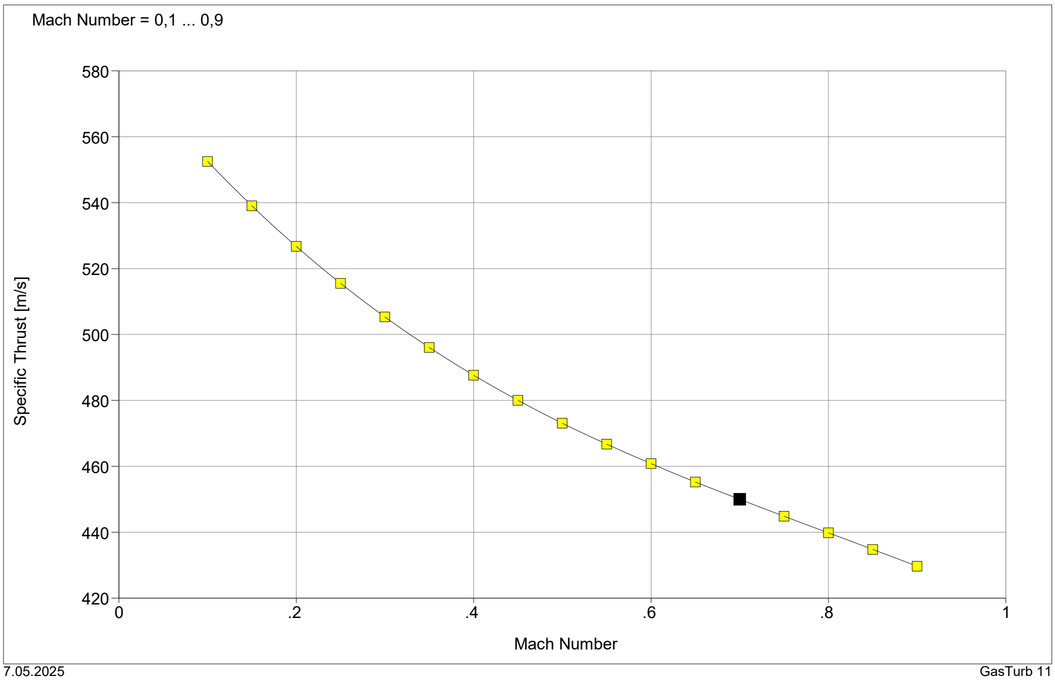

Figure 17: Mach vs Specific Thrust

Figure 17 shows the variation of the specific thrust with the Mach number. As the Mach number increases, specific thrust gradually decreases. This is mainly because higher Mach numbers result in a higher mass flow rate into the engine per unit time, while the net thrust does not increase at the same rate. As the freestream velocity increases, the difference between the exhaust and inlet velocities becomes smaller, which causes a reduction in net thrust. As a result, the ratio of thrust to incoming airflow, which is the specific thrust, decreases with increasing Mach number.

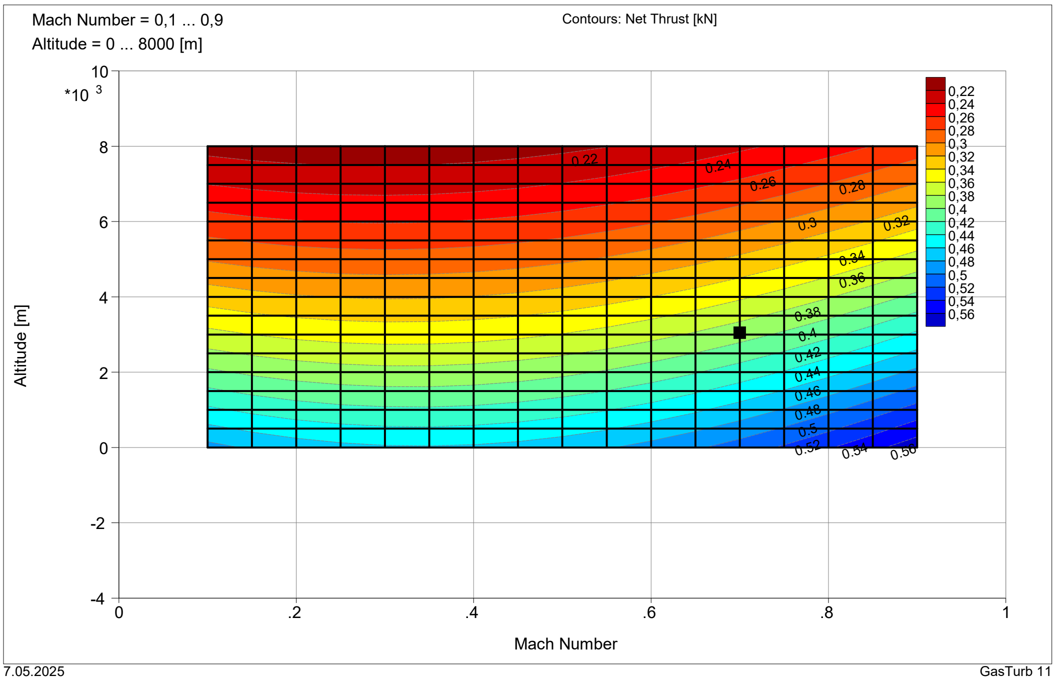

Figure 18: Variation of Net Thrust with Altitude and Mach Number

In Figure 18, the variation of net thrust with Mach number and altitude is presented in a contour plot. The figure clearly shows that net thrust decreases with increasing altitude due to the drop in air density, which limits mass flow through the engine. For a fixed altitude, increasing Mach number also reduces net thrust, as the engine imparts less additional momentum to the already fast incoming flow. This is because at higher speeds, the incoming velocity V_0 increases, and according to the thrust equation $F = \dot{m}(V_e - V_0)$ [17], the net thrust F decreases as the velocity difference becomes smaller. The overall trend indicates that maximum thrust is achieved at low altitude and high Mach numbers.

4.2.7 Estimation of Required Fuel

Accurate fuel estimation is critical to ensure that the aircraft can successfully complete its assigned mission. In addition, precise fuel calculations are essential to determine the net weight of the aircraft, which directly affects performance and balance. Fuel estimation was carried out on the basis of the mission profile which is determined by the control equip. Mission profile is shown in Figure 19.

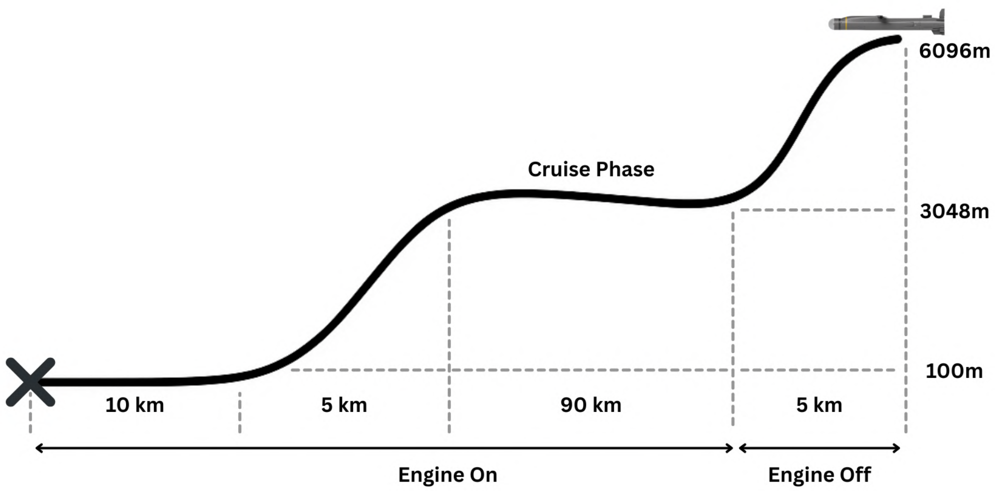

Figure 19: Cruise Missile Mission Profile

The mission profile is planned on the basis of fuel efficiency and long haul flight. Although the mission profile requires a minimum range of 100 km, the system was designed for a range of 110 km to ensure operational reliability and provide a safety margin. The missile leaves from aircraft at 20k feet, then it glides down to 10k feet. In this part of the mission, engine will be off. The 10k feet altitude is the cruise altitude, where the missile travels at 0.7 mach. After cruise, the missile descends to 330 feet, nearly sea level, and hits the target. The engine will provide minimum thrust in descent part, which means idle. Specific fuel consumptions for 10k feet and sea level altitude were obtained. The Figure 20 presents the comparison of specific fuel consumption at these two altitudes.

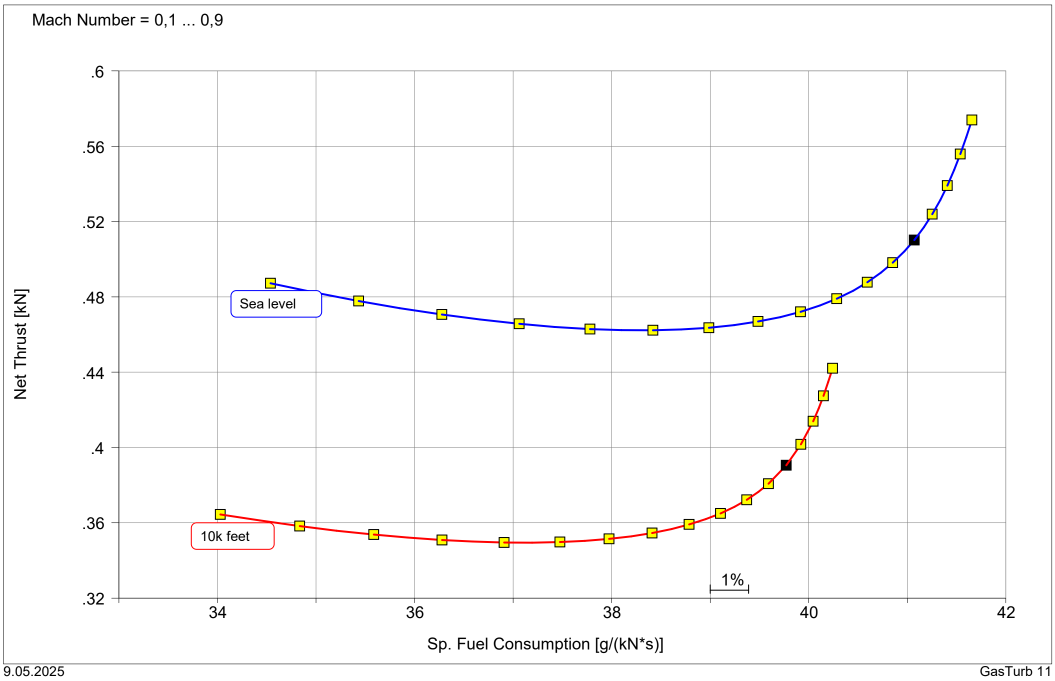

Figure 20: Specific Fuel Consumptions at Sea Level and 10k Ft

Table 14: Mach Number, Specific Fuel Consumption, and Net Thrust

Altitude	**Mach**	**SFC (g/kN·s)**	**Net Thrust (kN)**
Sea Level	0.7	41.1	0.51
10k Feet	0.7	39.8	0.39

The specific fuel consumptions at 0.7 Mach, sea level and 10k feet are given in Table 14. The estimation of required fuel was conducted on the basis of these parameters. The MATLAB [11] code of the required fuel calculation can be found in the Appendix.

Table 15: Fuel Consumption Based on Mission Profile

Phase	**Engine State**	**Fuel Used**	**Time**
Launch	Off	0.00 L	0.56 min
Cruise	Normal	7.50 L	6.53 min
Descent	Idle	0.11 L	0.36 min
Low-Alt Cruise	Normal	1.10 L	0.70 min
	Total:	**8.71 L**	**8.15 min**

As presented in the Table 15, the total flight duration was calculated as 8.15 minutes, and the total fuel consumption was found to be 8.71 liters. By applying a 25% correction margin to account for uncertainties and potential deviations, the final fuel requirement was determined as 11 liters.

This calculation method is based solely on engine performance data and can be considered a kind of worst-case estimation. It does not account for the aerodynamic characteristics of the missile. For comparison purposes, a second fuel consumption estimation was performed using the Breguet range equation [18], which incorporates the aerodynamic properties of the missile into the analysis. Breguet equation represented as [18]:

$$R = \frac{V}{c} \cdot \frac{C_L}{C_D} \cdot \ln\left(\frac{W_i}{W_f}\right) = \frac{V}{c} \cdot \frac{L}{D} \cdot \ln\left(\frac{W_i}{W_f}\right)$$

where R is the range of the missile or aircraft [m], V is the flight speed [m/s], L/D is the lift-to-drag ratio (also expressed as C_L/C_D), c is the specific fuel consumption [1/s], W_i and W_f are the initial and final weights respectively [kg], C_L is the lift coefficient, and C_D is the drag coefficient.

In this calculation, when the range R is taken as 100 km, the difference between initial and final weight is approximately 5.6 kg. Since the fuel used is Jet-A1, this corresponds to a fuel volume of approximately 6.65 liters. This equation shows that as the lift-to-drag ratio (L/D) increases, fuel consumption decreases. It also indicates that when aerodynamic properties are taken into account, the achievable range can increase under favorable conditions.

Given the parameters $V = 328.4$ m/s, $L/D = 3.01$, $c = 3.9 \times 10^{-4}$ 1/s, $W_i = 86.8$ kg, and $W_f = 78.0$ kg, the range is computed as:

$$R = \frac{V}{c} \cdot \frac{L}{D} \cdot \ln\left(\frac{W_i}{W_f}\right) = \frac{328.4 \times 3.01}{3.9 \times 10^{-4}} \ln\left(\frac{86.8}{78.0}\right) \approx 170 \text{ km}$$

When the total available fuel mass is inserted into the equation, the achievable range increases to approximately 170 km. This result highlights the importance of aerodynamic efficiency and shows that the system is capable of exceeding the 100 km baseline requirement under favorable conditions.

4.2.8 Intake Design for Cruise Missile

In this project, an inlet was designed to supply sufficient airflow to the turbojet engine under cruise conditions. The engine (JetCat P550) requires a mass flow rate of $\dot{m} = 0.93$ kg/s. At an altitude of 25,000 ft and a cruise speed of Mach 0.7, the air density is taken as $\rho = 0.549$ kg/m^3, and the freestream velocity is approximately $V = 223.5$ m/s.

Based on these values, the required inlet area was calculated as:

$$S_{\text{inlet}} = \frac{\dot{m}}{\rho \cdot V} = \frac{0.93}{0.549 \cdot 223.5} = 74.9 \text{ cm}^2 \tag{6}$$

Although the required inlet area was calculated as 74.9 cm^2, a slightly larger area of approximately 83 cm^2 was selected in the final design to account for potential errors and uncertainties in the estimation process.

The inlet geometry was selected as a filleted elliptical opening, partially embedded into the missile's upper fuselage. Although semi-circular and slot geometries were considered in early design stages, the elliptical form was preferred due to its smoother aerodynamic characteristics and better structural integration.The final inlet design can see in the Figure 21. The CAD drawings has completed with Solid Edge software [19].

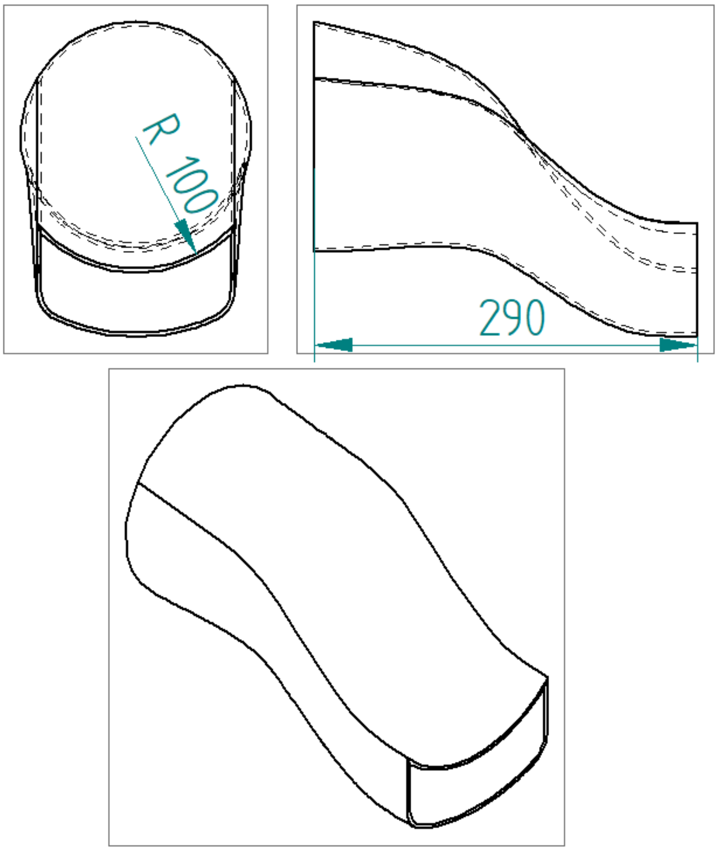

Figure 21: Three-view CAD sketch of the inlet design

Due to internal space limitations, the duct length was restricted to 290 mm. However, full s-duct shape was implemented. The duct was shaped to minimize flow separation and swirl, while ensuring that the required mass flow reaches the engine face [20]. Also dual side inlets were not used, as they would increase local flow disturbances that could affect the aerodynamic performance of the "+" shaped tail fin arrangement Figure 22. The overall inlet configuration was influenced by real-world cruise missile systems. The Naval Strike Missile [21], Storm Shadow [22]

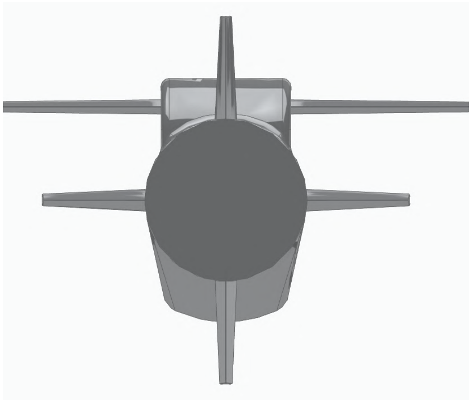

Figure 22: Back view of our Missile

all utilize embedded or semi-flush inlet designs that combine stealth characteristics with aerodynamic efficiency Figure 23. These references informed the design direction, especially regarding inlet placement, blended fuselage integration, and internal channel transitions. As a result, the final view of our inlet design can see in Figure 24a-24b.

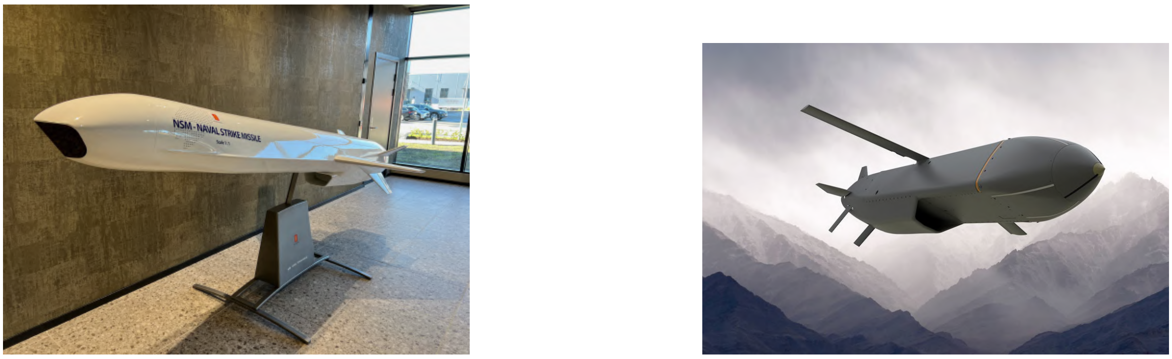

(a) Inlet design of the Naval Strike Missile [21]

(b) Inlet design of the Storm Shadow missile [22]

Figure 23: Examples of inlet geometries from real cruise missiles

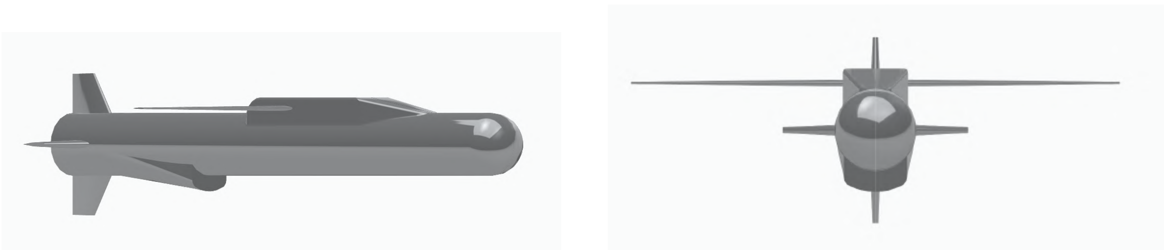

(a) Isometric view of our Missile

(b) Front view of our Missile

Figure 24: Our Missile

4.3 Guidance, Navigation, and Control (GNC)

4.3.1 Objective of the GNC Team

The main objective of the Guidance, Navigation, and Control (GNC) team is to design and develop a flight control system for the cruise missile in order to ensure accurate target engagement and stable flight performance.

4.3.2 Scope of the GNC Team

The scope of the GNC team in this project covers the design, modeling, and control of the guidance and control systems of the missile. The developed GNC system is expected to ensure the stability of the missile during flight, hit the target within predetermined tolerances, and withstand external disturbances that may be encountered along the trajectory to the target.
The tasks covered within the scope of the project are explained below:

1. **Coordinate Transformations:** Performing transformations between Body, NED, and ECEF reference frames, taking the Earth's rotation into account.
2. **Dynamic Modeling:** Developing a 6-DOF (Six Degrees of Freedom) dynamic model of the missile to represent its motion accurately.
3. **Controller Design:** Designing appropriate control algorithms to stabilize and maneuver the missile effectively.
4. **Guidance Algorithm:** Developing guidance strategies to direct the missile towards the target within the specified tolerances.
5. **Sensor Selection:** Selecting sensors compatible with the mission profile and considering cost-effectiveness.
6. **Actuator Modeling:** Including and modeling the actuators used in the control system.
7. **Verification and Performance Analysis:** Verifying the designed system and evaluating its performance using MATLAB/Simulink simulations.

4.3.3 GNC Performance Requirements

Table 16: GNC Performance Requirements

Category	Performance Requirement
Range	$\geq$ 100 km operational range
Accuracy (CEP)	$\leq$ 10 m Circular Error Probable
Flight Altitude	Minimum 100 m , Maximum 6000 m
Speed	Cruise Mach 0.7
Guidance	INS/GPS-based navigation and Imaging Infrared (IIR) seeker for terminal guidance

The main performance requirements for the GNC system are summarized in Table 16. These parameters directly affect the missile's guidance accuracy, stability, and overall mission success.

4.3.4 Trajectory and Flight Profile

The flight profile is designed to fulfill the mission requirements and ensure successful target engagement. The trajectory of the cruise missile consists of five main phases: Launch Phase, Cruise Phase, Descent Phase, Low-Altitude Cruise Phase, and Terminal Phase [23].

1. **Launch Phase:** The cruise missile will be released from an aerial platform. The launch altitude is selected as 6000 m (20,000 ft) based on the typical cruising altitude of UAVs. After release, the missile will perform a turning maneuver and descend to an altitude of 3000 m (10,000 ft).

2. **Cruising Phase:** After reaching 3000 m (10,000 ft), the missile will maintain a steady cruising speed between Mach 0.6 and Mach 0.7. During this phase, GPS and INS systems will be used to maintain navigation accuracy.

3. **Descent Phase:** In this phase, the missile will descend to an altitude of 100 m to save fuel and avoid detection by high-altitude radar systems.

4. **Low-Altitude Cruise Phase:** After stabilizing at 100 m altitude, the missile will continue to navigate towards the target at approximately Mach 0.7 using GPS and INS data until the terminal phase is reached.

5. **Terminal Phase:** In the final phase, the IIR (Imaging Infrared) seeker will be activated, enabling the missile to track and engage the target with high accuracy.

The overall flight profile is shown in Figure 25.

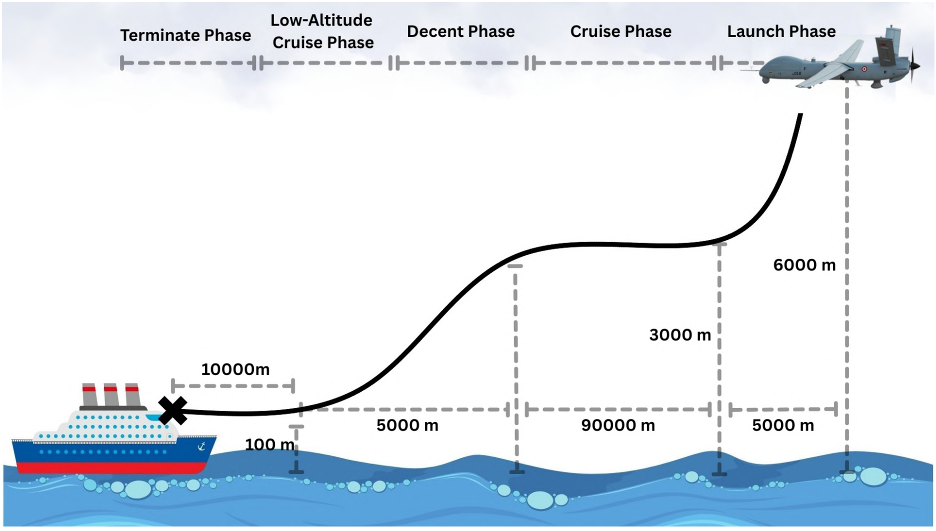

Figure 25: Representative flight profile of the designed cruise missile.

4.3.5 Guidance Architecture

Guidance Method

Guidance is the means by which a missile steers, or is steered, to a target. A guided missile is guided according to a certain guidance law. A meaningful comparison of homing guidance systems for missiles requires realistic models for the missile and its target engagement geometry model in order for terminal miss distance to be accurately evaluated. This model should include the important dynamics and system nonlinearities that influence performance, and yet be representative of missiles in general [24].

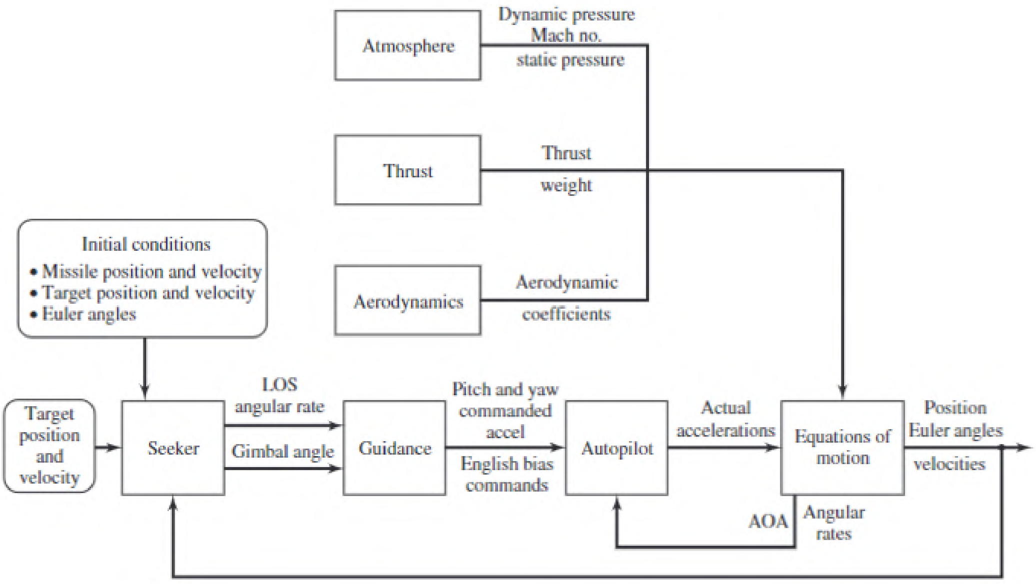

Figure 26: The Cruise Missile System Guidance Block Diagram [24]

Guidance system's inputs are error angles in both pitch and yaw planes. Guidance system makes some estimation and creates the necessary position values for the missile in order to give the directions for the target's next position. The most popular navigation guide method is proportional navigation guide (PNG). In this missile system, the proportional navigation guide method was taken into consideration when selecting the guide method [25]. This study chose proportional navigation guide (PNG) method for its simplicity, low computational load, and established effectiveness in air-to-air and surface-to-air missile engagements. The proportional navigation guidance law issues acceleration commands perpendicular to the instantaneous missile target line of sight, which is proportional to the line of sight rate and closing velocity.The line of sight (LOS) that passes through the objective of the guidance is an important concept of guidance [26]. In missile guidance line of sight (LOS) is the line directly between the launcher/tacker and the target, which must be in view. PNG is expressed in the mathematical formulation as:

$$a_c = N \cdot V_c \cdot \dot{\lambda}$$

- a_c : Commanded lateral acceleration (m/s^2)
- N : Navigation constant (dimensionless, typically 3–5)
- V_c : Closing velocity between missile and target (m/s)
- $\dot{\lambda}$: Rate of change of LOS angle (rad/s)

Sensors

The guidance system relies heavily on precise, timely, and robust sensor data to maintain effective trajectory correction. The following sensor types were integrated or considered within the system framework:

1. Inertial Measurement Unit (IMU): Measures linear accelerations and angular velocities using accelerometers and gyroscopes. IMU data provides short term navigation and high frequency updates, which are crucial for stability and dynamic tracking.

2. Global Positioning System (GPS): Provides global position and velocity information, mainly supporting mid course guidance. While susceptible to signal loss or jamming, GPS complements IMU by correcting long term drift errors.

3. Imaging Infrared (IIR) Seekers: Advanced type of IR seekers that provide 2D or 3D imaging of the target area. They allow for better target discrimination, resistance to countermeasures, and more accurate homing, especially in cluttered environments. IIR seekers are often coupled with onboard processors using scene matching algorithms.

4.3.6 Missile System Model Design

Missile system model consists of different parts within its mathematical structure. In this section, we will develop these models both mathematically and in the Simulink environment. Firstly, we will start with the coordinate frames and then continue with the 6-DOF model. In the following sections, the mathematical model of each part will be derived and its corresponding Simulink implementation will be presented.

Coordinate Systems

Coordinate frames are critical for the whole model as they affect the entire structure. We will start with the body frame, and then we will obtain the NED frame to get the positions based on latitude and longitude. From there, to include the Earth's rotation effect, we will pass to the ECEF frame. These frames are briefly explained below, along with their corresponding DCM models.

1. **Body Frame:** The body frame is a coordinate system fixed to the missile's center of gravity. Its axes are defined as:
   - X_b: Forward along the longitudinal axis
   - Y_b: Right along the lateral axis
   - Z_b: Downward along the vertical axis
2. **NED Frame:** A local level frame tangent to the Earth's surface. Its axes are defined as follows:
   - X_n: True North direction (forward)
   - Y_n: East direction (right)
   - Z_n: Downward (towards Earth's center)
3. **ECEF Frame:** A rotating Earth fixed frame that rotates with the Earth and is used to represent positions relative to the Earth's surface. The origin of the ECEF frame is located at the center of the Earth.

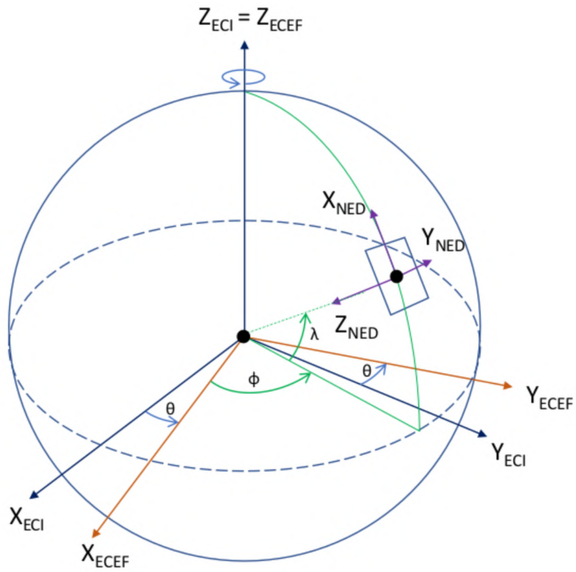

Figure 27: Transformation between Earth-Centered Inertial (ECI), Earth Centered Earth Fixed (ECEF), and North East Down (NED) coordinate systems [27].

Body to NED Transformation Matrix:

The transformation matrix from Body frame to NED frame is given as:

$$R_B^N = \begin{bmatrix} \cos\theta\cos\psi & \cos\theta\sin\psi & -\sin\theta \\ \sin\phi\sin\theta\cos\psi - \cos\phi\sin\psi & \sin\phi\sin\theta\sin\psi + \cos\phi\cos\psi & \sin\phi\cos\theta \\ \cos\phi\sin\theta\cos\psi + \sin\phi\sin\psi & \cos\phi\sin\theta\sin\psi - \sin\phi\cos\psi & \cos\phi\cos\theta \end{bmatrix} \tag{7}$$

NED to ECEF Transformation Matrix:

Latitude: ϕ Longitude: λ

The transformation matrix from NED frame to ECEF frame is given as:

$$DCM_{ne} = \begin{bmatrix} -\sin\lambda\cos\phi & -\sin\lambda\sin\phi & \cos\lambda \\ -\sin\phi & \cos\phi & 0 \\ -\cos\lambda\cos\phi & -\cos\lambda\sin\phi & -\sin\lambda \end{bmatrix} \tag{8}$$

6-DOF Missile Model

The mathematical model of the missile is represented by a 6-DOF (Six Degrees of Freedom) system, which is categorized into three main groups: Force Equations, Moment Equations, and Kinematic Relations. The detailed mathematical expressions of these equations are presented below.

Force Equations

$$
\begin{aligned}
m(\dot{U} + QW - RV) &= FG_x + FA_x + FT_x \\
m(\dot{V} + RU - PW) &= FG_y + FA_y + FT_y \\
m(\dot{W} + PV - QU) &= FG_z + FA_z + FT_z
\end{aligned} \tag{9}
$$

Moment Equations

$$
\begin{aligned}
I_x \cdot \dot{p} + (I_z - I_y) \cdot q \cdot r &= L \\
I_y \cdot \dot{q} + (I_x - I_z) \cdot p \cdot r &= M \\
I_z \cdot \dot{r} + (I_y - I_x) \cdot p \cdot q &= N
\end{aligned} \tag{10}
$$

Euler Angle Relations

The angular rates in the body axes are expressed in terms of the derivatives of Euler angles as follows:

$$
\begin{aligned}
P &= -\sin(\Phi) \cdot \dot{\psi} + \cos(\Phi) \cdot \dot{\theta} + \dot{\Phi} \\
Q &= \sin(\Phi) \cdot \cos(\theta) \cdot \dot{\psi} + \cos(\Phi) \cdot \dot{\theta} \\
R &= \cos(\Phi) \cdot \cos(\theta) \cdot \dot{\psi} - \sin(\Phi) \cdot \dot{\theta}
\end{aligned} \tag{11}
$$

Velocity Relations in ECEF Frame

The position derivatives in the North East Down (NED) frame are calculated using the following relations:

$$
\begin{aligned}
\dot{x}^E &= u\cos\theta\cos\psi + v(\sin\phi\sin\theta\cos\psi - \cos\phi\sin\psi) + w(\cos\phi\sin\theta\cos\psi + \sin\phi\sin\psi) \\
\dot{y}^E &= u\cos\theta\sin\psi + v(\sin\phi\sin\theta\sin\psi + \cos\phi\cos\psi) + w(\cos\phi\sin\theta\sin\psi - \sin\phi\cos\psi) \\
\dot{z}^E &= -u\sin\theta + v\sin\phi\cos\theta + w\cos\phi\cos\theta
\end{aligned} \tag{12}
$$

The developed 6-DOF missile model is implemented in MATLAB/Simulink environment. The block diagram of the model is presented in Figure 28.

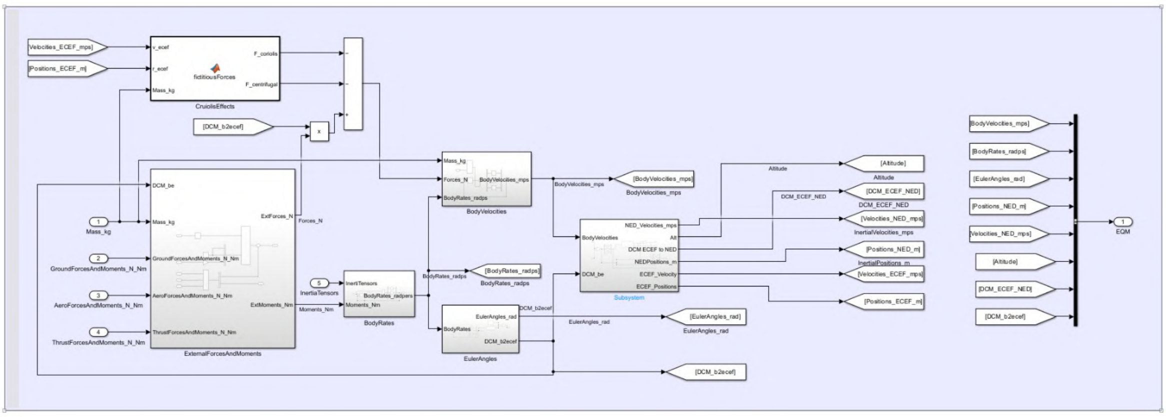

Figure 28: The developed 6-DOF missile model in Simulink environment.

Atmospheric Model

ISA (International Standard Atmosphere) Mathematical Model:

For Troposphere ($h \leq 11\,km$):

$$T(h) = T_0 - L \cdot h \tag{13}$$

$$P(h) = P_0 \left(\frac{T(h)}{T_0} \right)^{\frac{g}{L \cdot R}} \tag{14}$$

$$\rho(h) = \frac{P(h)}{R \cdot T(h)} \tag{15}$$

Where:

$T_0 = 288.15\,K$, $P_0 = 101325\,Pa$, $L = 0.0065\,K/m$, $g = 9.80665\,m/s^2$, $R = 287.05\,J/kgK$

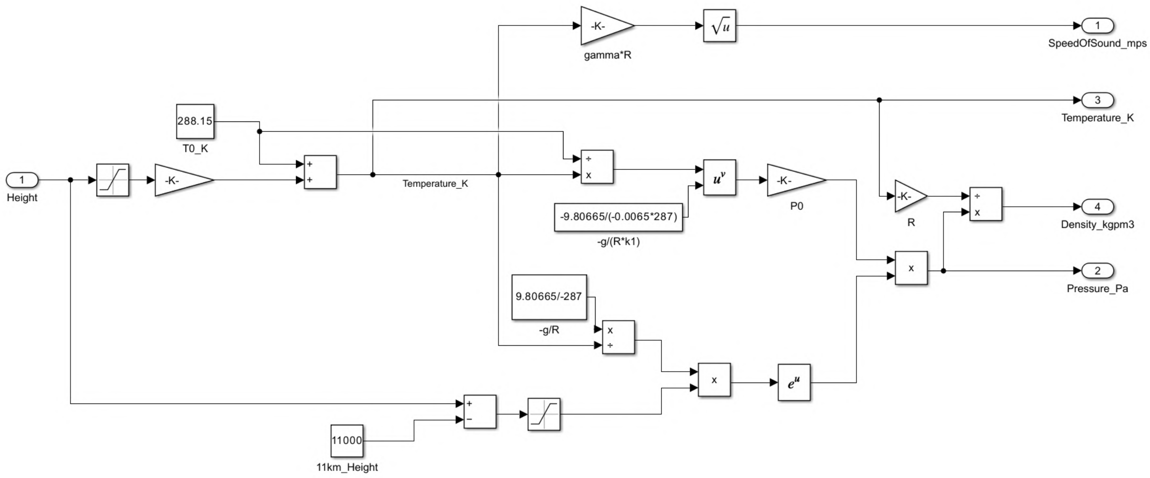

Figure 29: Atmosphere Model

Aerodynamic Model

The aerodynamic model aims to calculate the aerodynamic forces and moments acting on the missile during its flight. In order to obtain these forces and moments, aerodynamic coefficients must be defined properly.

In this study, the aerodynamic model is constructed based on the formulations provided in Yechout's reference book. Aerodynamic forces are considered along the X, Y, Z axes, and moments are considered around the L, M, N axes.

Although aerodynamic coefficients can be defined in various ways, in this project, the classical Taylor series expansion method is preferred to avoid multiple transformations and to ensure compatibility with the aerodynamic team's analysis capabilities.

In the aerodynamic analysis, the necessary coefficients were obtained using data from MISSILE DATCOM. By default, MISSILE DATCOM provides force and moment outputs in the axial (A), normal (N), and side (Y) directions for forces, and L, M, N for moments. Instead of modifying the 6-DOF ECEF block, an intermediate transformation was applied to convert these outputs into the standard X, Y, Z (forces) and L, M, N (moments) format. The forces and moments were accordingly referenced to the specified coordinate system.

Aerodynamic Forces

$$
\begin{aligned}
X &= C_x(\bar{q}S) \\
Y &= C_y(\bar{q}S) \\
Z &= C_z(\bar{q}S)
\end{aligned}
\tag{16}
$$

Aerodynamic Moments

$$
\begin{aligned}
L &= C_l(\bar{q}Sb) \\
M &= C_m(\bar{q}S\bar{c}) \\
N &= C_n(\bar{q}Sb)
\end{aligned}
\tag{17}
$$

Based on the Taylor expansion, the aerodynamic force and moment coefficients are expressed as follows:

Force Coefficients

$$
\begin{aligned}
C_x &= C_{x0} + C_{x\alpha}\alpha + C_{x\beta}\beta + C_{x\delta_a}\delta_a + C_{x\delta_e}\delta_e + C_{x\delta_r}\delta_r \\
C_y &= C_{y0} + C_{y\alpha}\alpha + C_{y\beta}\beta + C_{y\delta_a}\delta_a + C_{y\delta_e}\delta_e + C_{y\delta_r}\delta_r \\
C_z &= C_{z0} + C_{z\alpha}\alpha + C_{z\beta}\beta + C_{z\delta_a}\delta_a + C_{z\delta_e}\delta_e + C_{z\delta_r}\delta_r
\end{aligned}
\tag{18}
$$

Moment Coefficients

$$
\begin{aligned}
C_l &= C_{l0} + C_{l\alpha}\alpha + C_{l\beta}\beta + C_{lp}\frac{pb}{2V} + C_{lq}\frac{qc}{2V} + C_{lr}\frac{rb}{2V} + C_{l\delta_a}\delta_a + C_{l\delta_e}\delta_e + C_{l\delta_r}\delta_r \\
C_m &= C_{m0} + C_{m\alpha}\alpha + C_{m\beta}\beta + C_{mp}\frac{pb}{2V} + C_{mq}\frac{qc}{2V} + C_{mr}\frac{rb}{2V} + C_{m\delta_a}\delta_a + C_{m\delta_e}\delta_e + C_{m\delta_r}\delta_r \\
C_n &= C_{n0} + C_{n\alpha}\alpha + C_{n\beta}\beta + C_{np}\frac{pb}{2V} + C_{nq}\frac{qc}{2V} + C_{nr}\frac{rb}{2V} + C_{n\delta_a}\delta_a + C_{n\delta_e}\delta_e + C_{n\delta_r}\delta_r
\end{aligned} \tag{19}
$$

The developed aerodynamic missile model is implemented in MATLAB/Simulink [28] environment. The block diagram of the model is presented in Figure 28.

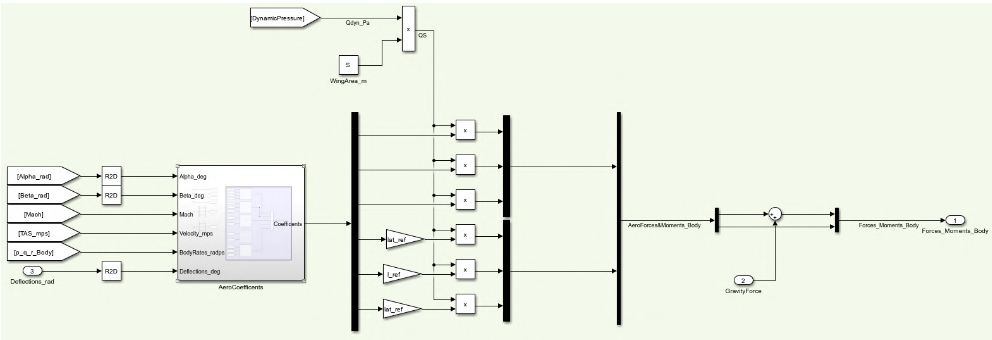

Figure 30: Aerodynamic force calculation model in Simulink environment.

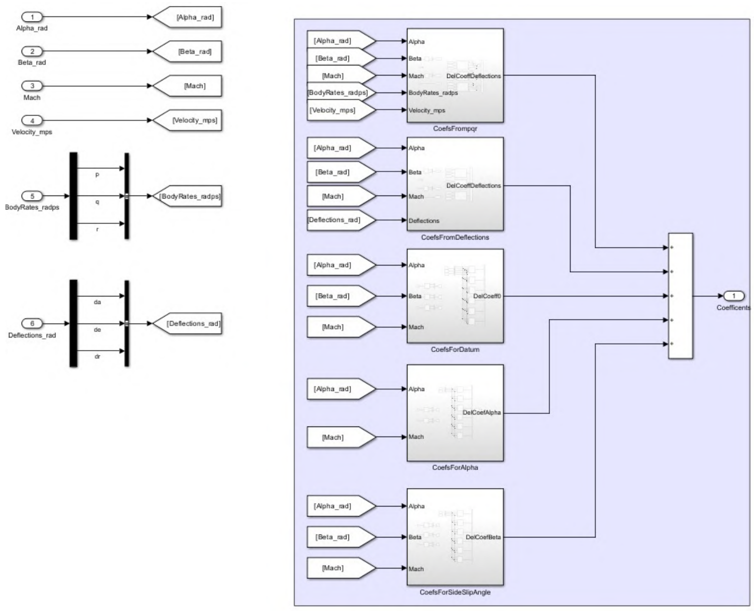

Figure 31: Aerodynamic moment calculation model in Simulink environment.

Propulsion Model

A propulsion model based on angle of attack (alpha) was developed using the data provided by the propulsion team. The model takes throttle ratio as its input.

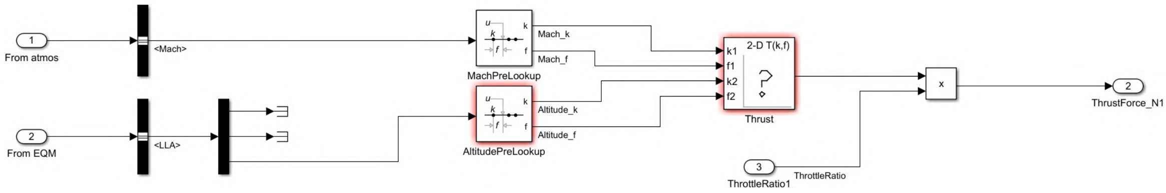

Figure 32: Propulsion model in Simulink environment.

4.3.7 Control Algorithm Design

Before conducting a full trim analysis, a cruise trim analysis was performed to observe whether the air vehicle was capable of straight and level flight. Based on the results of this analysis, the flight was simulated using FlightGear, as illustrated in Figure 33.

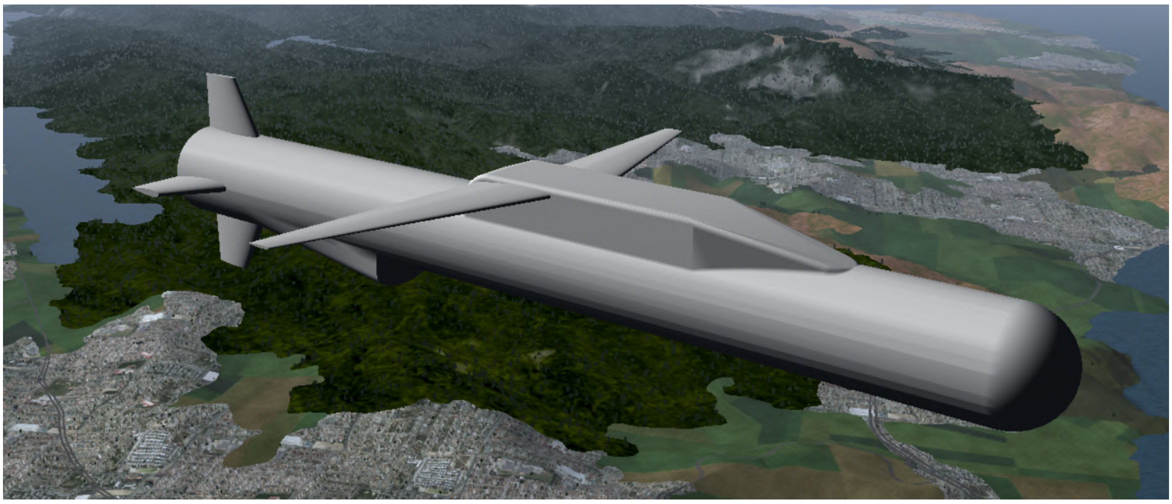

Figure 33: Missile model in FlightGear [29].

To design the controller, firstly we derive the nonlinear full system and perform trim analysis based on cruise conditions to obtain the trim situation. After the trim analysis, we will linearize the whole system to understand the system behavior without the controller. Then, we can design the controller for the system. For now, we have not started the controller design yet.

4.4 Payload

4.4.1 Payload Configuration

In this missile system, the payload consists of a high effect warhead used to neutralize the target. The warhead is the section containing explosives or effective substances designed to damage the target. The primary objective is to destroy or disable the target [30].

4.4.2 Warhead Selection

The starting point in warhead selection is the identification of the target. This selection is made based on and is obtained with the help of the table below.

Code	Target Type	Description
HAA	High Altitude Air Targets	Turbojet, turboprop, piston-engine aircraft; turbojet, ramjet, and rocket-engine missiles.
LAA	Low Altitude Air Targets	HAA targets plus helicopters and airships.
CHS	Concentrated Hard Surface Targets	Concrete bunkers, armored vehicles, fortifications, tunnels/passages, dams, warships, destroyers, heavy artillery positions, concrete bridges.
CSS	Concentrated Soft Surface Targets	Trucks, locomotives, cargo ships, tankers, landing vehicles, grounded aircraft, individual industrial buildings, wooden bridges.

Table 17: Target Types and Descriptions [31]

As can be seen from the table, our naval target falls within the scope of the CHS.But this type of target can be treated as being in the common domain of CHS and CSS. Based on this information, a new elimination will be carried out using another table below.

Target Classification	Guidance Error (ft)	Warhead Weight (lbs)				
		<25	25-100	100-300	300-600	>600
HAA (High Altitude Aerial)	less than 30	SC* EB	SC* CR* FR	FR* CL	FR* CL*	FR* CL*
	30-60	CR FR	FR* CR* FR* CL*	FR* CL	FR* CL*	FR* CL*
	more than 60	CL* FR*	CR FR CL	FR* CL	FR* CL*	FR* CL*
LAA (Low Altitude Aerial)	less than 30	SC* EB	EB* SC* EB* CL	CR	EB	EB* CL
	30-60	EB SC	EB* CR	CR	EB	EB* CL
	more than 60	CL	EB* CR	EB CR	EB	EB* CL
CHS (Concentrated Hard Surface)	less than 30	SC	SC	SC* IB	IB	EB
	30-60	SC	SC	IB*	IB*	EB
	more than 60	IB	IB	SC* IB	IB	EB
CSS (Concentrated Soft Surface)	less than 30	FR*IB*	FR*IB*	FR* IB	FR*IB*	EB
	30-60	FR	FR	FR* EB	FR*EB*	EB CL
	more than 60	FR*	FR*	FR* EB	FR*EB*	EB CL

SC: Shaped Charge EB: External Blast
CR: Continuous Rod FR: Fragmentation
CL: Cluster IB: Internal Blast
DR: Discrete Rod *: More Likely Selections

Table 18: Warhead Effectiveness by Weight, Guidance Error, and Target Type [31]

Accordingly, we determine that our missile should be of the FR (Fragmentation),IR (Internal Blast) and SC (Shaped Charge) type, with a standard error of guidance less than 30 feet.

In addition to this information, the types of warheads used in similar missiles are presented below.

Missile Name	Type	Warhead Type	Warhead Weight (kg)	Total Weight (kg)
Apache	Air-to-Ground Cruise Missile	Thermobaric (Bunker Buster)	~350	~1230
SOM	Air-to-Ground Cruise Missile	Fragmentation / Penetrator	~230	600
Naval Strike Missile	Anti-Ship Cruise Missile	High Explosive (HE-FRAG)	~120	407
Delilah	Air-to-Ground Cruise Missile	High Explosive	~30	187
Spear 3	Air-to-Ground Mini Cruise Missile	High Explosive (HE)	~10	~100

Table 19: Selected Cruise Missiles and Their Specifications

Upon examining the above table and the previously provided information, it is recommended that the warhead type should be high-explosive, fragmentation-effective, and thermobaric as a special requirement.

Considering that the warhead generally constitutes 10–30% of the total mass of the missile, a warhead in the range of 10–20 kg is considered suitable for the rocket. Below are some warheads that can serve this purpose.

Note: Most of the information provided is estimative, as such data is not available in accessible libraries due to military confidentiality.

Name	Weight (kg)	Type	Diameter (mm)	Length (mm)	Cost ($)
OFAB-100-120	18.5	HE/FR	180	425	20,000
S-8KOM	11.3	Heat-FR	80	1537	35,000
Rafael SPIKE ER2	20	HE / Tandem HEAT	170	450	40,000

Table 20: Selected Missile Specifications

Considering all these and the requirements for the missile, the most suitable warhead was selected as the OFAB-100-120.

4.4.3 Weight Distribution

Component	**Weight (kg)**	**Distance from nose tip (mm)**
Propulsion System	5.4	1784.5
Fuel Tank + fuel (kerosene)	15.0	927
Warhead	18.5	475
Guidance System (IMU)	2.0	90
GPS (Ardupilot Cube)	3.96	203
Imaging Infrared (IIR)	0.2	28
Processor (NVIDIA Jetson Nano)	0.6	157
Navigation (Ardupilot Cube)	0.2	249
Control Actuators	4.0	1882.7
Battery	3.0	1314
Fin	2.8	1882.7
Fuze	1.0	317
Wing	4.0	1197
Fuselage Structure	27.0	967
Intake	1.2	1436
Total	**86.3**	

Table 21: Component Weight and Location Data.

Based on this data, the center of gravity of the cruise missile has been determined as $X_{CG} = 911.8$ mm from the nose tip, as shown in Figure 34.

$$X_{CG} = \frac{\sum(weight \times length)}{\sum weight} = 911.8\,\text{mm} \tag{20}$$

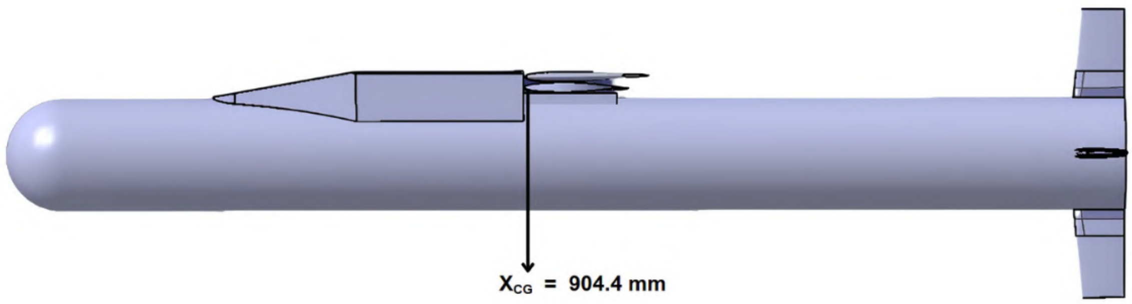

Figure 34: Center of Gravity Location of the Cruise Missile.

4.4.4 Delivery Mechanisms

Missile Launch and Initiation System

The missile is launched from an aircraft. At the moment of release, speed and directional stability are crucial. The aircraft must be at an appropriate speed and altitude to ensure the missile is released smoothly.

Guidance and Targeting

Missile guidance is provided by an Inertial Navigation System (INS) and a Global Positioning System (GPS) [32]. In the INS, sensors inside the missile continuously measure speed, acceleration, and direction and update these data throughout the flight. With GPS, the missile determines its position using satellite signals and follows the most efficient path to the target [33].

The missile is steered using aerodynamic surfaces, such as wings or stabilizers. These surfaces maintain the missile's balance during flight and keep it aligned with the target. They are constantly adjusted during flight to keep the missile on the correct path.

Detonation or Impact Mechanisms

A proximity sensor is considered for detonation. In this method, as the missile approaches the target, the proximity sensor activates and triggers detonation at a certain distance. This method is chosen for its ability to account for the movement of the target, making it ideal for large, mobile targets such as ships [34].

Payload Delivery and Drop Systems

This section covers the missile's release from the aircraft and its guidance towards the target.

a)Payload Delivery Systems: These systems are used for securely attaching and transporting the missile on the air platform. They ensure that the missile is positioned stably during flight. The payload delivery systems reviewed include Hardpoint/Pylon, BRU (Bomb Release Unit),and MER-TER (Multi-Ejector Rack and Triple-Ejector Rack). Among these systems, the combination of BRU and Pylon is considered the most ideal. The Pylon system provides safe transport and ease of control, while the BRU offers precise release control, adding extra security and compatibility [35]. If the possibility of firing multiple missiles simultaneously is considered, the TER/MER systems may be used.

b)Drop Systems: These systems are responsible for releasing the missile from the air platform and guiding it towards the target. In this context, Gravity Release was considered but eliminated due to its weak guidance capabilities. Pyrotechnic Ejection was found too aggressive due to the rapid separation it creates, and Rail Launch was disregarded because it is suitable for air-to-air targets [36]. The most suitable drop system, due to its safe operation at high speeds and no damage to the guidance system, is Pneumatic Ejection [37].

c)Final Configuration: Thus,the BRU is attached to the pylon under the aircraft, the missile is placed on the BRU, it is gently separated using the pneumatic system, and then guided by GPS.

4.5 Materials and Structures

4.5.1 Material Selection

There are 3 main components in a cruise missile. These components are the fuselage, wing and fins respectively. In order to prevent problems such as internal mechanism organization and component access in case of failure, the fuselage is selected as a semi-monocoque. Therefore, the sub-components in the fuselage are frame and stringers. Due to the airfoil chosen by the aerodynamics team, the fins and the tip of the wings are extremely thin, making these main components unsuitable for the rib, spar and skin structure. Therefore, wings and fins are monocoque without sub-component system.

The loads that the main components will be exposed to in the air are important for material selection. During the flight, the cruise missile is subjected to surface loads including aerodynamic and air pressure on the skin and body forces including gravity and inertia loads. As a result of surface loads and body forces, shear, tension, torsion and compression load types are observed in the cruise missile structure.

Because of the pressure distribution on the fuselage, compression occurs at the lower part of the fuselage and tension at the upper fuselage. While shear loads occur along the entire fuselage, bending stress occurs in the fuselage with the upward movement of the wings as a result of lift. Torsional loads occur as a result of pitch, roll and yaw movements. Due to altitude change, hoop stress occurs in the fuselage.

As a result of the lift load distribution on the wing, compression and tension occur around the wing. The combination of these loads and the fixing of the wings to the fuselage results in bending load. Shear load and torsion loads are observed on the entire wing.

The control surfaces of the cruise missile are the fins. Bending, torsion, compression and tension loads also occur on the fins for similar reasons as on the wing and fuselage.

Fuselage materials should have high stiffness and strength properties. Considering the mass production of cruise missiles, the selected materials should have high corrosion resistance. It is important for cruise missiles to choose materials with good thermal properties. The requirements for wing and fin materials are similar to those of the fuselage. Stiffness and strength values of the materials should be high to prevent bending and torsion loads. In addition, wing materials should be selected to have damage resistance against bird strikes [38].

The materials used in the aviation industry are generally aluminum, titanium and steel alloys and composites [39]. Material selection was made by examining Young's modulus-density, strength density and cost strength charts through asbhy diagrams.

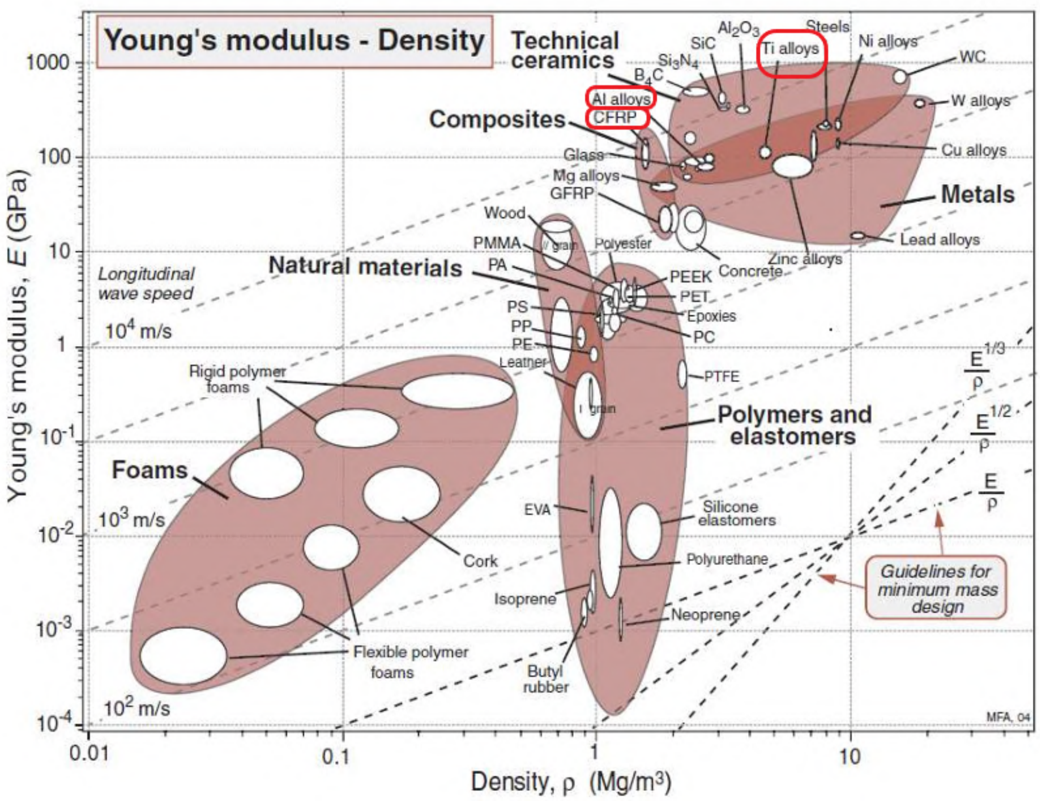

Figure 35: Young's modulus vs Density [40].

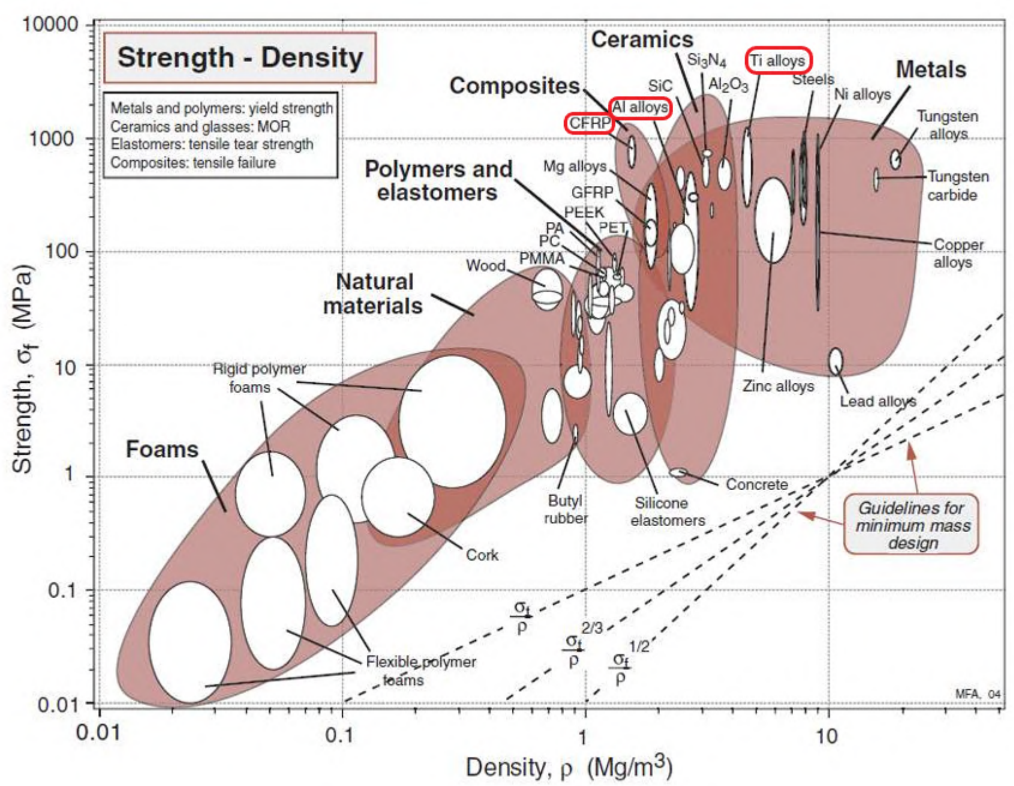

Figure 36: Strength vs Density [40].

High elastic modulus affects the stiffness value of the material. For the same elastic modulus values, materials with lower density come to the fore. As shown in Figure 35, CFRP has lower density and higher elastic modulus than Al alloys and Ti alloys. Since Ti alloys are high density materials, they cause the components to be heavy. Al alloys have low elastic modulus and average density value compared to the other two materials.

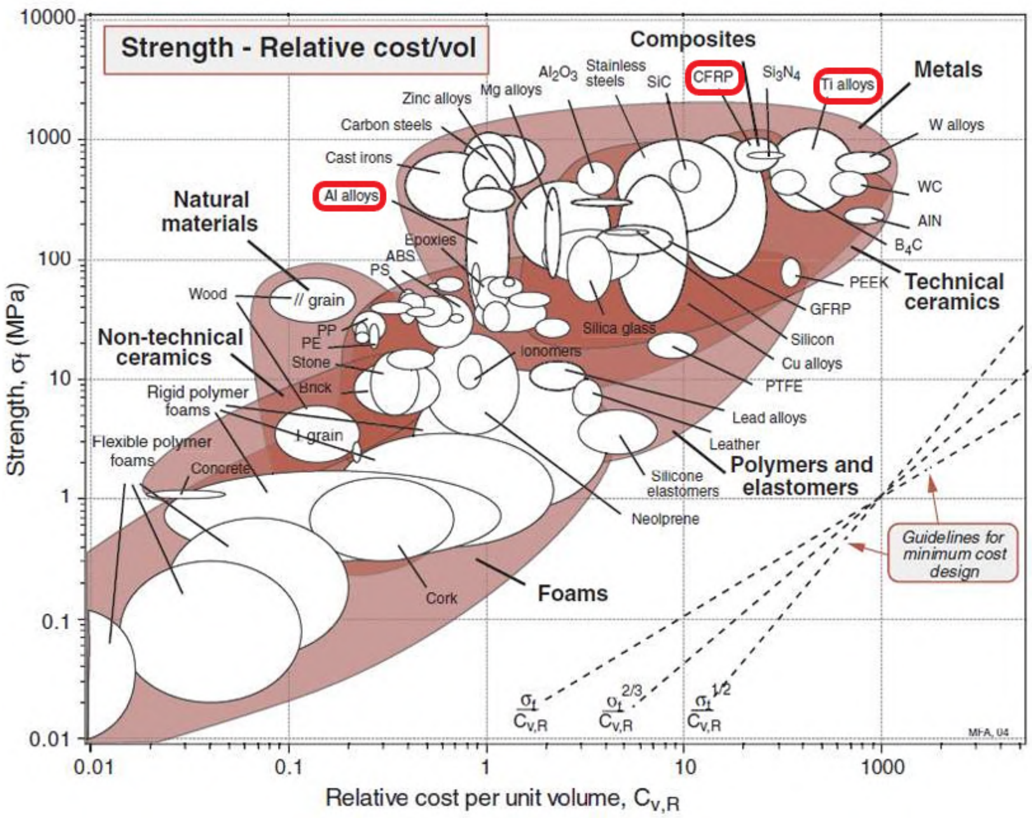

Figure 37: Strength vs Cost [40].

The high strength value of the material is related to the fact that it does not undergo reasonable deformation against the applied load. The evaluations here are similar to the part described in the Young's modulus - density graph. As shown in Figure 36, CFRP has a high strength/density value. Ti alloys have a density disadvantage and Al alloys have average properties.

Cost is another important criterion for material selection. The cost of the selected material should be low and other mechanical properties should be good. Young's modulus - density and strength - density graphs show that CFRP is the most advantageous material, but cost may cause these advantages to be ignored. As seen in Figure 37, CFRP and Ti alloys have higher strength values than Al alloys, but they have very high costs. Therefore, in this project, Al alloys, which have average properties in Young's modulus - density and strength - density graphs, will be preferred due to their low cost.

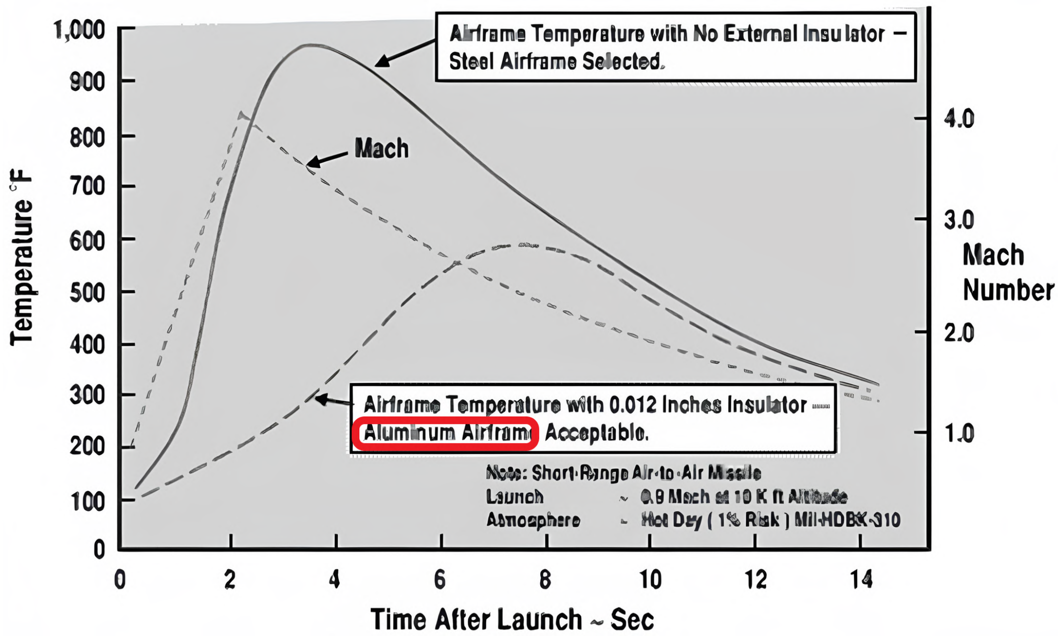

Figure 38: Temperature- Mach vs Time [41].

The Mach number for our cruise missile is set at 0.7. At about Mach 1, the aluminum fuselage temperature is 200-250 °F as seen in Figure 38.

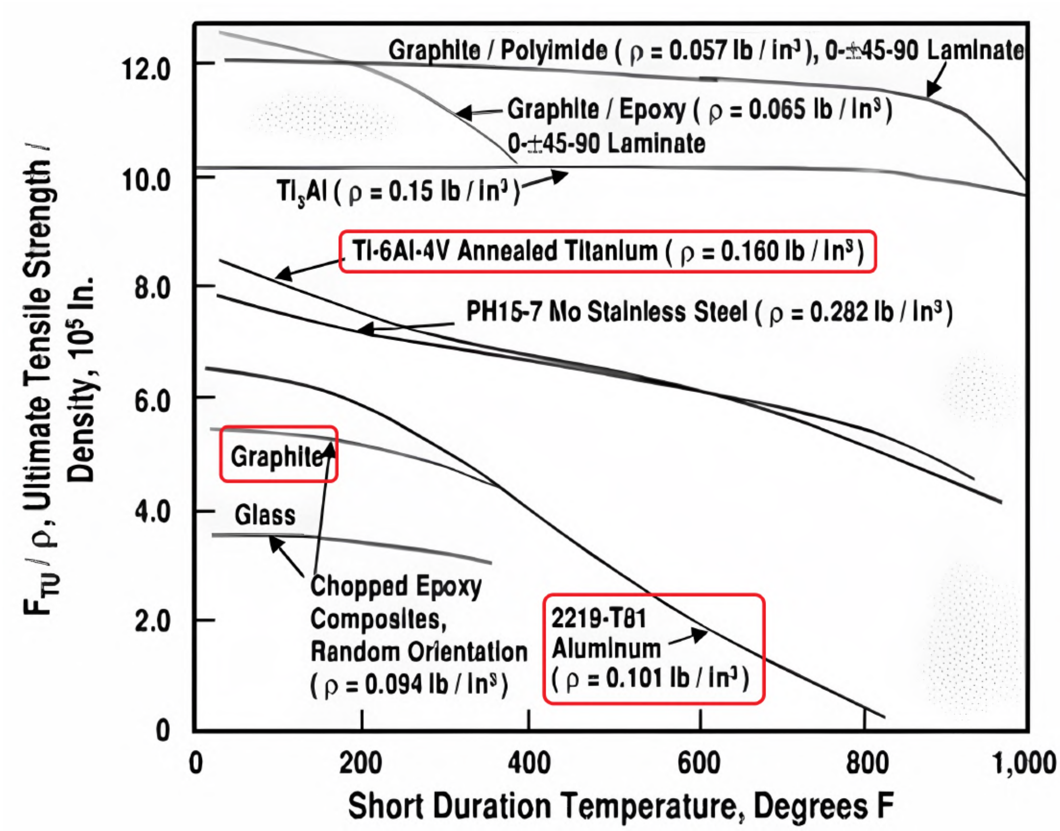

Figure 39: Ultimate Tensile Strength/Density vs Temperature [41].

In Figure 39 , graphite (CFRP) has the lowest ultimate tensile strength / density value in the range corresponding to 200 - 250 °F. The material with the best tensile strength value in this temperature band appears to be Ti alloys. The use of Al alloys, which have average values, seems to be a good option from a thermal point of view.

Aluminum alloys consist of 1000, 2000, 3000, 4000, 4000, 5000, 6000, 7000 and 8000 series. In the aerospace industry, the 2000, 6000, 7000 and 8000 series are suitable for structural component materials as they have better mechanical properties through heat treatment methods. Aluminum 2000 series are used in damaga-tolerant applications. Therefore, it is preferred for fuselage skins and control surfaces that have high fatigue resistance and damage-tolerant requirements. 6000 series have low fracture toughness and are preferred for ducting and tanks. 7000 series has the highest strength value compared to other alloys. Therefore it is suitable for stringers, frames, spars and frames. It is also the best alloy type in terms of machinability. This is an advantage for structural parts to be produced by CNC machining. The 8000 series has low density values but the cost is very high [38]. In line with this information, the most suitable materials for airframes are 2000 and 7000 series.

Wing and Fin Substructure Configuration

Generally, the wings consist of spar, rib and wing skin. However, due to the selected Sc0010 airfoil, the maximum wing tip thickness is 4.9 mm as seen in Figure 40a. Since the skins used in aviation are generally 2-4 mm thick, it was understood that the use of skin, rib and spar was not suitable for this cruise missile. There are two different production methods, casting and CNC machining, for the wings planned to be produced in monocoque form as seen in Figure 40b. As seen in Tables 22 and 23, since the mechanical properties of Al alloys suitable for the casting method are low, this method was not preferred. It is planned to be produced by CNC machining method. The end fin thickness is 5.6 mm. The fins, which have similar problems with the wings, are planned to be produced by CNC machining method.

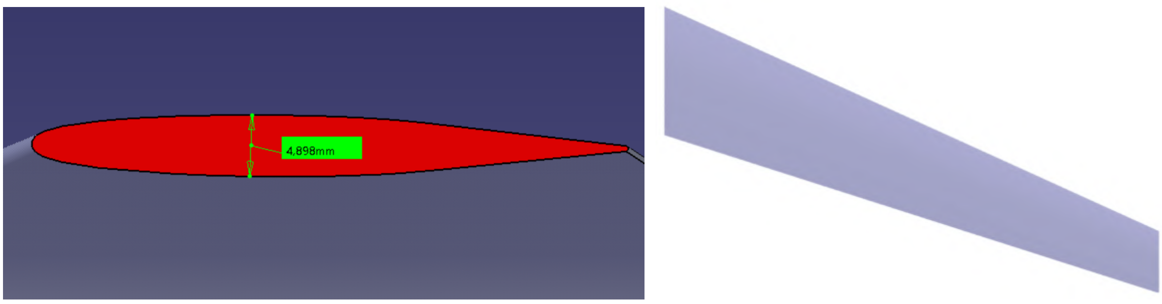

(a) Wing Tip (b) Monocoque Wing

Figure 40: Configuration of Wing.

Material	YS (MPa)	UTS (MPa)	Elongation (%)
Al-12Si-0.1Sc	143	254	8.3
Al-13Si-5Cu	284	343	0.68
Al-12.6Si-0.8Fe-3.6Mg-0.5La	270	312	4.28
Al-0.5Mg-0.7Si-0.13Fe-0.3Mn	294	328	14.9
Al-5Mg-0.6Sc	182	302	12.4

Table 22: Mechanical Properties of Some Cast Aluminum Alloys [42].

Material	YS (MPa)	UTS (MPa)	Elongation (%)
Al 2024	325	470	22
Al 6061	276	310	12
Al 7075	500	570	11
Al 8090	340	440	12

Table 23: Mechanical Properties of Non-cast Aluminum Alloys [38].

Since the production of wings and fins is planned with CNC machining method, the most widely used Al 7075 material in the literature was chosen as the wing and fin material.

Fuselage Substructure Configuration

The problems mentioned for wings and fins do not apply to the fuselage. This makes it preferable to use a semi-monocoque fuselage instead of a monocoque. With the semi-monocoque fuselage structure, the cruise missile is planned to be more easily assembled. The fuselage of cruise missile consists of skin, stringer, and frame as seen Figure 41. The fuselage is planned to be produced with the sheet metal forming method to obtain skins that are perfectly compatible with the aerodynamic surfaces. Since the frames are thick and complex geometry parts, it is planned to protect the structural integrity by producing them with the CNC machining method. The longitudinal elements of the body are stringers. In order for the stringers to be placed between the frames to take the desired shape, it was decided to use the sheet metal forming method.

Al 2024, the most widely used 2000 series aluminum from the aerospace industry, was chosen as the skin material. The material of the frames, which have the same production method as the wings and fins, was chosen as Al 7075 due to its machinability and widespread use. Stringers were selected as sheet metal since they should be easily formable. The material of the stringers, which are the structural elements that provide load transfer between the frames, is AL 7075, which has high mechanical properties.

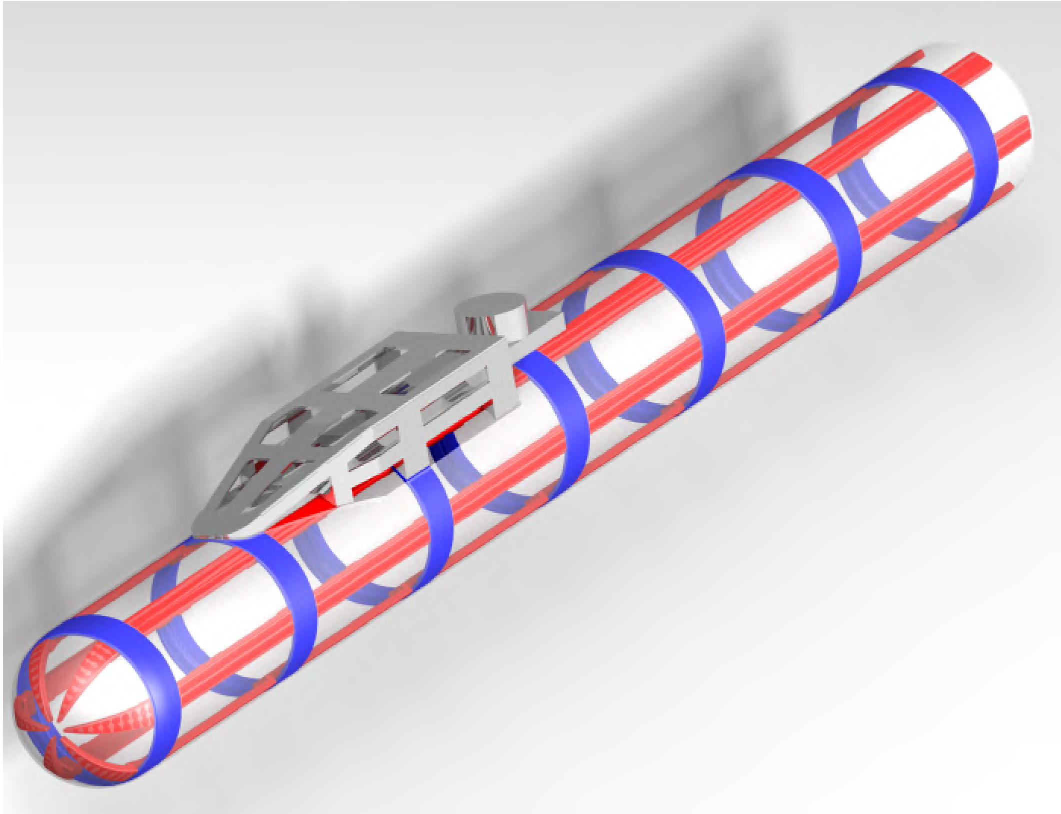

Figure 41: Fuselage Configuration.

Component	Material	Manufacturing Method
Wing	Al 7075	CNC Machining
Fin	Al 7075	CNC Machining
Frame	Al 7075	CNC Machining
Fuselage Skin	Al 2024	Sheet Metal Forming
Stringer	Al 7075	Sheet Metal Forming

Table 24: Materials and Manufacturing Methods of Structural Components.

The materials and production methods of structural parts are seen in Table 24.

Mechanisms

In this design, a foldable wing and fin mechanism was developed for the cruise missile to fit inside the internal weapon bays of aircraft. When the missile is stored or carried, the wings and fins stay in a closed position to save space, as shown in Figure 42. After the missile is launched, these parts open automatically to their full positions and allow the missile to fly properly, as shown in Figure 43. This folding system helps the missile fit inside narrow compartments and makes it easier to carry on modern aircraft.

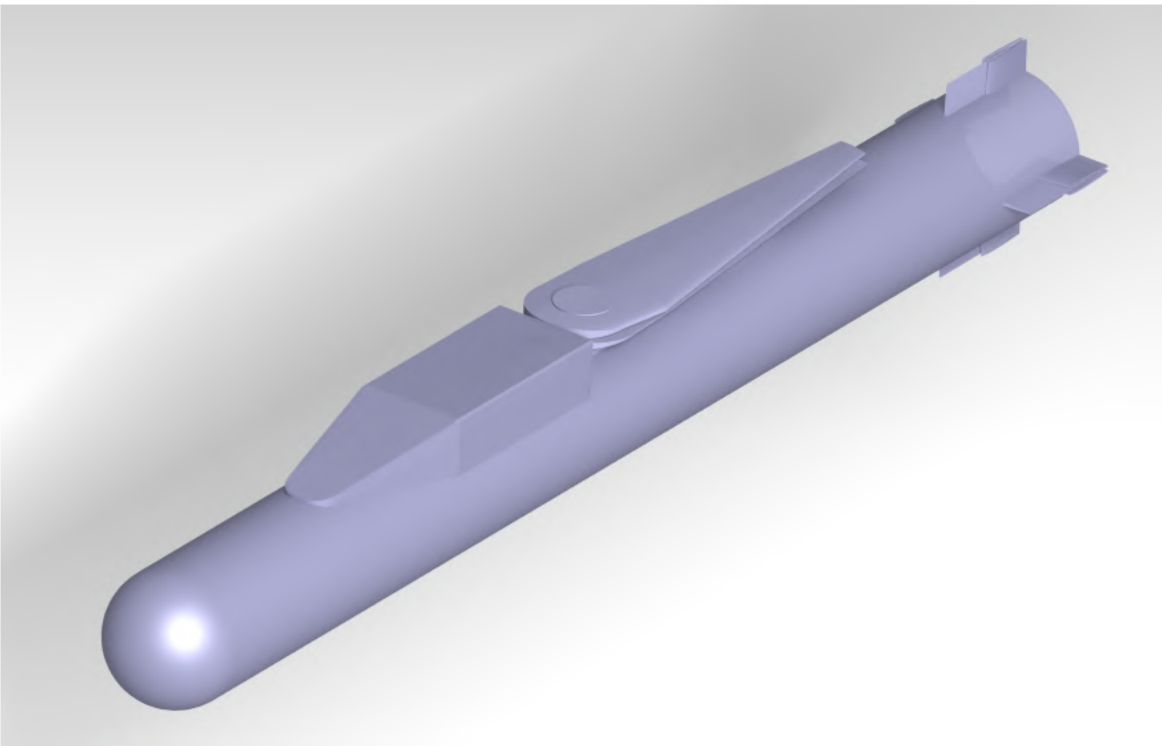

Figure 42: Closed Position of Wing and Fin.

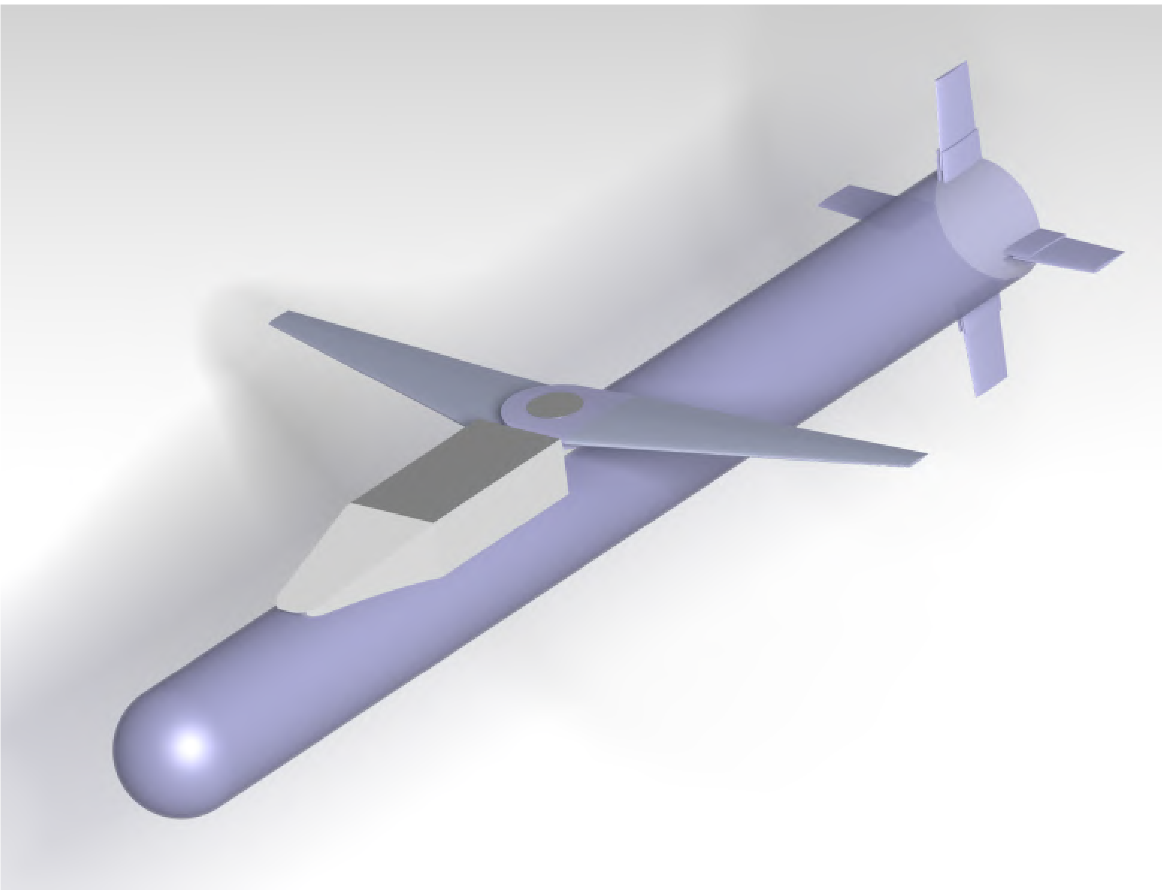

Figure 43: Opened Position of Wing and Fin.

The all structural design was modeled using CATIA V5 CAD software [43]. More CAD models added to Appendix 10.6.

4.5.2 Static Structural Analysis of Wing

The stresses and deformations resulting from applied operational loads on the geometry and material were examined in the static structural analysis phase [44].Firstly, boundary conditions and loads on the wing were determined.

Boundary Condition

The boundary condition is defined as a fixed support applied along the root of the wing.

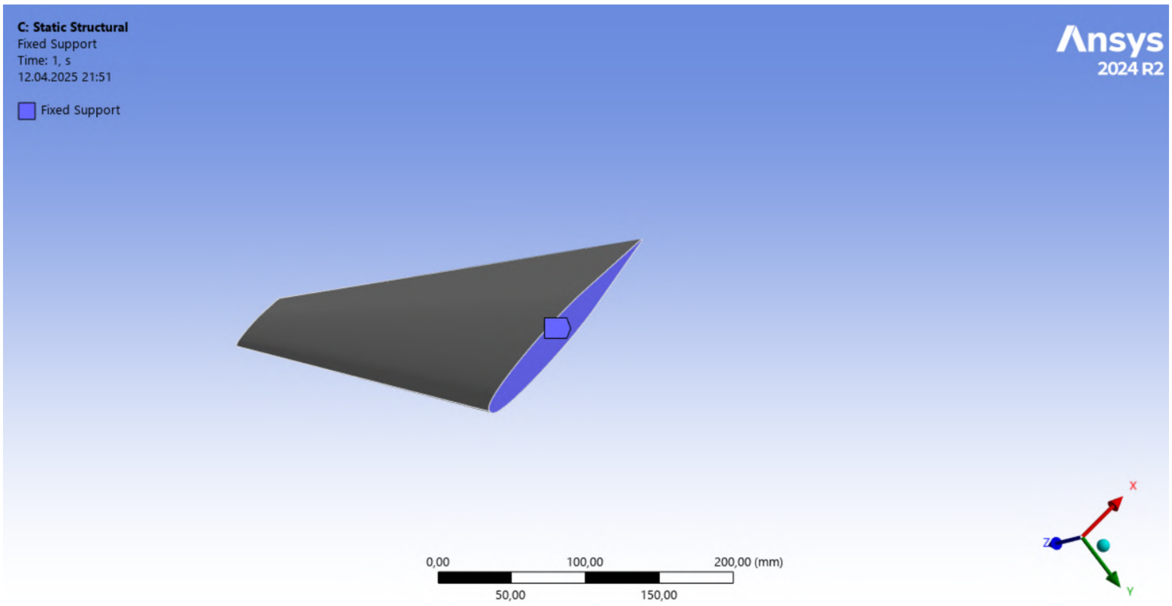

Figure 44: Boundary Condition

Loads

The aerodynamic loads on the wing are taken as a c_p distribution from the result of the CFD analysis.

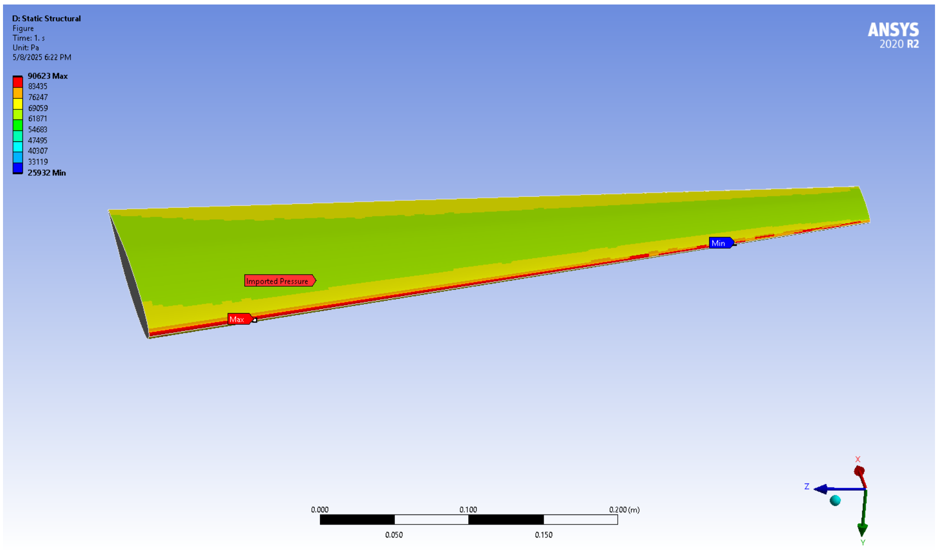

Figure 45: Loads on The Wing

Analysis Results

After defining the boundary conditions and applied loads, the stress and deformation distributions on the wing were analyzed through the finite element method (FEM). In this study, Al 7075 was chosen as the wing material primarily due to its low density, cost-effectiveness, and acceptable strength characteristics, which make it an ideal candidate for lightweight structural components in aerospace applications.

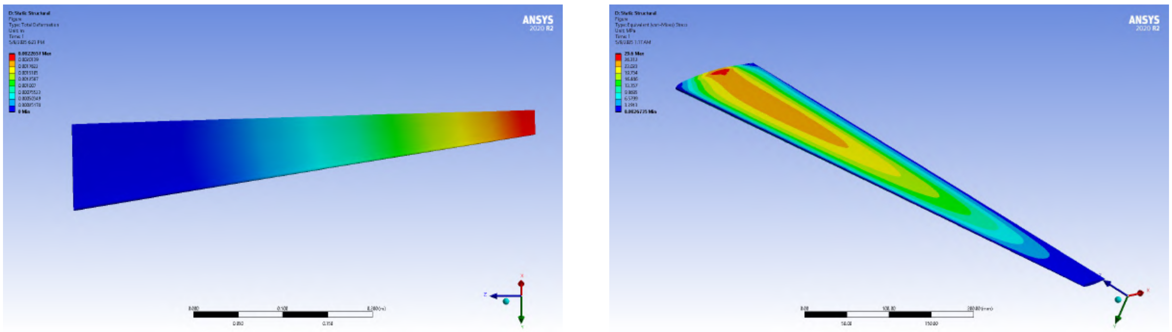

(a) Total Deformation (b) Von Mises Stress

Figure 46: Total Deformation and Von Mises Stress

The stress and deformation results obtained from the finite element analysis are presented in Figure. 57 and results are given in Table. 25. As anticipated, the maximum deformation is observed at the wing tip region, where the structure is free, while the highest stress concentrations occur at the wing root region due to the fixed boundary conditions applied. This distribution is fully consistent with typical cantilever beam behavior subjected to aerodynamic loads.

It is evident from the results that both stress and deformation values remain significantly below the critical limits of the selected material. For Al 7075, the yield strength is approximately 500 MPa. In contrast, the maximum stress value obtained from the analysis is around 29.6 MPa. This considerable margin between the yield strength and the calculated stress indicates that the chosen material provides an adequate safety factor for the given loading conditions. Therefore, it can be concluded that Al 7075 is a suitable and reliable material choice for the wing structure within the specified design and operational requirements.

Result Type	**Minimum**	**Maximum**	**Average**
Total Deformation [mm]	0.0000	2.2829	0.7762
Von Mises Stress [MPa]	2.6735×10^{-3}	29.6	7.883

Table 25: Summary of total deformation and Von Mises stress results obtained from structural analysis.

The presented values are the outcomes of the static structural analyses, specifically focusing on the stress and deformation behavior of the wing structure under the applied loading conditions.

Mesh Convergence

In order to reduce the computational cost, mesh convergence was applied for blade analysis. As can be seen from Table 26, the result converged at 29.6 MPa. For this analysis, instead of using 11,484 elements, the same result was obtained by using 5,145 elements.

Element size (mm)	**Number of elements**	**Von-Mises stress (MPa)**
10	1272	28.09
8	1848	29.31
7	2356	29.58
5	5145	29.60
4	11484	29.60

Table 26: Effect of mesh refinement on Von-Mises stress values.

Hand Calculation Validation

We modeled the wing of the cruise missile as a beam and its dimensions are: length=600mm, thickness=110mm and height=17mm. We also modeled the lift and drag forces on the wing as shown below.

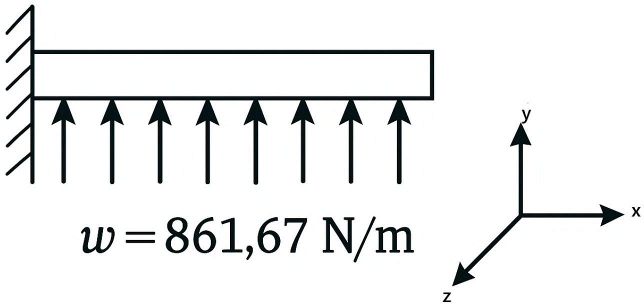

Figure 47: Lift distribution on wing

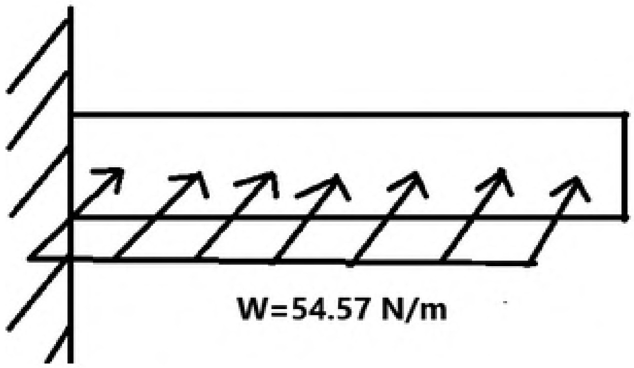

Figure 48: Drag distribution on wing

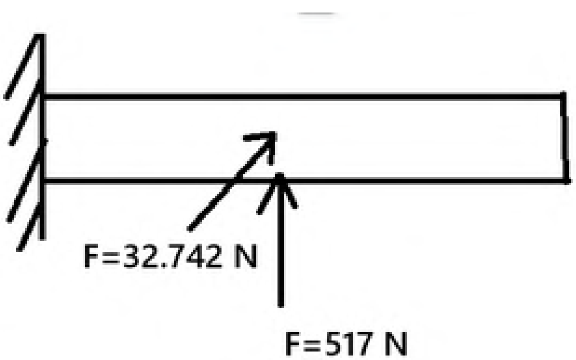

Figure 49: Resultant force

The stress distribution of lift and drag force at the root of the beam is given below.

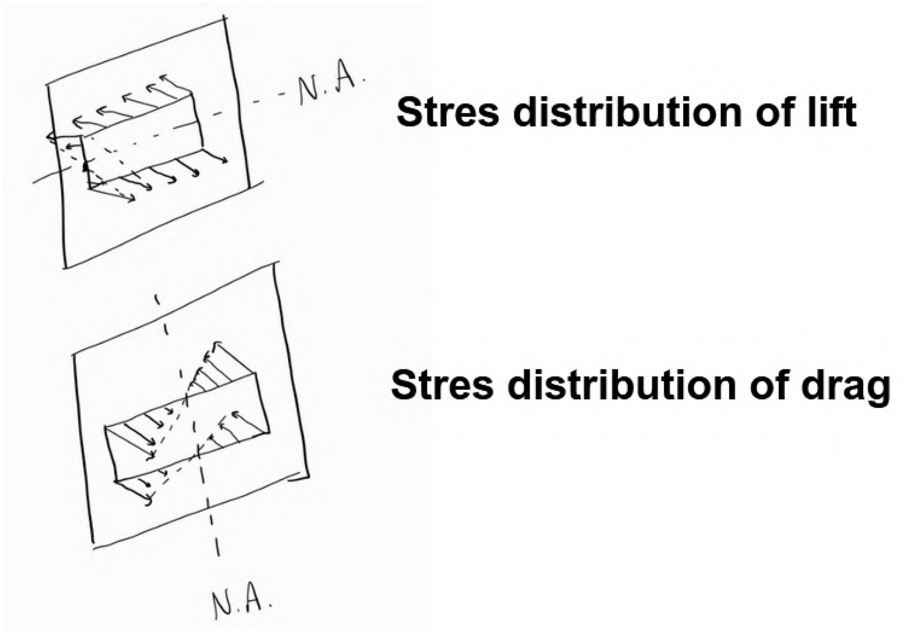

Figure 50: Stress distribution

If we take a unit stress element from the center of the beam, we can find the maximum Von Mises stress and ignore the stress caused by drag.

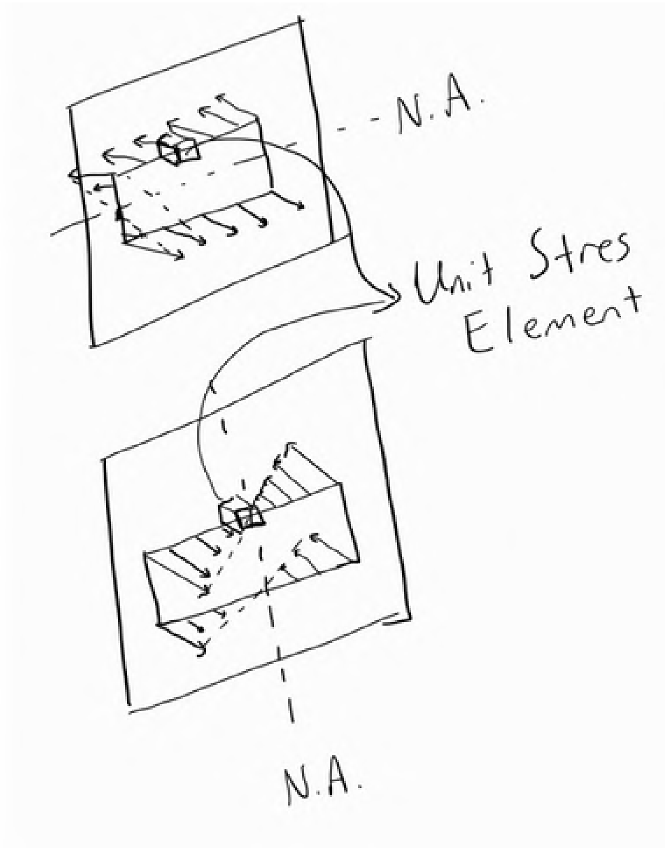

Figure 51: Unit stress element

The transverse shear stress should be added to the von mises calculation, and the shear stress diagram and moment diagram are given below to find the shear stress.

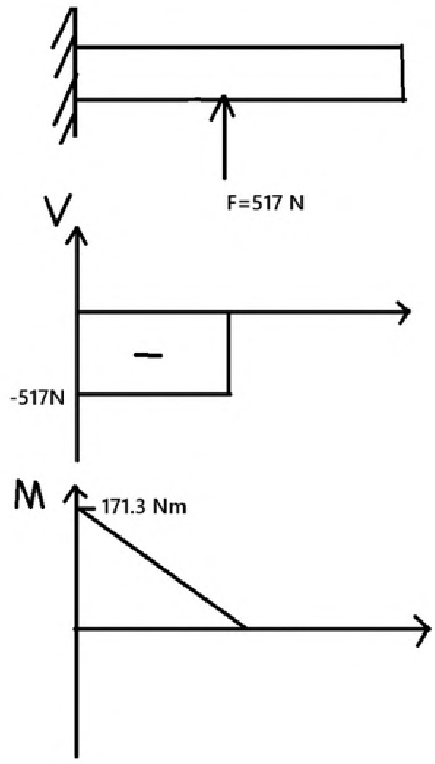

Figure 52: Shear and Moment diagram

$$\tau = \frac{VQ}{It} \tag{21}$$

For beam transverse shear stress can be considered like below

$$\tau = \frac{3}{2}\frac{V}{A} \tag{22}$$

$$\tau = \frac{3 * 517}{2 * 110 * 17 * 10^{-6}} = 0.415MPa \tag{23}$$

Bending stress is as follows

$$\sigma = \frac{Mc}{I} \tag{24}$$

The bending stress created by the lift is as follows.

$$\sigma = \frac{Mc}{I} = \frac{571 * 0.3 * 8.5 * 10^{-3}}{\frac{1}{12} * 110 * 17^3 * 10^{-12}} = 32.3MPa \tag{25}$$

The bending stress generated by the drag was ignored by selecting the unit element in the middle. In addition, the transverse shear stress caused by the drag was ignored because it is very small. Bending stress and transverse shear stress generated by the lift we consider. The representation of these stresses in unit stress element is as follows.

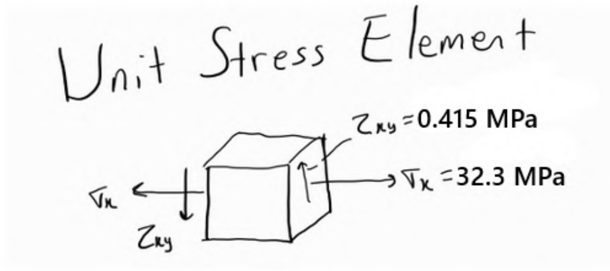

Figure 53: Unit Stress Element with Stresses

Calculating Von mises stress

$$\sigma_{von-misses} = \frac{1}{\sqrt{2}}[(\sigma_x - \sigma_y)^2 + (\sigma_y - \sigma_z)^2 + (\sigma_z - \sigma_x)^2 + 6(\tau_{xy}^2 + \tau_{yz}^2 + \tau_{xz}^2)]^{1/2} \quad (26)$$

$$\sigma_{von-misses} = \frac{1}{\sqrt{2}}[(32.3-0)^2+(0-0)^2+(0-32.3)^2+6(0.415^2+0^2+0^2)]^{1/2} = 32.308MPa \quad (27)$$

For an easier calculation, we can apply Tresca if we accept the shear stress as 0.

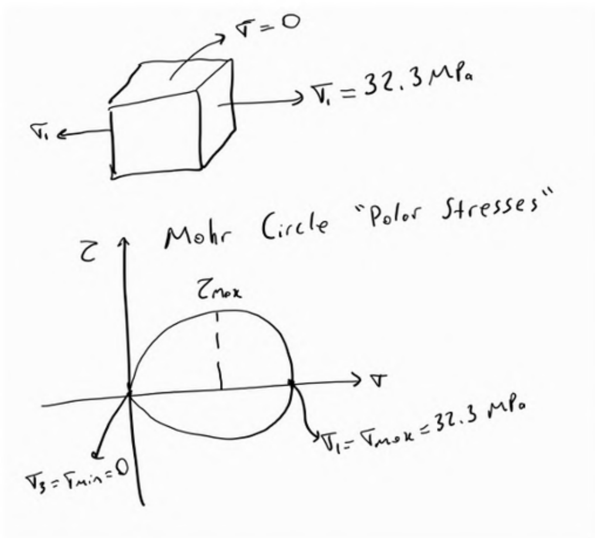

Figure 54: Unit stress element and Mohr circle for Tresca

$$\sigma_{tresca} = |\sigma_{max} - \sigma_{min}| \quad (28)$$

$$\sigma_{tresca} = |32.3 - 0| = 32.3MPa \quad (29)$$

When we solve the beam in ANSYS under the same conditions, the result obtained is as follows.

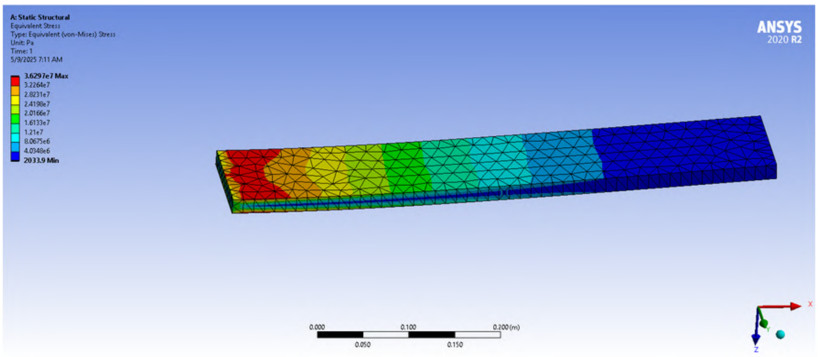

Figure 55: ANSYS result

4.5.3 Static Structural Analysis of Frame

The main purpose of the frame analysis was to examine the stress values on the frame caused by the aerodynamic loads on the wing. Stresses resulting from the selection of two different boundary conditions were analyzed. Images of the frame location are given in Appendix 10.5.

Boundary Conditions

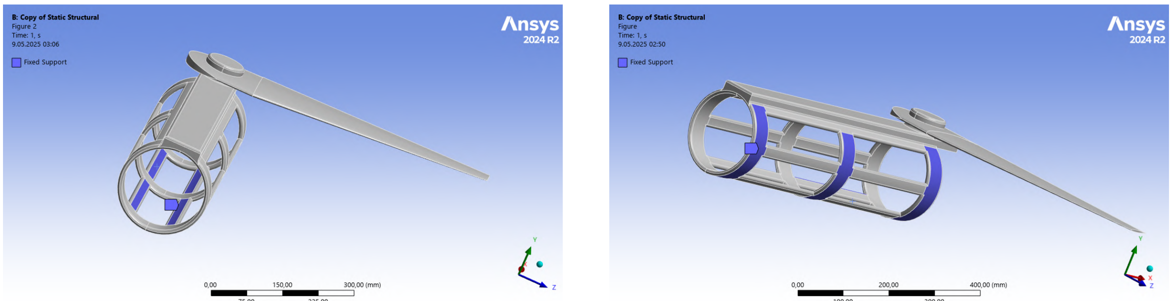

(a) Stringer Fix

(b) Ring Frame Fix

Figure 56: Boundary Conditions

While the boundary conditions were selected, the areas where the structure would be fixed to the missile were fixed, and stress examinations were carried out.

Loads

Aerodynamic loads were distributed over the entire surface. Lift force was applied as 517 N in the +y direction, and drag force was applied as 32 N in the +x direction. The loads on the wing are the loads resulting from the CFD analyses.

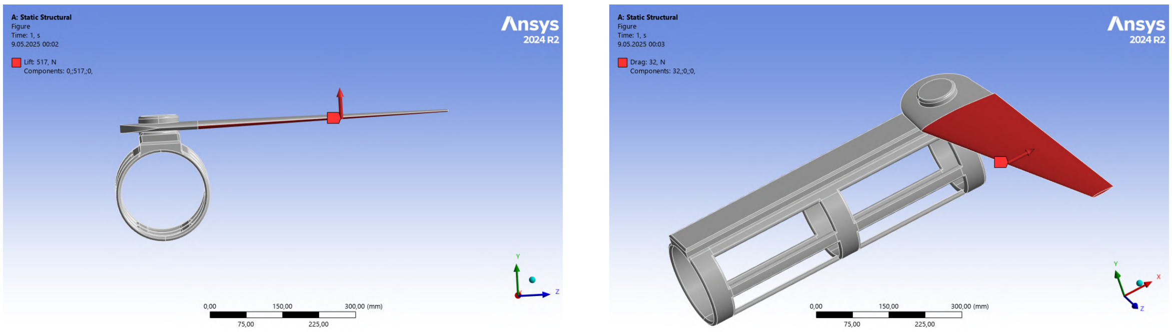

(a) Lift(517N)

(b) Drag(32N)

Figure 57: Loads

Analysis Result

The von Mises stress values resulting from the analysis are shown in Table 27 and Figure 58.

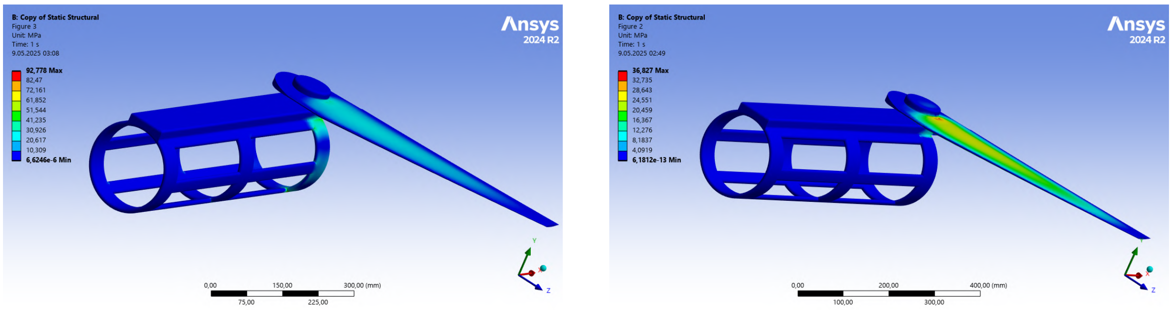

(a) Stringer Fix

(b) Ring Frame Fix

Figure 58: Von Misses Stresses

Boundary Condition	**Minimum [MPa]**	**Maximum [MPa]**	**Average [MPa]**
Ring Frame Fix	6.1812e-013	36.827	1.9843
Stringer Fix	6.6246e-006	92.778	3.2215

Table 27: Stress values for different boundary conditions.

The most stress occurred at the junction of the ring frame and the stringer in the analysis results.

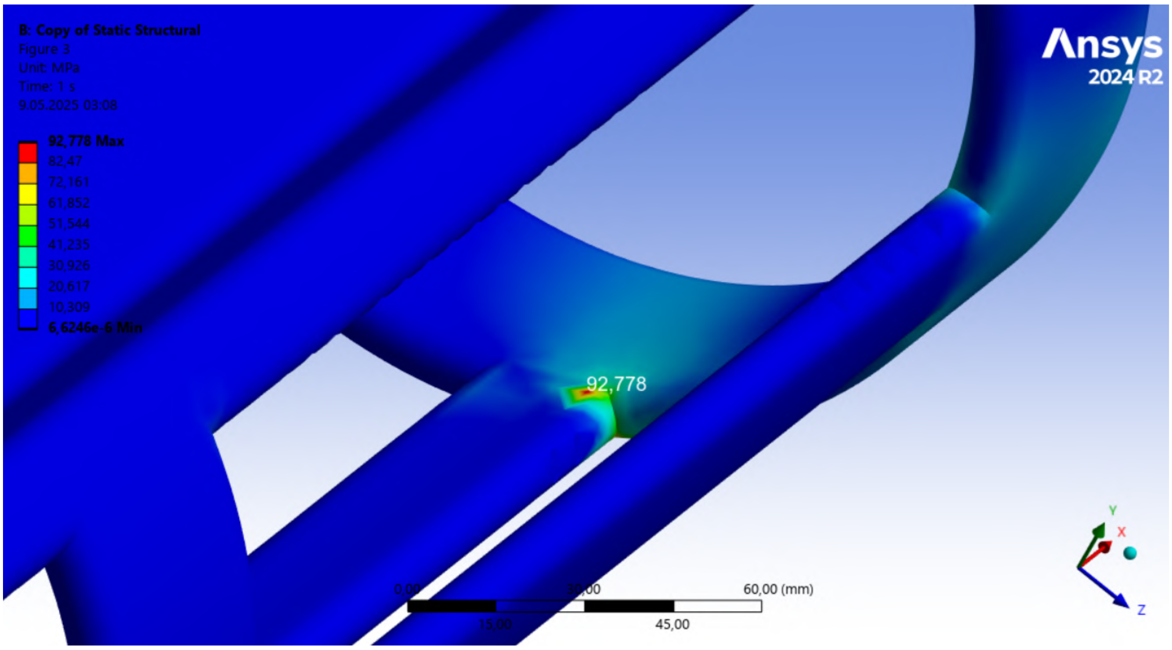

Figure 59: Von Mises Stress

Al 7075 was chosen as the material. Although the stress is far below the yield strength of the material, these areas are the areas that need the most attention.

4.5.4 Modal Analysis

In this study, modal analysis was performed on a cruise missile structure to investigate its free vibration behavior. The main objective of the study is to determine the natural frequencies and mode shapes of the missile.

Geometry

Missile Length: 2000 mm
Missile Diameter: 200 mm
Wall Thickness: 3 mm

Material Properties

Material	Density [kg/m^3]	Young's modulus [GPa]	Poisson's ratio
AL-7075	2710	71	0.33

Table 28: Material properties.

Mesh Details

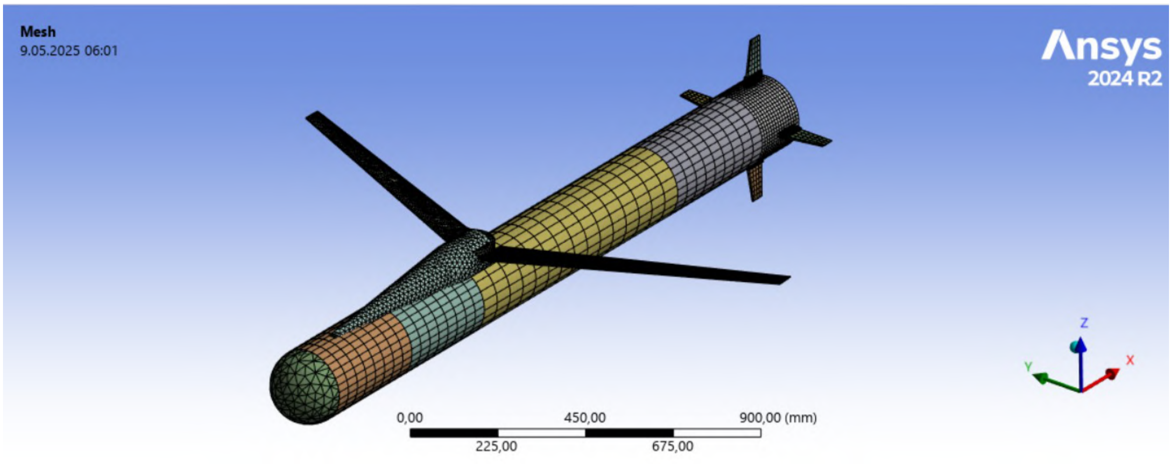

Figure 60: Mesh of cruise missile

System's Component

Cruise missile's component represented by point mass in ANSYS.

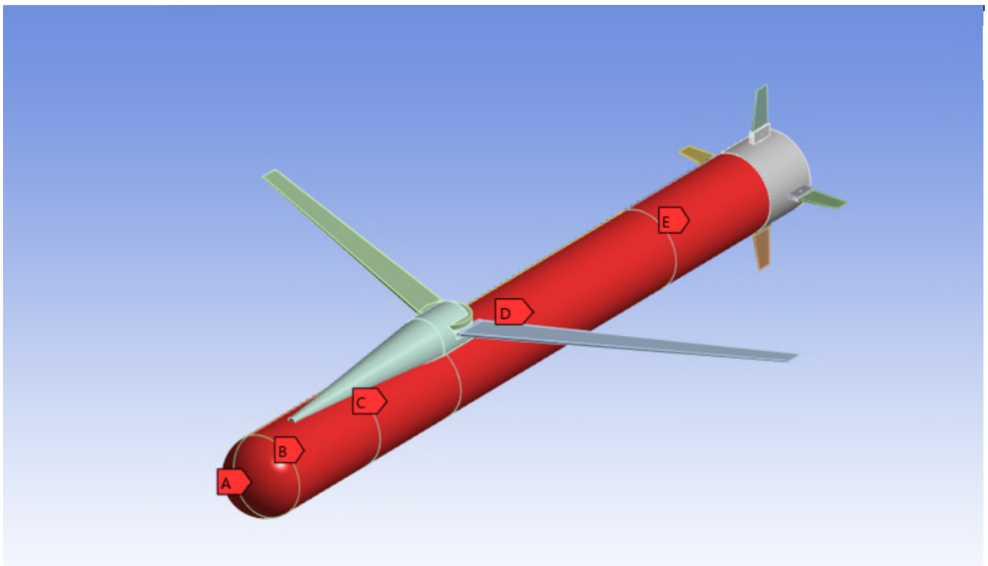

Figure 61: Component represented by point mass

Boundary Conditions

In this study, a free-free modal analysis was performed. Since the aim was to determine the natural frequencies under free vibration conditions, no fixed supports were applied to the model.

Results

The first 6 modes were observed as rigid body modes in which the system moves freely. So the first 6 modes are equal to 0 and the other 6 modes are given in the Table 29.

Table 29: Results of Modal Analysis

Mode	**Frequency [Hz]**
1	0
2	0
3	0
4	1.0051e-3
5	1.1803e-3
6	2.8185e-3
7	10.467
8	13.39
9	44.741
10	45.431
11	108.81
12	110.87

Selected engine is JetCat P550 Pro and its rpm range is 26000-83000.

$$2600rpm = \frac{2600}{60} = 433.3Hz \tag{30}$$

$$83000rpm = \frac{83000}{60} = 1383.3Hz \tag{31}$$

Based on the modal analysis results and the frequency range in which the motor operates, there will be no resonance due to the motor.

Mode Shape

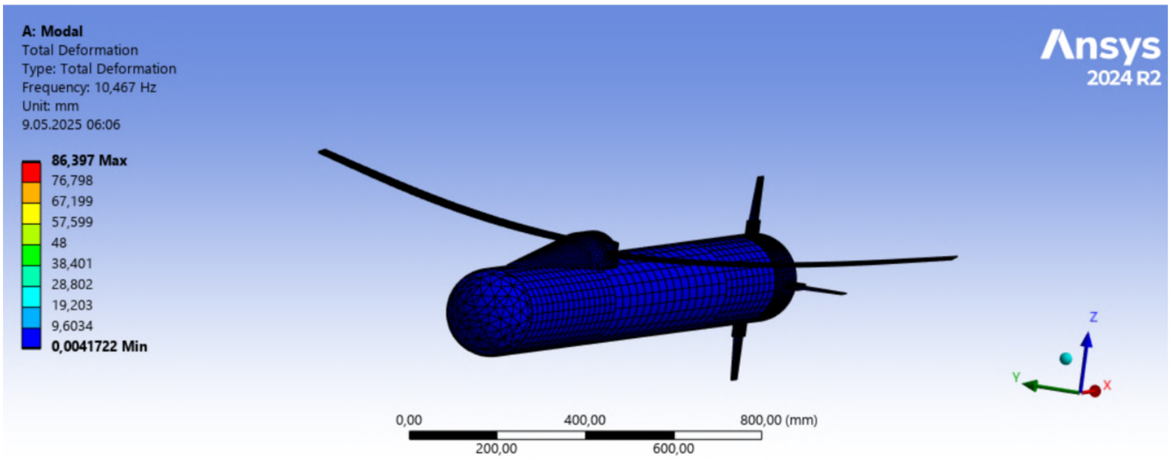

Figure 62: Mode Shape 1

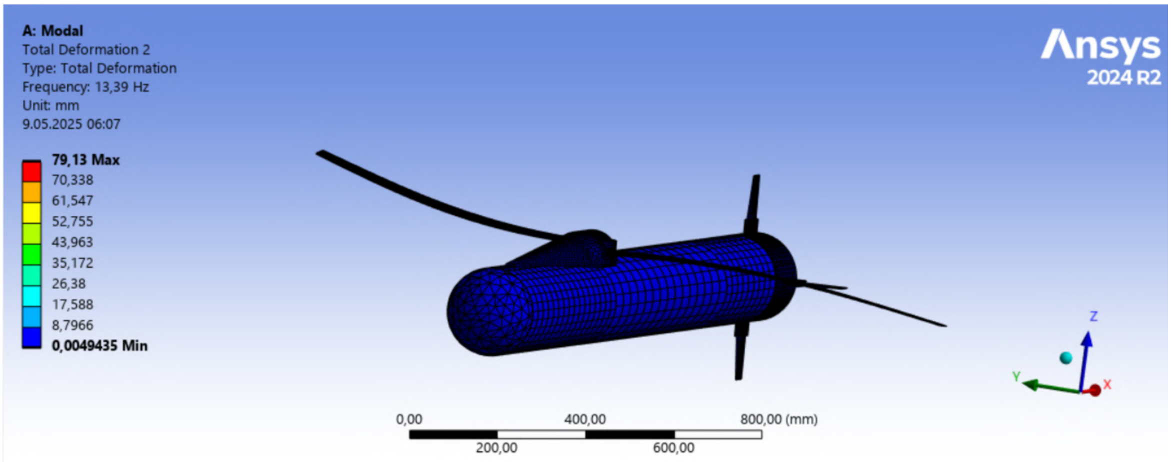

Figure 63: Mode Shape 2

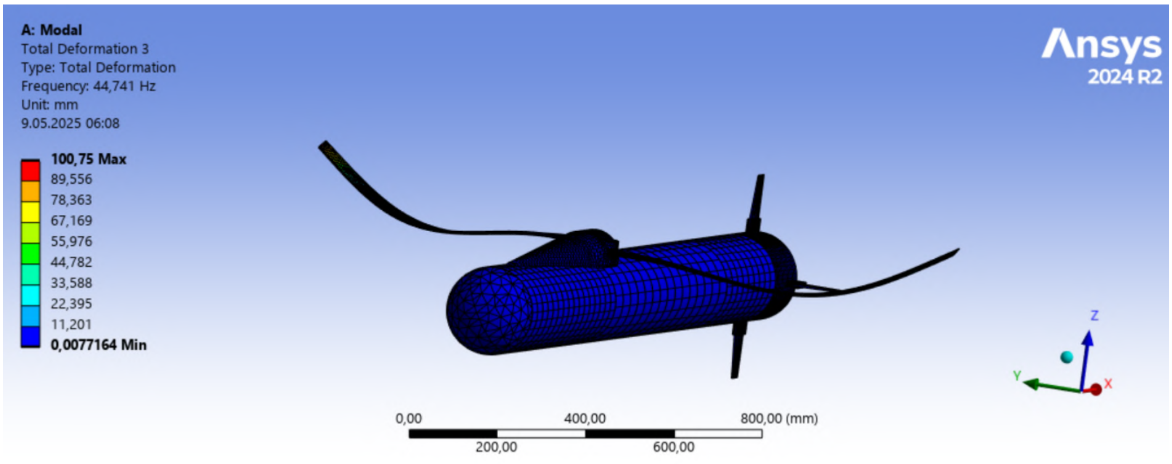

Figure 64: Mode Shape 3

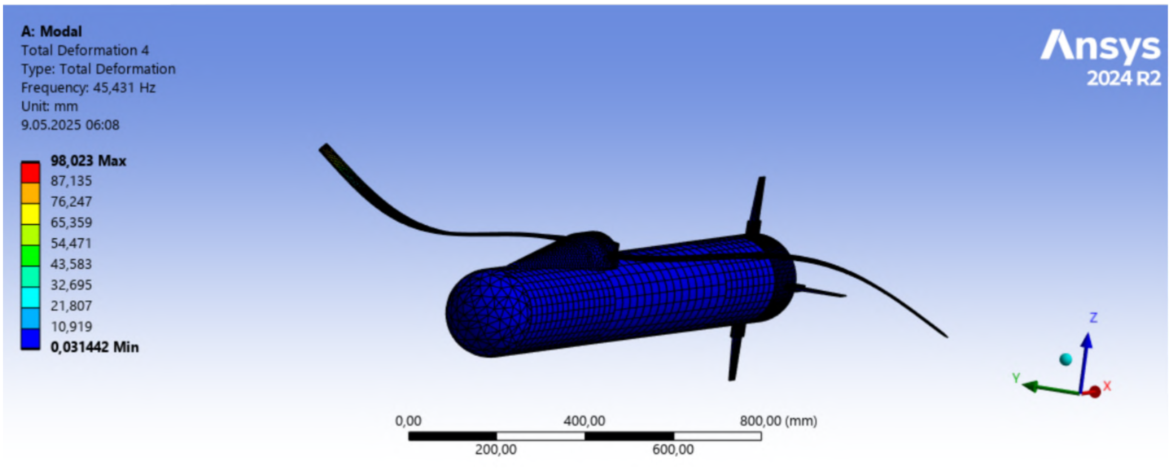

Figure 65: Mode Shape 4

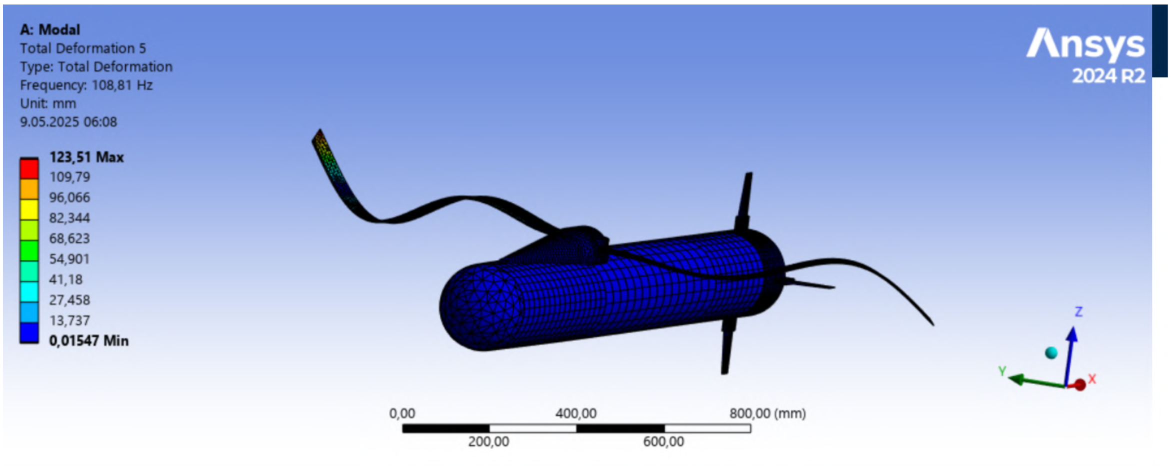

Figure 66: Mode Shape 5

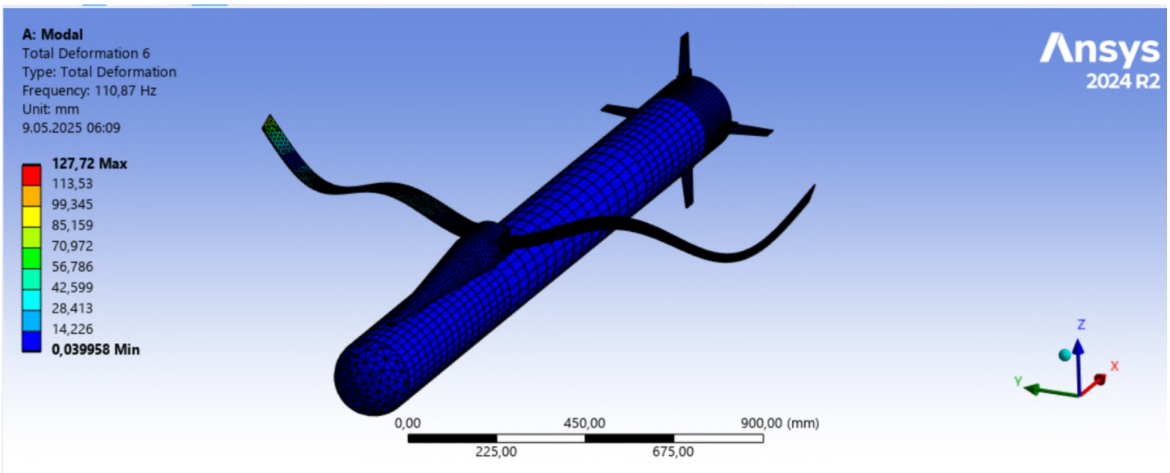

Figure 67: Mode Shape 6

Hand Calculation Validation

Modal analysis was performed for the wing and tail. Modal analysis was also performed by modeling the wing and tail as a beam. The following table shows the ANSYS results of the wing and tail, ANSYS results of the wing and tail modeled as beam, and hand calculations of the wing and tail modeled as beam.

Table 30: Modal Analysis of Beam and Wing

	Cantilever Beam	Cantilever Beam Ansys	Actual
Wing	9.975	10.243	10.714
Fin	244.4	256.33	316.4

The following simple formula sequence was followed for hand calculation for modal analysis.

$$k_{eq} = \frac{EI}{l^3} \tag{32}$$

$$\rho = \frac{m}{V} \tag{33}$$

$$m_{eq} = m/4 \tag{34}$$

$$w = \sqrt{\frac{k_{eq}}{m_{eq}}} \tag{35}$$

$$f_n = \frac{w}{2\pi} \tag{36}$$

4.6 Systems Integration

During the system integration process, data from missile systems available in the literature were utilized. In line with the literature, several assumptions were made regarding component weights are given in Table 31. Nose tip distance values are the distance between the center of gravity of each component and the nose tip of the cruise missile.The final configuration resulting from this integration is presented Figure 68.

Number	Component	Distance from nose tip (mm)
1	Imaging Infrared (IIR)	28
2	Guidance System (IMU)	90
3	Processor (NVIDIA Jetson Nano)	157
4	GPS	203
5	Navigation (Ardupilot Cube)	249
6	Fuze	317
7	Warhead	475
8	Fuel Tank + Fuel (kerosene)	927
9	Battery	1314
10	Intake	1436
11	Propulsion System	1784.5
12	Control Actuators	1882.71

Table 31: Location Information of Missile Components.

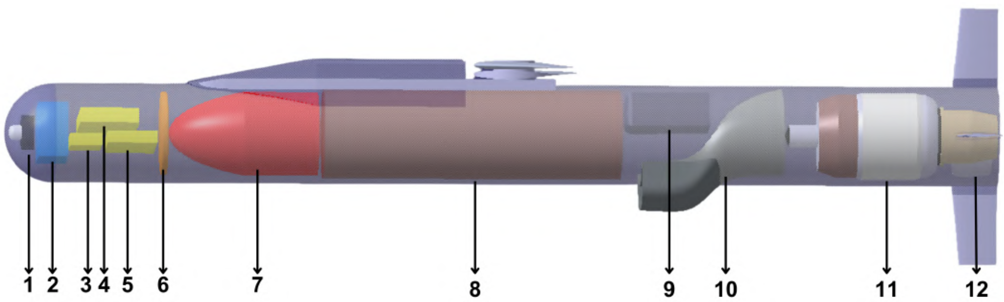

Figure 68: System Integration.

The system integration is considered in this manner. In the proposed integration, the mass values were calculated approximately. X_{CG} is calculated in section 4.4.3 by including wing, fin and fuselage structure in these components.

5 Safety and Reliability

In this section, we examine the measures taken to ensure that the cruise missile performs its mission with high confidence while minimizing the probability and consequences of system failures. This includes systematic risk identification, mitigation strategies, and failure analysis to enhance mission assurance.

5.1 Risk Analysis and Mitigation Strategies

Purpose: This subsection identifies potential hazards in the missile's design and operation and outlines proactive strategies implemented to minimize these risks. It ensures that all safety critical functions are accounted for during design and integration.

In the design and operational planning of our air-to-surface cruise missile, a thorough risk analysis has been conducted to ensure both mission success and system reliability. Given the missile's complex integration of propulsion, navigation, and payload subsystems, we identified several potential failure scenarios and implemented mitigation strategies tailored to the climb-and-dive mission profile and naval target engagement.

Potential Failure Scenarios

- **Loss of Guidance or Navigation:** Due to the sea-skimming and climb-dive profile, any failure in the hybrid GPS/INS system or terminal seeker can lead to a missed target or collateral damage.
- **Engine Failure:** The turbojet (JetCat P550 PRO) operates at high RPM (up to 83,000) and temperature (up to 750°C), posing risk of thermal stress, bearing failure, or fuel pump malfunction.
- **Structural Failure:** The missile undergoes aerodynamic stress during climb and high-G dive. Improper material selection or flawed structural design could lead to catastrophic in-flight breakup.
- **Warhead Malfunction:** A failure in detonation timing or triggering mechanism (especially in XF-10 thermobaric warhead) may result in ineffective damage or unintended consequences.
- **Data Link or Communication Failure:** During certain phases, loss of uplink or failure in internal telemetry can hinder diagnostics or mission updates.

Mitigation Strategies

Purpose: This section presents specific design choices and redundancies incorporated to reduce the likelihood of failure and improve the resilience of the system under adverse conditions.

- **Redundant Navigation:** A dual-redundant GPS-INS navigation system with internal error correction and data fusion ensures resilience against signal loss or GPS jamming.
- **Engine Monitoring and Thermal Protection:** The integration of real time ECU monitoring, EGT probes, and thermal shielding reduces the risk of engine related failures. The P550's self regulating ECU contributes to this resilience.
- **Fail Safe Detonation Mechanism:** The XF-10 warhead includes a multi channel trigger system arming based on impact sensors, proximity radar, or time delay backup to ensure high reliability.
- **Robust Structural Design:** Aerospace-grade aluminum alloys and composite reinforcements were selected to withstand load during the dive phase. FEM based simulations validated structural integrity.
- **Environmental Sealing:** To counteract sea spray, humidity, and thermal variations, the missile's outer shell includes a water-resistant coating and sealed avionics bay.
- **Terminal Evasive Capability:** The missile is programmed to execute high agility maneuvers in the terminal phase to bypass countermeasures, increasing survivability.

5.2 Failure Modes and Effects Analysis (FMEA)

Purpose: FMEA is a systematic technique used to identify all possible failure modes of individual components, assess their consequences, and prioritize mitigation based on severity, likelihood, and detectability. This is essential for identifying weak points before production or deployment.

The table below outlines the primary components of the cruise missile, possible failure modes, their effects, severity, and mitigation strategies. Each failure mode was evaluated using standard FMEA methodology, considering Severity (S), Occurrence (O), and Detection (D), with a qualitative Risk Priority Number ($RPN = S \times O \times D$) assessment.

Subsystem	Potential Failure Mode	Effect on System	S	O	D	Mitigation Strategy
Guidance (INS/GPS)	Signal loss / drift	Missed target / crash	9	4	3	Dual GPS-INS, drift correction, terminal seeker fusion
Turbojet Engine (P550)	Overheating / RPM loss	Loss of thrust, crash	10	3	4	ECU-controlled limits, real-time monitoring, thermal insulation
Flight Control Surfaces	Servo failure	Loss of control / instability	8	4	5	Redundant actuator paths, health diagnostics, flutter testing
Warhead (XF-10)	Failed detonation	Ineffective strike	9	2	3	Multiple arming mechanisms, sensor validation, self-check routines
Data Bus / Avionics	Bus failure / noise	Sensor data loss / GNC error	8	3	4	Shielded wiring, signal redundancy, CRC error checking
Power Supply	Battery failure	Loss of all functions	10	2	3	Multi-cell LiPo packs with thermal fuses, voltage regulation
Airframe Structure	Material fracture	In-flight breakup	10	2	3	FEM analysis, load testing, factor-of-safety margin
Seeker System	Terminal sensor failure	Reduced hit accuracy	7	3	4	Dual-mode seeker (IR/radar), fallback targeting logic

Table 32: FMEA for Major Missile Subsystems

5.3 System Reliability Predictions

Purpose: This subsection aims to provide a theoretical estimate of the cruise missile system's overall reliability. Due to the missile being in the conceptual phase, real world test data or full scale simulations are not yet available. Therefore, comparative analysis is made based on two similar operational systems.

Reliability Estimation Approach:

- **Failure Mode Analysis (FMEA):** Already conducted in Section 1.2.
- **Historical Reliability Metrics:** Using Mean Time Between Failure (MTBF) and mission success rates from similar missiles.
- **Assumptions:** Mission duration is short enough that wear out failures are negligible compared to catastrophic failures. Reliability is thus modeled primarily via subsystem MTBF and known rates of success.

Reference Systems:
Two comparable cruise missiles are selected: the SOM-J, developed by TÜBİTAK-SAGE, and the Naval Strike Missile (NSM) by Kongsberg. These missiles match our system in mission profile, propulsion class, and navigational complexity.

Applicability to Our Missile:
Although our system uses a smaller warhead and lighter airframe, the architecture and redundancyprinciples are similar. It is therefore acceptable to infer a conservative estimated success rate based on these analog systems.

Table 33: Similar System Comparison

System	**Mission Profile**	**Navigation System**	**Success Rate**	**MTBF (h)**
Naval Strike Missile (NSM)	Sea-skimming + evasive	GPS/INS + Passive IR	94–96%	150–180
SOM-J	Climb-Dive / Sea-skimming	GPS/INS + IR seeker	93–95%	130–160
Our System (Estimated)	Climb-Dive	GPS/INS + IIR + fallback logic	90–92%	120–150

	Loss of control during flight	Communication failure	Delay in motor ignition	Control surface malfunction	Software error	Overheating in motor section	Structural failure during flight
Probability	1	2	2	3	3	1	1
Impact	5	4	2	4	3	3	3
Score	5	8	4	12	9	3	3
Risk Level	Moderate	High	Low	High	High	Low	Low

Figure 69: Missile System Risk Assessment Table

6 Verification and Validation

6.1 Test Plans for Subsystems and Full System

The verification and validation process of our missile system is structured around the independent testing of each subsystem followed by integrated full-system evaluations. Our team is divided into four core subsystems (aerodynamics, propulsion, control, and structures)each of which is responsible for conducting detailed simulations and analyses to ensure their respective components meet performance expectations

6.1.1 Subsystem test plans

Aerodynamics (CFD)

Objectives and Procedures:

- The comparison of different airfoils is planned in order to select the most suitable airfoil for generating sufficient lift.
- Wings that can provide the required lift will be designed and analyzed.
- A full-body model will be created, and the aerodynamic behavior of the entire system will be analyzed.

Software and Methods:

- All simulations will be performed using ANSYS Fluent 2020 R2 [5].
- ICEM CFD 2020 R2 [45] and Pointwise will be used for mesh generation.
- AGARD Model B simulations will be conducted to validate the turbulence model.

Structure

Objectives and Procedures:

- Static structural analyses will be performed on both the wing and the fuselage.
- Modal analysis will be conducted for the wing and fin to determine the system's natural frequencies.
- The goal is to evaluate stress, deformation, and strain values under expected aerodynamic loads.
- In later stages, a hinge mechanism will be added to the wing's attachment point, and the resulting bending and torsional loads will be examined.

- Critical stress regions in the fuselage will be identified, and reinforcement strategies will be developed accordingly.

Software and Methods:

- Static structural analyses will use aerodynamic loads obtained from CFD results as input.
- Finite element analysis (FEA) tools will be employed to assess structural performance under realistic flight conditions.
- Modal analysis techniques will help ensure the system avoids resonance and maintains dynamic stability.
- All structural analyses were performed using ANSYS 2020 R2 [46].
- CATIA V5 [43] was used in the design phase.

Control

Objectives and Procedures:

- A full 6-DOF (Degrees of Freedom) mathematical model of the system has been developed based on reference equations of motion.
- The model includes aerodynamics, propulsion, and atmospheric dynamics.
- Aerodynamic data will be obtained from Missile DATCOM; propulsion data from GasTurb.
- Once all subsystems are modeled, a trim analysis will be conducted under cruise conditions.
- The system's transfer function will be derived, and its dynamic response under various inputs will be analyzed.
- A controller will be designed based on the system behavior to meet mission specific requirements.
- The nonlinear system will be integrated with the controller and revalidated to ensure closed loop stability.

Software and Methods:

- All subsystem models (aerodynamics, propulsion, atmosphere) will be implemented using MATLAB/Simulink.

- Validation will be conducted by comparing custom models against standard Simulink library blocks.
- Aerodynamic and propulsion models are based on lookup tables to capture nonlinear behavior.
- The atmospheric model is developed using the ISA (International Standard Atmosphere) and validated accordingly.

6.1.2 Full System Test Plan

- When all systems are integrated, the system's target orientation, flight stability and mission completability will be tested.
- In this context, flight dynamics simulations were carried out with tools such as MATLAB/Simulink and/or OpenVSP.

6.2 Results of Simulations

Structural analyses were performed to verify the integrity and reliability of the missile's fuselage and wing structures under the specified aerodynamic loads. The primary components of the missile — the wings and fuselage — were analyzed using the finite element method.

6.2.1 Static and Modal Analysis Results

Static structural analyses were conducted using *ANSYS 2020 R2* [46] software by applying aerodynamic load data obtained from CFD [5] simulations. The results showed that the maximum von Mises stress values remained below the yield strength of selected aluminum alloys (Al 7075 and Al 2024). This indicates that the structure possesses sufficient strength and maximum durability under the defined flight conditions. The maximum deformation values were within acceptable limits, maintaining the aerodynamic surface geometry and ensuring the effectiveness of control surfaces.As expected, total deformation was concentrated near the wing tip. In particular, high stress concentrations were observed at the wing root region.

For modal analysis, separate modal analyzes were performed for the wings and fuselage structures to prevent adverse effects of structural resonance on the dynamics of the control system. Additionally, both the results of the static and modal analysis were validated using data from the literature and manual calculations . The results were found to be consistent and closely aligned.

6.3 Compliance with mission requirements and performance criteria

The structural system of the missile successfully fulfills the mission requirements in terms of both mechanical robustness and aerodynamic integrity under the aerodynamic and dynamic loads encountered during the mission profile.

As a result of the static analyzes, the maximum stress values obtained in the wing and fuselage components were found to be below the yield strength of the selected materials, Al 7075-T6 and Al 2024-T3. This indicates that the structure does not undergo any deformation that could pose a risk under the specified flight conditions. The maximum deformation values were also found to be within acceptable limits that do not negatively affect aerodynamic performance. Furthermore, it was observed that the deformation mainly concentrated at the tip of the wings, which is consistent with the initial design assumptions.

The results of the modal analysis demonstrated that the natural frequencies of the structure fall outside the operational frequency range of the control system. Therefore, potential resonance effects during flight have been avoided and the dynamic stability of the structure has been ensured. The mode shapes and frequencies identified through modal analysis do not hinder the effective operation of the control surfaces.

Simulation results obtained from ANSYS [46] were cross-validated with hand calculations and compared to similar models available in the literature. These comparisons confirmed that the simulation results are within acceptable error margins and that the system has been accurately modeled.

In conclusion, the structural subsystem has been designed and verified in full compliance with mission requirements and performance criteria in terms of both static and dynamic analysis outcomes.

7 Budget and Schedule Review

7.1 Budget and Cost

The estimated budget for the cruise missile has been carefully prepared through extensive research of commercially available components, prioritizing cost-effective and performance-balanced solutions. As seen in Table 34, the listed components include essential elements such as the turbojet engine, seeker, GPS + INS system, and various structural components, amounting to a total of 59,927 USD in component costs. Project expenses, including R&D, testing, logistics, and integration, contribute an additional 27,500 USD, while commercial expenses such as marketing, legal licensing, and insurance add 8,000 USD to the overall budget.

The selection process took into account the balance between performance and cost effectiveness, though it is important to note that these components may undergo changes as the project progresses. Factors such as size, weight, and integration compatibility could necessitate adjustments. Moreover, further optimizations are expected during later design stages, with the aim of enhancing system efficiency and potentially reducing overall costs.

Item	**Sub-item / Description**	**Cost (USD)**
1. Component Costs	Turbojet Engine : JetCat P550 PRO	12,227
	Seeker : FLIR Boson+ Gimbal	10,000
	GPS + INS : Honeywell HG1930 + NovAtel OEM719 GNSS	7,000
	Computer and Software : Embedded processor + mission software	8,000
	Fin Servos : RDS51150	200
	Battery : Thermal Battery	2,000
	Warhead : OFAB-100-120	20,000
	Fuselage, Wings, Fins : Al 2024,Al 7075	1000
	Total Component Costs	**59,927**
2. Project Expenses	R&D : Preliminary design, analysis, prototyping	15,000
	Testing & Certification : Simulation + 1 flight test	5,000
	Logistics & Procurement : Part delivery, permits	2,500
	Integration & Labor : Assembly, cabling, tuning	5,000
	Total Project Expenses	**27,500**
3.Commercial Expenses	Marketing & Sales : Expo participation, brochures, web content	3,000
	Legal & Licensing : Permits, export clearance, etc.	2,000
	Other (insurance, support, etc.) : Optional costs	3,000
	Total Commercial Expenses	**8,000**
Grand Total		**95,927 USD**

Table 34: Cruise Missile Cost Breakdown

7.2 Schedule Review with Gantt Chart

Design project

Group 1

Project start: Pzt, 2.10.2025

Display week: 1

TASK	ASSIGNED TO	PROGRESS	START	END	
Aerodynamics					
CFD Software Training	Aerodynamics	100%	14.02.2025	17.02.2025	4
Airfoil Comparison	Aerodynamics	100%	1.03.2025	13.03.2025	13
Wing Design & Analysis	Aerodynamics	100%	13.03.2025	27.03.2025	15
Full-body CFD Analysis	Aerodynamics	100%	1.04.2025	25.04.2025	25
AGARD B Validation	Aerodynamics	100%	13.04.2025	21.04.2025	9
MISSILE DATCOM Validation	Aerodynamics	100%	21.04.2025	1.05.2025	11
Propulsion					
Approximate Total Drag Calculation	Propulsion	100%	16.02.2025	2.03.2025	15
Engine Selection	Propulsion	100%	2.03.2025	23.03.2025	22
Engine Analysis	Propulsion	100%	23.03.2025	2.05.2025	41
Inlet Design	Propulsion	100%	30.03.2025	22.04.2025	24
Structures					
Static Structural Analysis	Structures	100%	1.03.2025	5.03.2025	5
Modal Analysis	Structures	100%	4.03.2025	18.03.2025	15
Hinge Mechanism Load Analysis	Structures	100%	19.03.2025	25.03.2025	7
Stress Region Identification	Structures	100%	23.03.2025	26.03.2025	4
Structural Reinforcement Plan	Structures	100%	30.03.2025	30.04.2025	32
Control					
6-DOF Model Development	Control	100%	23.03.2025	7.04.2025	16
Trim Analysis	Control	100%	25.04.2025	2.05.2025	8
Transfer Function & Dynamic Response	Control	100%	27.04.2025	4.05.2025	8
Controller Design	Control	100%	29.04.2025	6.05.2025	8
Closed-loop Test & Validation	Control	100%	4.05.2025	8.05.2025	5

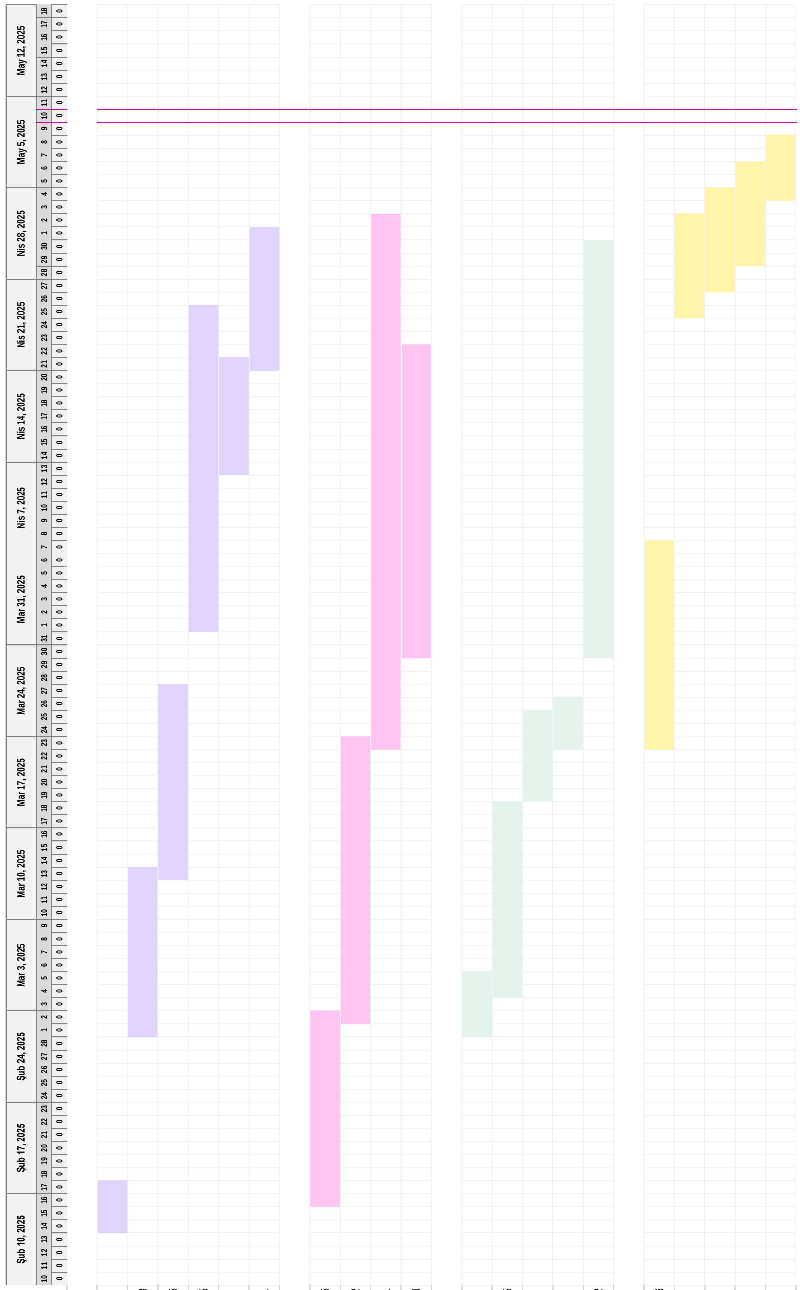

Figure 70: Verification and Validation Gantt Chart

8 Recommendations and Next Steps

8.1 Recommendations

Structure

Weight reduction is proposed by improving structural component and sub-component designs by staying within the confidence intervals established by structural analysis and hand calculations.

Control

It is recommended to focus on improving the control system by performing more detailed actuator modeling, especially considering non-linear effects such as saturation and delay. Additionally, testing different control algorithms and conducting sensitivity analyses could increase system robustness against uncertainties and disturbances during the flight.

Aerodynamics

Prismatic transitions at the front edge of the wing folding mechanism can induce flow separation and increase drag. Therefore, it is recommended to introduce contoured fillets or fairings with appropriate radius of curvature to create a smoothly streamlined, more compact interface. The nose geometry will remain unchanged due to the dimensional limitations imposed by the seeker. However, if the seeker dimensions are revised in the future, redesigning the nose as a conical shape could be considered to reduce pressure drag.

Propulsion

The semi-flush air inlet design has been successfully implemented with the goal of reducing the radar cross-sectional area, and the fuel tank sizing has been optimized based on finalized fuel consumption calculations. However, it is recommended that internal flow analyses be conducted in the future to ensure that the inlet geometry satisfies the engine's mass flow requirements and does not induce flow distortions or significant pressure losses. Additionally, although the JetCat P550 engine meets the current thrust needs, future design iterations may consider using a more compact, lighter, and slightly more efficient alternative to improve integration and overall system performance.

8.2 Next Step

Structure

All structural parts designed separately will be designed as a single solid as in the wing-fuselage connection and full body analysis will be performed. Thermal-structural analysis will be performed to measure the structural effects of thermal stresses during flight.

Control

After the controller tuning is completed, a final system evaluation will be conducted to validate the missile's ability to reach the target under predefined constraints. Two different controllers will be integrated into the system to enable an optimal control strategy. Finally, the project will be concluded with the preparation and presentation of the final results.

Aerodynamics

In future studies, a simple internal flow CFD analysis of the inlet geometry could also be performed; this investigation would rapidly assess total pressure recovery, flow uniformity, and potential separation regions within the inlet, thereby supporting early stage design improvements.

Propulsion

To validate and refine the propulsion system integration, several actions are planned. First, CFD-based internal flow analysis should be carried out to verify inlet performance, including total pressure recovery and distortion at the engine face. The inlet–engine transition zone must be modeled to ensure smooth flow delivery with minimal losses. Off-design performance under varying Mach numbers and altitudes should also be evaluated to confirm robustness. Environmental risks such as icing or foreign object ingestion must be assessed, particularly for low-altitude phases. Based on team feedback, future design iterations may explore engine alternatives that offer reduced size and weight with comparable performance. Lastly, optimization of internal layout—particularly the placement of the fuel tanks, ECU, and pump—should be considered to enhance maintainability, thermal safety, and balance.

9 Acknowledgment

We would like to express our sincere gratitude to our esteemed instructors, Prof. Dr. Ahmet Salih Yiğit, Assoc. Prof. Dr. Mustafa Kaya, Asst. Prof. Dr. Orhan Özçelik, and Asst. Prof. Dr. Oğuzhan Murat, for their invaluable support and guidance throughout the entire process. We also extend our heartfelt thanks to the Roketsan family, who closely followed our work from the beginning to the end, provided constructive feedback at every stage, and greatly contributed to addressing our sectoral knowledge gaps.

References

[1] Charles D. Harris. Nasa supercritical airfoils: A matrix of family-related airfoils. Technical Report NASA TP-2969, NASA Langley Research Center, Hampton, Virginia, 1990. Accessed: May 10, 2025.

[2] SimScale. K-omega turbulence models — global settings, 2025. Available at: https://www.simscale.com/docs/simulation-setup/global-settings/k-omega-sst/Accessed: April, 2025.

[3] SimScale. Turbulence: Which model should i select for my cfd analysis?, 2025. Available at: https://www.simscale.com/blog/turbulence-cfd-analysis/ Accessed: April, 2025.

[4] Dendy Adanta, I. M. Rizwanul Fattah, and Nura Musa Muhammad. Comparison of standard k-epsilon and sst k-omega turbulence model for breastshot waterwheel simulation. *Journal of Mechanical Science and Engineering*, 7(2):039–044, Oct. 2020.

[5] ANSYS Inc. *ANSYS Fluent User's Guide*, 2020. Version 2020 R2; Accessed: May 10, 2025. Available at: https://www.ansys.com/products/fluids/ansys-fluent.

[6] Missile DATCOM software package, 2025. Proprietary version obtained from Roketsan, 2025.

[7] ANSYS, Inc. *ANSYS Fluent Theory Guide, Release 2020 R2*. ANSYS, Inc., Canonsburg, PA, USA, 2020. Accessed: May 11, 2025.

[8] V. Schmitt and F. Charpin. Pressure distributions on the onera-m6-wing at transonic mach numbers. Technical Report AGARD AR 138, AGARD, Fluid Dynamics Panel Working Group 04, May 1979. Experimental Data Base for Computer Program Assessment.

[9] Sean Tuling, B. Vallabh, and M. F. Morelli. Compressibility effects for the agard-b model. *The Aeronautical Journal*, 119:543–552, April 2015.

[10] Daniel P. Raymer. *Aircraft Design: A Conceptual Approach*. AIAA Education Series. American Institute of Aeronautics and Astronautics, Inc., Reston, Virginia, 2018.

[11] The MathWorks, Inc. *MATLAB Release 2023a*. MathWorks, Natick, Massachusetts, United States, 2023. Available at: https://www.mathworks.com/products/matlab.html Accessed: April, 2025.

[12] JetCat Turbinen GmbH. Jetcat p550-pro turbojet engine. https://www.jetcat.de/en/products/p550-pro/, n.d. Accessed: May 10, 2025.

[13] Swinin Technology. Sw-600 turbojet engine. https://www.swinin.com/s-product/sw-600, n.d. Accessed: May 10, 2025.

[14] AMT Netherlands. Amt nike turbojet engine. https://www.amtjets.com/turbines/nike, n.d. Accessed: May 10, 2025.

[15] Joachim Kurzke. *GasTurb 11 – Design and Off-Design Performance of Gas Turbines*. GasTurb GmbH, Augsburg, Germany, 2020. Available at: https://www.gasturb.deAccessed: April, 2025.

[16] Razvan Marius Catana, Grigore Cican, and Gabriel-Petre Badea. Thermodynamic analysis and performance evaluation of microjet engines in gas turbine education. *Applied Sciences*, 14(15):6754, 2024. Accessed: May 10, 2025.

[17] Jack D. Mattingly. *Elements of Propulsion: Gas Turbines and Rockets*. American Institute of Aeronautics and Astronautics (AIAA), Reston, Virginia, 2006. Foreword by Hans von Ohain.

[18] George N. Lewis and Theodore A. Postol. Long-range nuclear cruise missiles and stability. *Science & Global Security*, 3:49–99, 1992.

[19] Siemens Digital Industries Software. *Solid Edge 2024 Student Edition*. Siemens AG, 2024. Available from: https://solidedge.siemens.com/en/student/; Accessed: May 10, 2025.

[20] Geoffrey Tanguy, David Macmanus, Eric Garnier, and Peter Martin. Characteristics of unsteady total pressure distortion for a complex aero-engine intake duct. *Aerospace Science and Technology*, 78:297–311, 2018.

[21] Reuters. Australia to manufacture kongsberg cruise missiles, 2024. Available at: https://www.reuters.com/business/aerospace-defense/australia-manufacture-kongsberg-cruise-missiles-2024-08-22/Accessed: May 3, 2025.

[22] MBDA UK Ltd. Storm shadow cruise missile, 2016. Copyright MBDA UK Ltd 2016.

[23] Mohammad H. Sadraey. *Aircraft Design: A Systems Engineering Approach*. John Wiley & Sons, Ltd., New Hampshire, USA, 2013.

[24] George M. Siouris. *Missile Guidance and Control Systems*. Springer, 2004.

[25] K. Ç. Kılıç. Autopilot and guidance algorithms for infrared guided missiles. M.s. thesis, Middle East Technical University, Ankara, Turkey, 2006.

[26] Rafael Yanushevsky. *Modern Missile Guidance*. CRC Press, 2007.

[27] Adrien Finance, Christophe Dufour, Thomas Boutéraon, Alain Sarkissian, Antoine Mangin, Philippe Keckhut, and Mustapha Meftah. In-orbit attitude determination of the uvsq-sat cubesat using triad and mekf methods. *Sensors*, 21:7361, 11 2021.

[28] The MathWorks, Inc. *Simulink Documentation, Release 2023b*. MathWorks, Natick, MA, USA, 2023. Accessed: May 11, 2025.

[29] FlightGear Development Team. *FlightGear Manual, Version 2017.1*. FlightGear Project, USA, 2017. Accessed: May 11, 2025.

[30] K. T. Chung and M. A. Smith. *Missile Design and Engineering Handbook*. Defense Technical Press, Washington, D.C., 2011.

[31] Army Materiel Command. *Engineering design handbook: Warheads – General (AMCP 706-290)*. U.S. Army Materiel Command, 1964.

[32] Paul D. Groves. *Principles of GNSS, Inertial, and Multi-Sensor Integrated Navigation Systems*. Artech House, 2013.

[33] B. W. Parkinson, J. J. Spilker, P. Enge, and S. J. Hering. *Global Positioning System: Signals, Measurements, and Performance*. American Institute of Aeronautics and Astronautics, 1996.

[34] Michael W. Robbins. The allies' billion-dollar secret: The proximity fuze of world war ii. *HistoryNet*, 2020. Accessed: May 10, 2025.

[35] Department of Defense. Mil-std-2088a: Bomb rack unit (bru), aircraft, general design specification. Technical Report MIL-STD-2088A, U.S. Department of Defense, 2016. Available at: https://everyspec.com/MIL-STD/MIL-STD-2000-2999/download.php?spec=MIL-STD-2088A.033183.pdf Accessed: May 3, 2025.

[36] J. Smith, M. Allen, and R. Thompson. Separation and release devices for aeronautical and astronautical applications: A review. *Journal of Aeronautical Engineering*, 58(3):155–178, 2020. Accessed: May 7, 2025.

[37] L3Harris. *Pneumatic Single Carriage and Release Systems*. L3Harris Technologies, 2023. Available at: https://www.l3harris.com/all-capabilities/pneumatic-single-carriage-and-release-systems Accessed: May 8, 2025.

[38] A. Mouritz. *Introduction to Aerospace Materials*. Woodhead Publishing, 2012.

[39] Flake C. Campbell Jr. *Manufacturing Technology for Aerospace Structural Materials*. Elsevier Science, Oxford, UK, 2006.

[40] Michael F. Ashby. *Materials Selection in Mechanical Design*. Butterworth-Heinemann, Oxford, UK, 3rd edition, 2005.

[41] E. L. Fleeman. *Tactical Missile Design*. AIAA Education Series, Reston, VA, USA, 2001.

[42] Shuang-Shuang Li, Xin Yue, Qing-Yuan Li, He-Li Peng, Bai-Xin Dong, Tian-Shu Liu, Hong-Yu Yang, Jun Fan, Shi-Li Shu, Feng Qiu, and Qi-Chuan Jiang. Development and applications of aluminum alloys for aerospace industry. *Journal of Materials Research and Technology*, 27:944–983, 2023.

[43] Dassault Systèmes. *CATIA V5-6R2021*. Dassault Systèmes, Vélizy-Villacoublay, France, 2021. Computer-Aided Design (CAD) Software.

[44] ANSYS Inc. *ANSYS MECHANICAL User's Guide*. ANSYS, Canonsburg, Pennsylvania, USA, 2024. Available at: https://www.ansys.com/products/structures/ansys-mechanical; Accessed: May 10, 2025.

[45] ANSYS Inc. *ANSYS ICEM CFD User's Guide*, 2020. Version 2020 R2; Accessed: May 10, 2025. Available at: https://www.ansys.com/products/fluids/ansys-icem-cfd.

[46] Ansys Inc. *ANSYS Academic Research Mechanical, Release 2020 R2*. Ansys Inc., Canonsburg, PA, 2020. Finite Element Analysis Software.

[47] Jr. John D. Anderson. *Aircraft Performance and Design*. McGraw-Hill Companies, Inc. Tata McGraw Hill Education Private Limited, New Delhi, India, tata mcgraw-hill edition 2010, fifth reprint 2012 edition, 1999.

[48] Abderrahmane Badis. Subsonic aircraft wing conceptual design: Synthesis and analysis. *International Journal of Sciences: Basic and Applied Research (IJSBAR)*, 00(1):00–00, 2017.

[49] Smithsonian National Air and Space Museum. Tomahawk cruise missile (bgm-109). https://airandspace.si.edu/collection-objects/missile-cruise-ship-launched-tomahawk-bgm-109/nasm_A19820119000, 2024. Accessed: 2025-04-10.

[50] Č. Kostić, A. Bengin, B. Rašuo, and D. Damljanović. Calibration of the cfd code based on testing of a standard agard-b model for determination of aerodynamic characteristics. *Proceedings of the Institution of Mechanical Engineers, Part G: Journal of Aerospace Engineering*, 235:1129–1145, 2021.

10 Appendix

10.1 Technical Drawing of Missile and CFD Domain

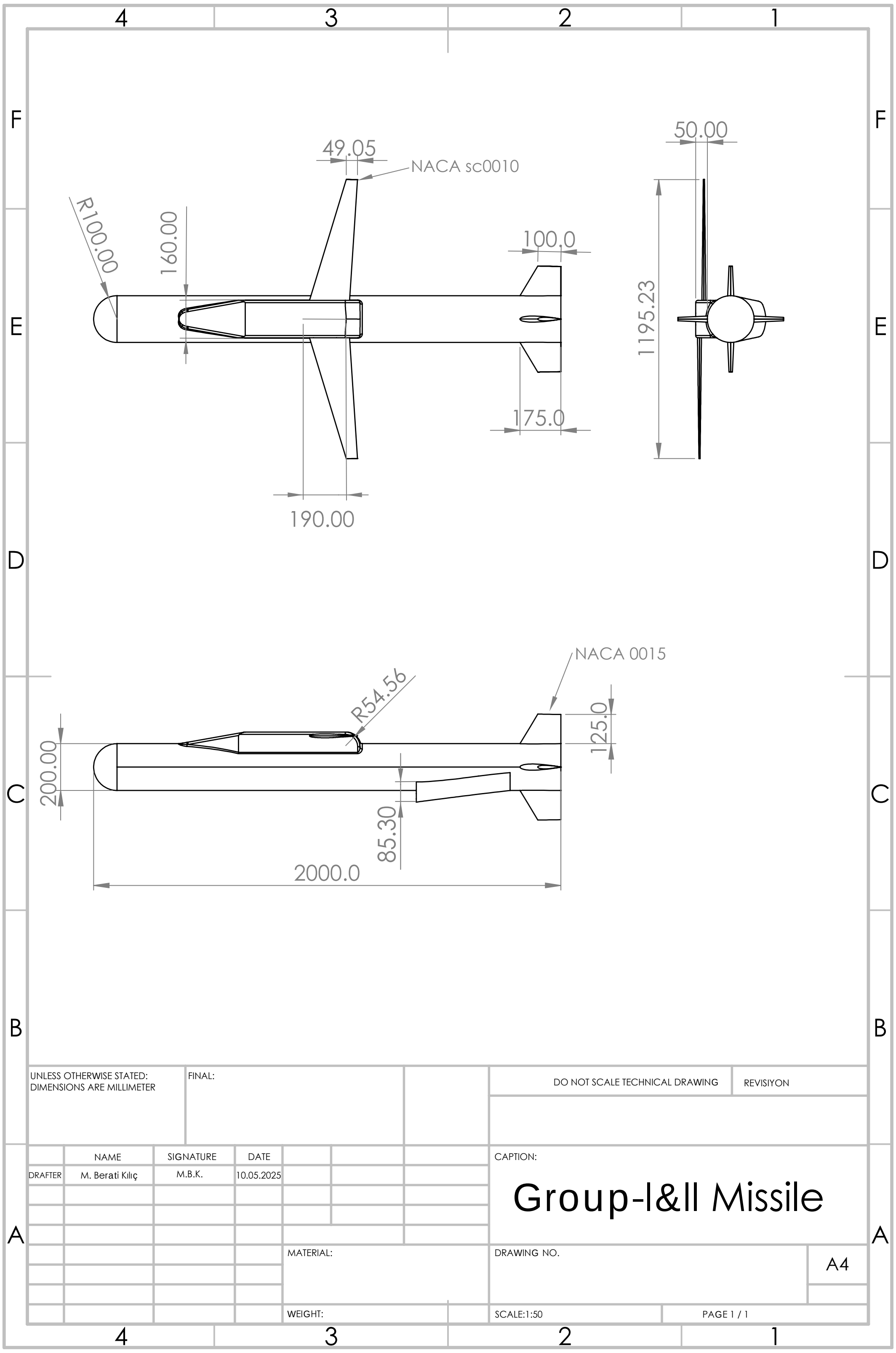

Figure 71: Technical Drawing of Missile

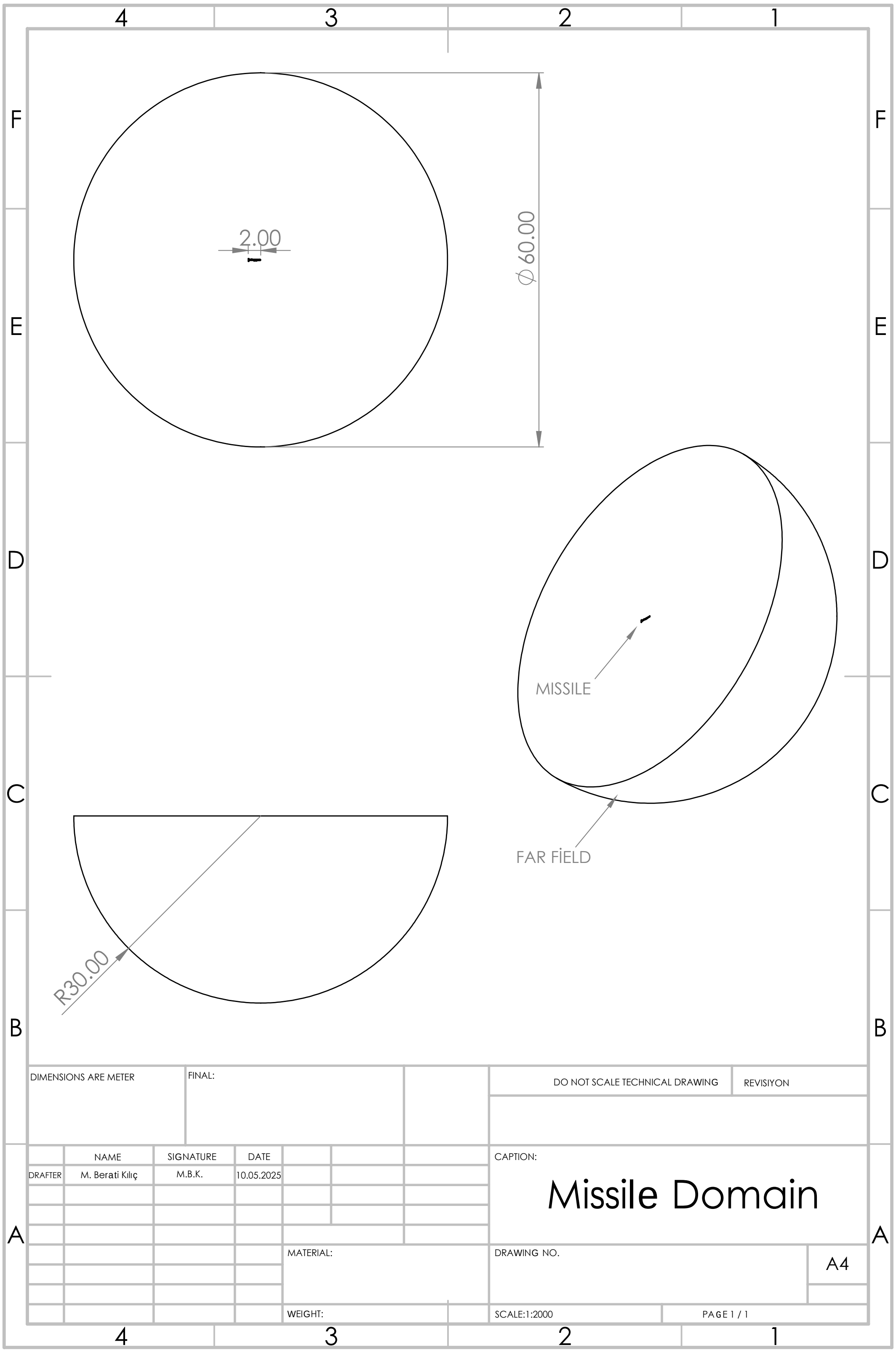

Figure 72: Technical Drawing of CFD Domain

10.2 MATLAB Code for Drag Calculation

```
clc;
clear all;
close all;
Sref=0.338158219;%0.338158219;%1.537701005;%ft^2
Sref_SI=0.0314159265;
MAC=0.437698179;%ft
MAC_tail=0.462300164;
l=6.562;
d=0.656;
f=l/d;
mu= 3.22*10^-7;%3.337*10^-7;
rho=1.2673*10^-3;%0.0765;

M=0.7;
V=677.5;%781;%ft/s
Lambda_m=14.8933150639;
b=1.195228*3.2808399;
AR=b^2/Sref;
dinamikbasinc=13900;%34761.2;%pa = 726.0 psf

%%%%%%%%%%fuselage%%%%%%%%%%%%%
R_f=(rho*V*l)/mu;
Cf_f = 0.455 / ( (log10(R_f))^2.58 *
(1 + 0.144 * M^2)^0.65 );
FF_f = 1 + 60 / f^3 + f / 400;
Swet_f=1.37146433*3.28083993^2;

CD_fuselage=(Cf_f*FF_f*Swet_f)/Sref;


%%%%%%%%%%%wing%%%%%%%%%%%%%%%%%
R_w=(rho*V*MAC)/mu;
Cf_w = 0.455 / ( (log10(R_w))^2.58 *
(1 + 0.144 * M^2)^0.65 );
FF_w = (1 + (0.6/0.3)*(0.10) + 100*(0.10)^4) *
(1.34* M^0.18* (cos(Lambda_m))^0.28);
Swet_w=0.113146233*2*3.28083993^2;
```

```
CD_wing=1.25*(Cf_w*FF_w*Swet_w)/Sref;

%%%%%%%%%fin%%%%%%%%%%%%%%%%%%%%
R_tail=(rho*V*MAC_tail)/mu;
Cf_tail = 0.455 / ( (log10(R_tail))^2.58 *
(1 + 0.144 * M^2)^0.65 );
FF_tail = (1 + (0.6/0.3)*(0.15) + 100*(0.15)^4) *
(1.34*M^0.18);
Swet_tail=4*0.0395930271*3.2808399^2;

CD_tail=1.25*(Cf_tail*FF_tail*Swet_tail)/Sref;

CD_0=CD_tail+CD_wing+CD_fuselage;

%%%%%%%%%%Induced Drag%%%%%%%%%%%%
e1=1.78*(1-0.045*AR^0.68)-0.64;




K=1/(pi*AR*e1);

CL=1032/(34761.2*Sref_SI);
%Kanad n Sref   0.0314159265 0.142857098 m^2
CD=CD_0+K*CL^2;


Drag=CD*dinamikbasinc*Sref_SI;
%Kanad n Sref 0.0314159265 0.142857098 m^2

% ------------------------------

fprintf('Reynolds Number (R): %.3e\n', R_f);
fprintf('Form Factor 2 (FF2 - cylindrical): %.4f\n', FF_f);
fprintf('Friction Coefficient (Cf):  %.6f\n',Cf_f);
fprintf('CD_f=%.6f\n',CD_fuselage);

fprintf('\n=== wing ===\n');
fprintf('Reynolds Number (R): %.3e\n', R_w);
fprintf('FF_w: %.4f\n', FF_w);
```

```
fprintf('Friction Coefficient (Cf):  %.6f\n',Cf_w);
fprintf('CD_w=%.6f\n',CD_wing);

fprintf('\n=== fin ===\n');
fprintf('Reynolds Number (R): %.3e\n', R_tail);
fprintf('FF_tail: %.4f\n', FF_tail);
fprintf('Friction Coefficient (Cf):  %.6f\n',Cf_tail);
fprintf('CD_tail=%.6f\n',CD_tail);

fprintf('\n=== Drag calculation ===\n');
fprintf('CD_0=%.6f\n',CD_0);
fprintf('C_L=%.6f\n',CL);
fprintf('CD=%.6f\n',CD);


fprintf('Drag1=%.6f\ n  ',Drag);
```

10.3 MATLAB Code for Required Fuel Estimation

```
%% Constants
SFC_20k = 0;                % g/(kN.s)
SFC_10k = 39.75             % g/(kN.s)
SFC_sea = 41.1;             % g/(kN.s)
NetThrust_sea = 0.510;      % kN
NetThrust_10k = 0.390;      % kN
NetThrust_20k = 0.290;      % kN
a_sea = 340.1;              % m/s
Mach = 0.7;
a_10k = 328.1;              %m/s
V_sea = Mach * a_sea;       %m/s
V_10k = Mach * a_10k;       %m/s
V_20k = 70;                 % m/s - uav cruise speed
LPG = 0.001235; % litre per gram (Jet A-1 fuel density)
SFC_idle = 300; %ml/min

%% Distances
h1 = 0;                        % meters (20k ft)
h2 = 5000;                    % meters (20k-10k ft)
h3 = 90000;                    % meters (10k ft)
h4 = 5000;                     % meters (10k-330 ft)
```

```
h5 = 10000;                    % meters (330 ft)
%% Time calculations
t2 = h2 / ((V_20k + V_10k)*0.5);
t3 = h3 / (V_10k);
t4 = h4 / ((V_10k + V_sea)*0.5);
t5 = h5 / (V_sea);

%% Fuel consumption for each segment (in grams)
fuel2 = 0;      % g
fuel3 = SFC_10k * NetThrust_10k * t3;      % g
fuel5 = SFC_sea * NetThrust_sea * t5;      %g

%% Convert to liters
fuel2_L = fuel2 * LPG;
fuel3_L = fuel3 * LPG;
fuel4_L = (SFC_idle/1000)*(t4/60);
fuel5_L = fuel5 * LPG;

%% Totals
total_time = t2 + t3 + t4 + t5;             % seconds
total_fuel_L = fuel2_L + fuel3_L + fuel4_L + fuel5_L;  % lt

%% Display results
fprintf('--- Flight Profile Summary ---\n');
fprintf('Time at 20k ft to 10k ft km %.2f min\n', t2/60);
fprintf('Time at 10k ft: %.2f min\n', t3/60);
fprintf('Time at 10k to sea level: %.2f min\n', t4/60);
fprintf('Time at sea level: %.2f min\n', t5/60);

fprintf('Fuel during 20k ft to 10k ft: %.2f L\n', fuel2_L);
fprintf('Fuel at 10k ft: %.2f L\n', fuel3_L);
fprintf('Fuel during 10k to sea level: %.2f L\n', fuel4_L);
fprintf('Fuel at sea level: %.2f L\n', fuel5_L);

fprintf('------------------------------\n');
fprintf('Total flight time: %.2f min\n', total_time/60);
fprintf('Total fuel required: %.2f L\n', total_fuel_L);
```

10.4 Missile Datcom Input File

Listing 1: Missile DATCOM Input File

```
CASEID TOMAHAWK_BGM109
DIM M
DERIV RAD
$FLTCON
 NALPHA=19.0,
 ALPHA(1) = -20.0, -15.0, -12.0, -10.0, -7.0, -5.0, -3.0, -2.0, -1.0, 0.0,
 ALPHA(11) = 1.0, 2.0, 3.0, 4.0, 5.0, 7.0, 10.0, 12.0, 15.0,
 NMACH = 3.0,
 MACH = 0.60, 0.70, 0.80,
 REN = 2.04E06, 2.39E06, 2.73E06,
 BETA = 0.0,
$END
$REFQ
  SREF = 0.031416,
  LREF = 2.00,
  LATREF = 1.195228,
  XCG = 0.904358,
$END
$AXIBOD
  X0 = 0.0,
  TNOSE = POWER,
  POWER = 0.5,
  LNOSE = 0.100,
  DNOSE = 0.200,
  TRUNC = .FALSE.,
  LCENTR = 1.900,
  DCENTR = 0.200,
  TAFT = 1.0,
  LAFT = 0.0,
  DAFT = 0.200,
$END
$FINSET2
  SECTYP = NACA,
  SSPAN = 0.100, 0.2250186,
  CHORD = 0.1747527, 0.0989228,
  XLE = 1.8252474,
  SWEEP = 30.92,
  STA = 0.0,
  NPANEL = 4.0,
  PHIF = 0.0, 90.0, 180.0, 270.0,
  GAM = -10.0,
NACA-1-4-0015
$END
$FINSET1
  SECTYP = NACA,
  SSPAN = 0.1, 0.697614,
  CHORD =  0.1710125, 0.0481604,
  XLE = 0.9255881,
  SWEEP = 16.7,
  STA = 0.0,
  NPANEL = 2.0,
  PHIF = -50.0,50.0,
  GAM = -40.,40.,
NACA-2-4-0010-64
```

```
$END
$DEFLCT
  DELTA1 = 0.0, 0.0, 0.0, 0.0,
  DELTA2 = 0.0, 0.0,$
DAMP
BUILD
PART
WRITE
PLOT
SAVE
NEXT CASE
CASEID TRIM OF CASE NUMBER 1
$TRIM
 SET=2.,
 PANL1=.TRUE.,
 PANL2=.TRUE.,
 PANL3=.TRUE.,
 PANL3=.TRUE.,
 DELMIN=-20.,
 DELMAX=20.,$
SAVE
$END
PRINT AERO TRIM
PART
NEXT CASE
```

10.5 CAD Model of Wing-Fuselage Connection

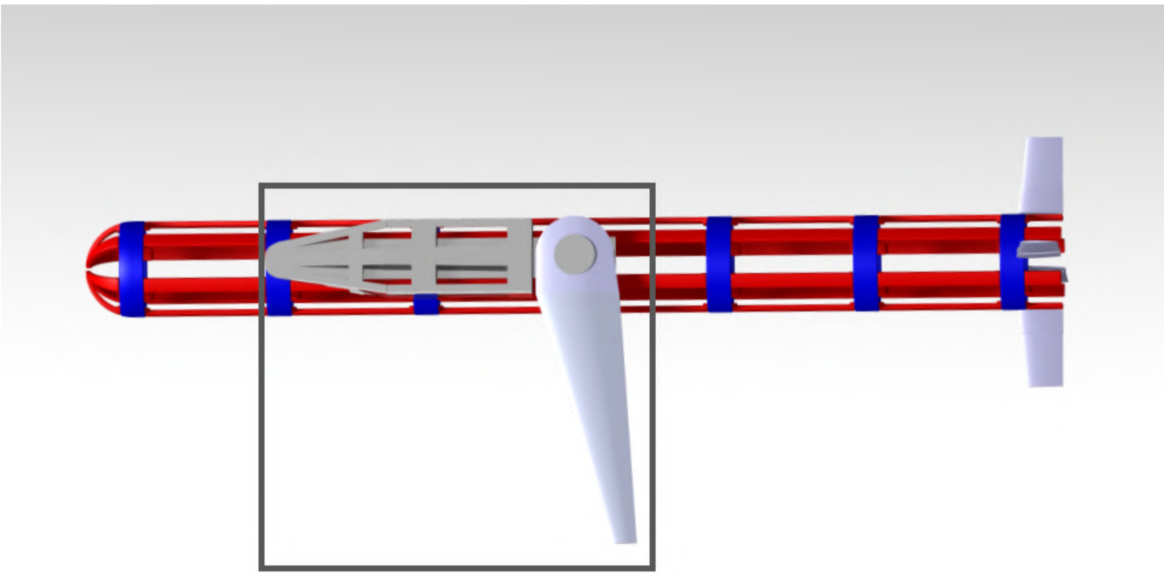

Figure 73: Wing-Fuselage Connection.

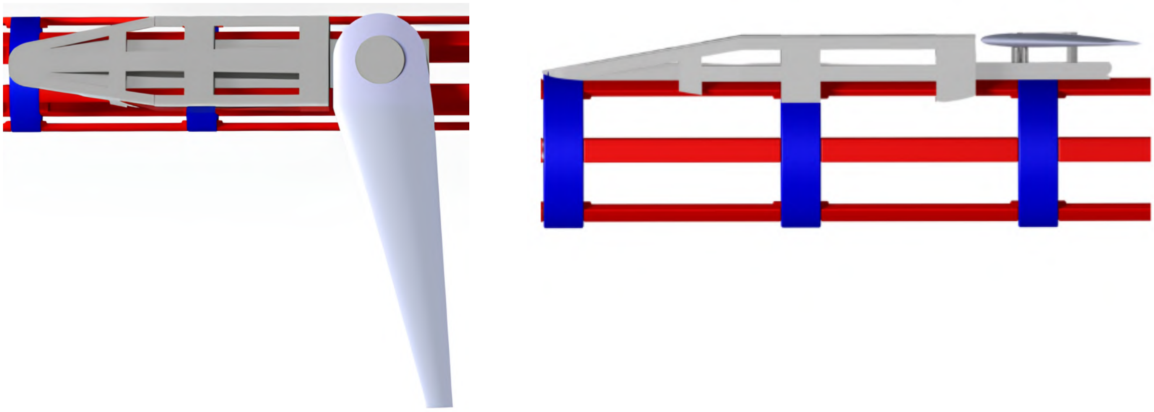

(a) Top View. (b) Side View.

Figure 74: Detailed View of Wing-Fuselage Connection Area.

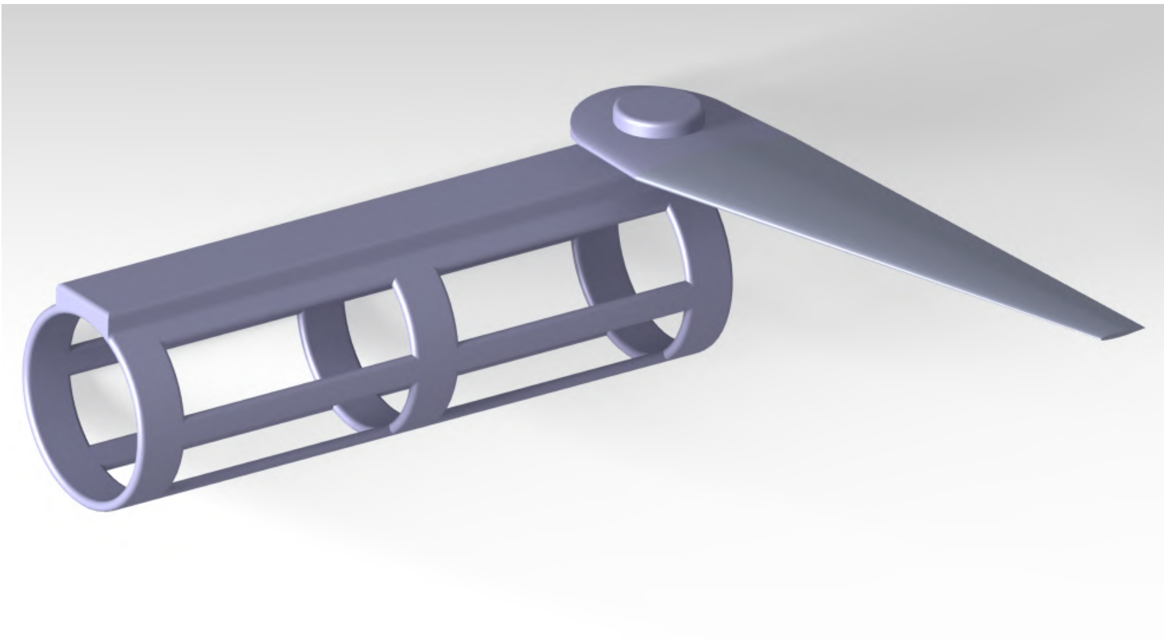

Figure 75: Solid Wing-Fuselage Connection Area.

The frame, stringer and wing in Figures 73 and 74 are designed and assembled separately. In order to make the structural analysis of the wing-fuselage connection part easier, this part is designed as solid as shown in 75.

10.6 CAD Model of Cruise Missile

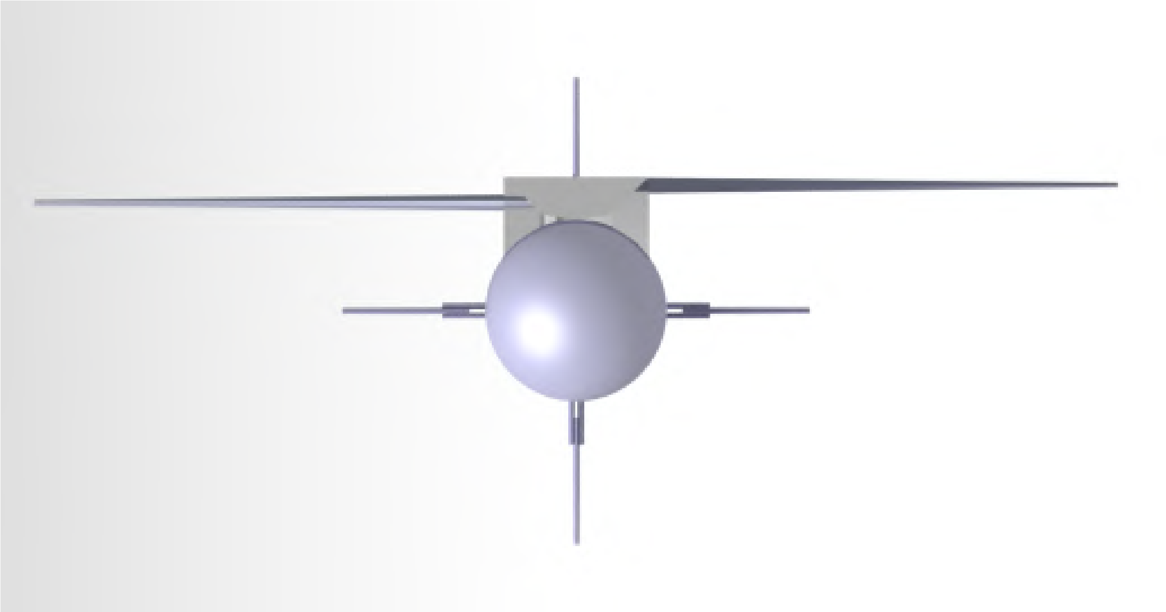

Figure 76: Front View of Missile.

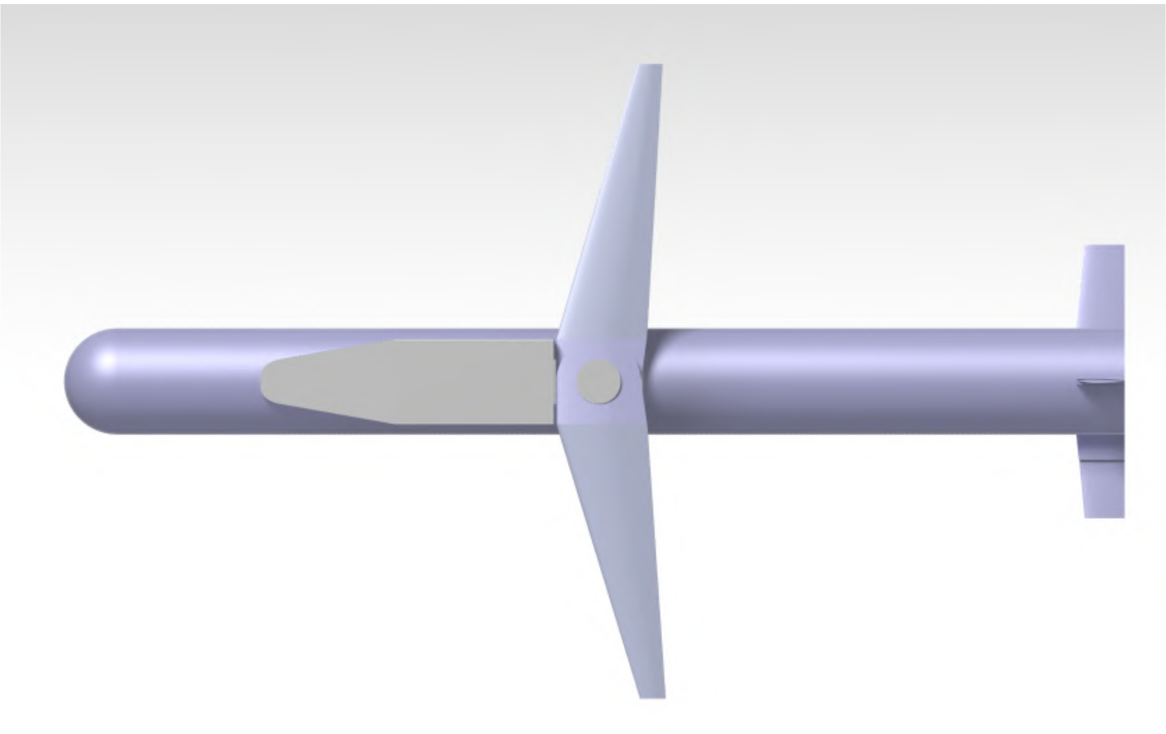

Figure 77: Top View of Missile

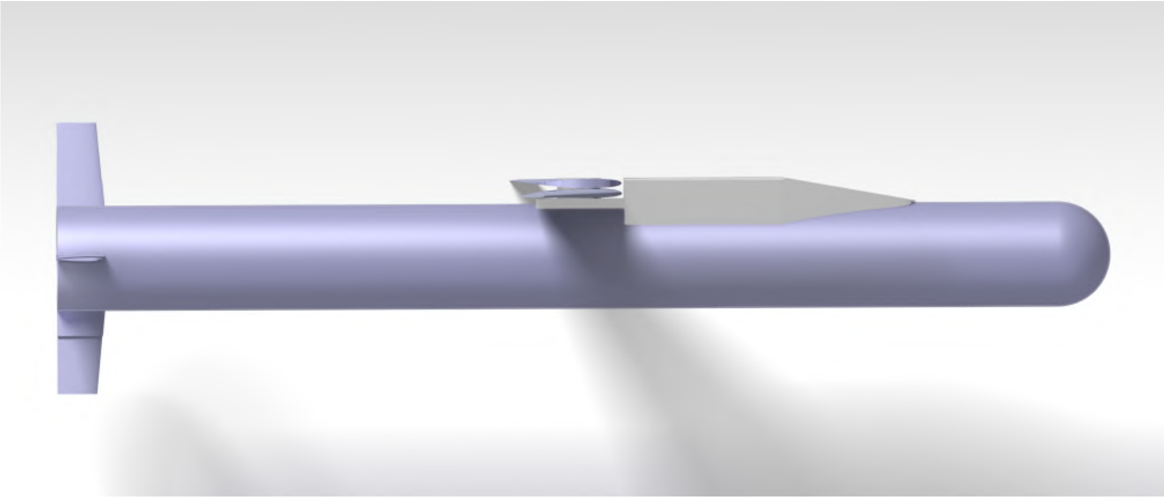

Figure 78: Right View of Missile.

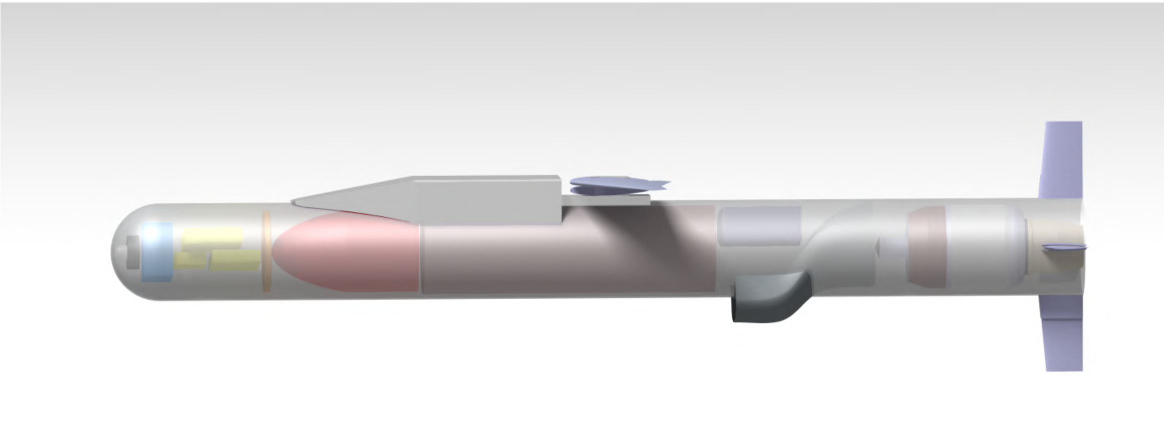

Figure 79: Left View of Missile.

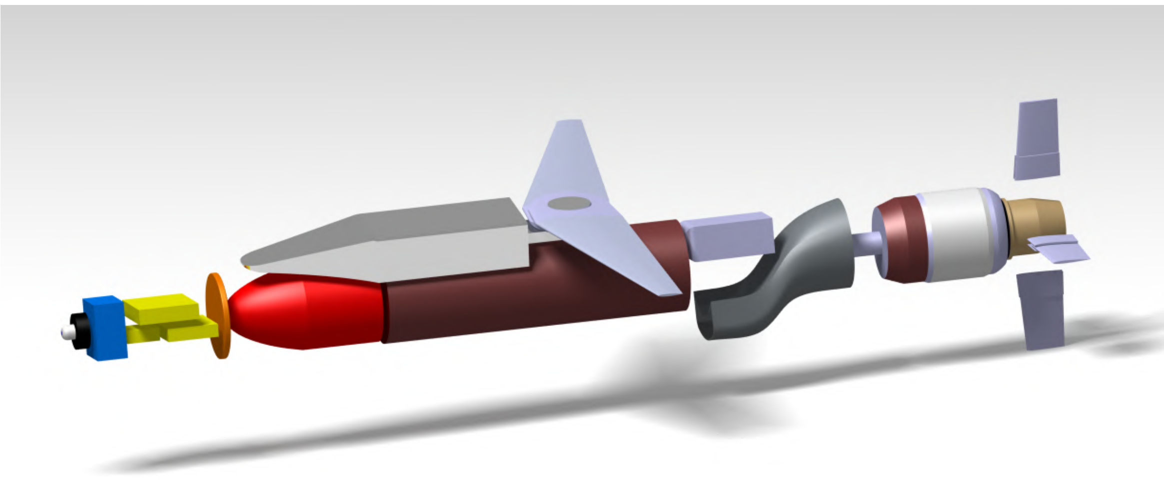

Figure 80: System Integration.